Missing-mass spectroscopy of short-lived nuclei at low-momentum transfer region opened by the MAIKo active target

Tatsuya FURUNO

A dissertation submitted in partial fulfillment of the
requirements for the degree of Doctor of Philosophy in Science,
Department of Physics, Kyoto University

January, 2020

Abstract

A new active target system named MAIKo has been developed for the missing-mass spectroscopies of unstable nuclei. The MAIKo active target is based on a time projection chamber where the detection gas plays also as the target gas. This technique enables us to detect low-energy recoil particles emitted at forward center-of-mass angles. As the first physics experiment with MAIKo, the elastic and inelastic alpha scatterings on ^{10}C were measured using a 68-MeV/u radioactive ^{10}C beam at Research Center for Nuclear Physics, Osaka University. As designed, we have succeeded to reduce the detection threshold for the recoil alpha particles down to 500 keV with MAIKo. The phenomenological α-N effective interaction and the point-nucleon density distribution in the ground state were determined from the differential cross sections of the elastic alpha scattering. The distorted-wave Born-approximation calculation was carried out by using the interaction and density distribution to analyze the inelastic alpha scattering. The calculated cross sections were compared with the measured cross sections, and the neutron transition matrix element M_n from the ground state to the 2^+_1 state at the excitation energy of 3.35 MeV in ^{10}C was determined to be $M_n = 6.9 \pm 0.7\,(\text{fit}) \pm 1.2\,(\text{sys})$ fm^2. The obtained M_n value in ^{10}C is close to the proton transition matrix element M_p in the mirror nucleus ^{10}Be, demonstrating that the isospin symmetry in the $A = 10$ system is conserved. Combining the present result with the previously measured proton transition matrix element in ^{10}C of $M_p = 6.63 \pm 0.11$ fm^2, the ratio of the neutron matrix element to the proton matrix element in ^{10}C was deduced as $M_n/M_p = 1.05 \pm 0.11\,(\text{fit}) \pm 0.17\,(\text{sys})$. This ratio close to unity suggests that the quadrupole transition in ^{10}C is less neutron dominant compared to ^{16}C, and the $Z = 6$ shell closure which was recently proposed in the neutron-rich carbon isotopes like ^{16}C is less evident in proton-rich ^{10}C. The first physics experiment with MAIKo was successfully accomplished, demonstrating that MAIKo has opened the missing-mass spectroscopy of unstable nuclei at low-momentum transfer region.

Contents

1 INTRODUCTION

1.1 Inelastic scattering and its challenge in RI beam experiments

Inelastic scatterings with light ions such as protons or alpha particles are excellent probes to obtain the information on the structures of atomic nuclei. High-resolution spectroscopy with the inelastic scattering unveils nuclear level structures and the cross section provides transition matrix elements between the ground and excited states. The energy levels and the transition matrix elements are the experimental observables which can be directly compared with the theoretical calculations. In inelastic scatterings, measurements at forward scattering angles in the center-of-mass (c.m.) frame with low-momentum transfer are especially important because the differential cross section becomes larger and the reaction mechanism is simple.

With the recent technical developments of the new facilities to provide rare isotope (RI) beams [1–5], it is now possible to measure the inelastic scatterings off short-lived unstable nuclei and to explore the structures of exotic nuclei far from the β-stability line. Studies on the unstable nuclei allow us to test whether the present knowledge of the nuclear structures established on stable nuclei are valid even in the exotic nuclei with large asymmetry in their proton and neutron numbers.

Since we cannot prepare a target of a short-lived unstable nucleus, scattering spectroscopy of unstable nuclei must be performed in the inverse kinematic condition where an RI beam is incident on a target. There are two methods to determine the excitation energy of the beam particle as presented in Fig. 1.1. One method is the invariant-mass spectroscopy in which an excitation energy is deduced from an invariant mass reconstructed by detecting all decay particles emitted from a beam particle such as light-ions, gamma rays, and neutrons. This method enables us to use a thick liquid or solid target which ensures the highest yield. The invariant-mass spectroscopy has been widely applied in many earlier RI beam experiments using relatively high-energy (>50 MeV/u) beams. However, this method is very difficult both in elastic and inelastic scatterings exciting high-lying states. In case of the elastic scattering, a scattered beam particle does not change its angle and energy a lot, and thus it is difficult to distinguish it from the unreacted beam particles. In the inelastic scattering exciting high-lying states, the efficiency for detecting all of the fragments becomes small because multiplicity of the decay fragments including neutral particles becomes high.

The other method is the missing-mass spectroscopy in which an excitation energy is determined by measuring the energy and angle of a recoil particle. Compared to the invariant-mass

spectroscopy, the missing-mass spectroscopy is effective for the elastic scattering because the recoil particles are emitted around 90° in the laboratory frame, which makes it easier to separate them from the beam particles. The missing-mass spectroscopy can be also applied to the inelastic scattering exciting high-lying states because the detection efficiency for recoil particles does not depend on the excitation energy.

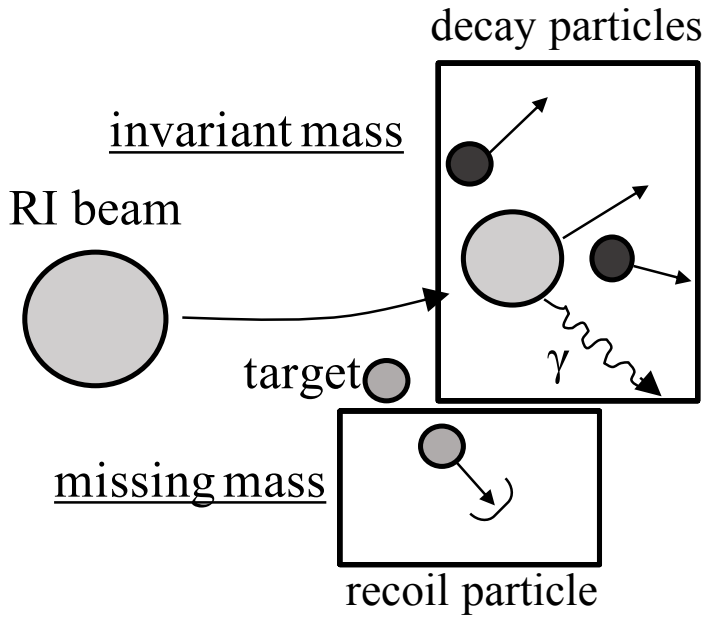

Figure 1.1: Invariant-mass spectroscopy and missing-mass spectroscopy in an RI-beam experiment.

From the kinematics, the energy of the recoil particles become very small at forward angles in c.m. frame, especially in alpha inelastic scattering. Typically, detection of low-energy recoil particles below 1 MeV is required. However, it is almost impossible to detect such low-energy alpha particles with a thin target and an external detector because these particles stop in the target and cannot be detected by the detector. If one uses an extremely thin target, it will reduce the luminosity. So far, there are two methods to detect low-energy recoil particles without losing the luminosity: the cooler ring method and the active target method. In the following sections, we review the two methods.

1.2 Cooler ring method

One method to detect low-energy recoil particles is the cooler ring method which is realized at GSI as the project called "exotic nuclei studied in light ion induced reactions (EXL)" [6]. Figure 1.2 shows a schematic of the detector setup in the EXL experiment [7]. In this method, the RI beams are stored in a cooler ring [8] and an internal gas-jet target

of helium or hydrogen [9] is installed inside the ring. The recoil particles are detected by a dedicated telescope array which consists of double-sided silicon strip detectors (DSSD) and lithium-doped silicon [Si(Li)] detectors [10]. This system can be operated under the ultra-high vacuum condition for the cooler ring. The low-energy recoil particles are detected because the mass thickness of the gas-jet target is extremely low (~ 10 pg/cm^2). At the same time, high luminosity of 10^{26} cm^{-2}s^{-1} is achieved [7] because the unreacted beam particles are impinged repeatedly onto the target. In addition, by using an electron cooler system [11], the emittance and momentum spread of the RI beams can be lowered as small as 0.1π mm·mrad and $\delta p/p \sim 10^{-5}$, which contributes to increase the luminosity due to the large overlap between the beam particles and the gas-jet target.

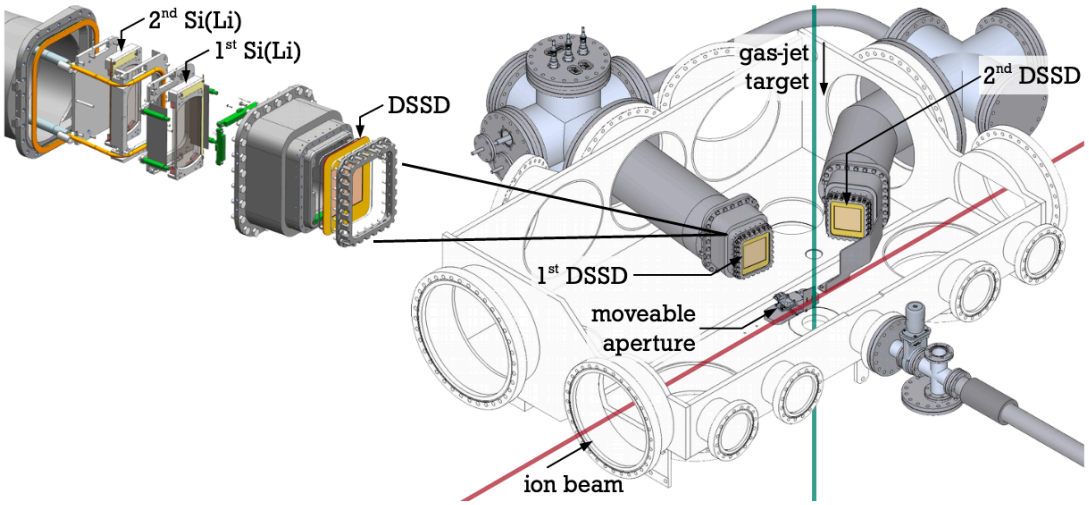

Figure 1.2: Schematic detector setup of the EXL experiment. The figure is taken from Fig. 2 in Ref. [7].

Recently, the EXL project performed measurements of the proton elastic scattering on unstable ^{56}Ni [12] and the alpha elastic and inelastic scatterings on ^{58}Ni [13, 14]. [14]. The experiments successfully lowered the detection threshold for the recoil alpha particles down to 0.5 MeV. Although the EXL project is promising to carry out the missing-mass spectroscopy in a low-momentum transfer region by detecting low-energy recoil particles, it is only applicable to nuclei whose life times are longer than a minute because it takes about one minute to store and cool the RI beams in the cooler ring [15].

1.3 Active target method

The use of a time projection chamber (TPC) as an active target is another solution to detect the low-energy recoil particles. The TPC is a gaseous radiation detector with three-

Table 1.1: Comparison of major active target systems.

Name	Lab.	e^- ampl.	Volume (mm^3)	Pitch	Ch.
IKAR (1971) [16]	GSI	N.A.	$600 \times 200^2\pi$	N.A.	18
MSTPC (2006) [19]	CNS	Wire	$700 \times 150 \times 200$	11 mm	128
MAYA (2007) [20]	GANIL	Wire	$300 \times 280 \times 280$	8.86 mm	1,024
pAT-TPC (2012) [21]	NSCL	μ-megas	$500 \times 125^2\pi$	2 mm	256
CAT (2015) [22]	CNS	GEM	$100 \times 100 \times 250$	4.04 mm	400
AT-TPC (2017) [23]	NSCL	μ-megas	$1000 \times 250^2\pi$	3.33 mm	10,240
ACTAR (2018) [25]	GANIL	μ-megas	$300 \times 300 \times 260$	2 mm	16,384
TexAT (2020) [40]	Texas A&M	μ-megas	$220 \times 240 \times 140$	1.67 mm	1,024
MAIKo (2018) [41]	RCNP	μ-PIC	$100 \times 100 \times 140$	0.4 mm	512

dimensional reconstruction capability for charged particle trajectories. The essential feature of the active target is that the detector gas of the TPC plays a role of a target gas. Typically, helium, hydrogen, deuterium or hydrocarbon gas is used. Since the reaction occurs inside the sensitive volume of the TPC, detection of low-energy recoil particles is possible over the large solid angle. Moreover, the luminosity of the measurement can be increased by extending the length of the TPC along the beam axis, keeping the detection threshold for the recoil particles low. While the cooler ring method can be applied only to relatively long-lived nuclei with $\tau_{1/2} \geq 1$ minute, the active target method can be applied even to short-lived nuclei because the RI beams are bombarded onto the active target immediately after the production. The reconstructed trajectory of a recoil particle is used to determine the recoil angle and recoil energy to obtain the excitation energy of the beam particle.

The first active target named IKAR was developed in 1970s in Leningrad Nuclear Physics Institute, Gatchina, USSR [16]. The IKAR active target was a dedicated detector system to be operated with the high-pressure hydrogen gas at 10 bar. The system was used for proton elastic scattering measurements on neutron-rich isotopes to deduce nucleon distributions [17].

After IKAR, many active target systems were developed around the world [18–26], and measurements using these active targets have been reported [27–36]. Owing to the recent developments of micro-pattern gaseous detectors (MPGD) and readout electronics such as general electronics for time projection chamber (GET) [37], some of the active target systems have large sensitive volumes and many readout channels over 10,000, which contributes to high statistics and high spacial resolutions. Major active targets are listed with the electron-amplification method, sensitive volume of the detector, granularity of the readout (readout pitch), and number of readout channels in Table 1.1. Comprehensive reviews on the recent developments of the active targets are reported in Refs. [38, 39].

1.4 MAIKo active target

1.4.1 Overview

Recently, we developed a new active target system named MAIKo (mu-PIC based active target for inverse kinematics$_{\circ}$) [41] at Research Center for Nuclear Physics (RCNP), Osaka University to realize the detection of the low-energy recoil particles for the missing-mass spectroscopy. In MAIKo, the micro-pixel chamber (μ-PIC) [42] was introduced for the amplification and readout of the electrons with the help of the cosmic ray group in Kyoto University. A schematic view of MAIKo is shown in Fig. 1.3. Compared to the other active targets, the sensitive volume of MAIKo is small, but the readout pitch is the finest (0.4 mm).

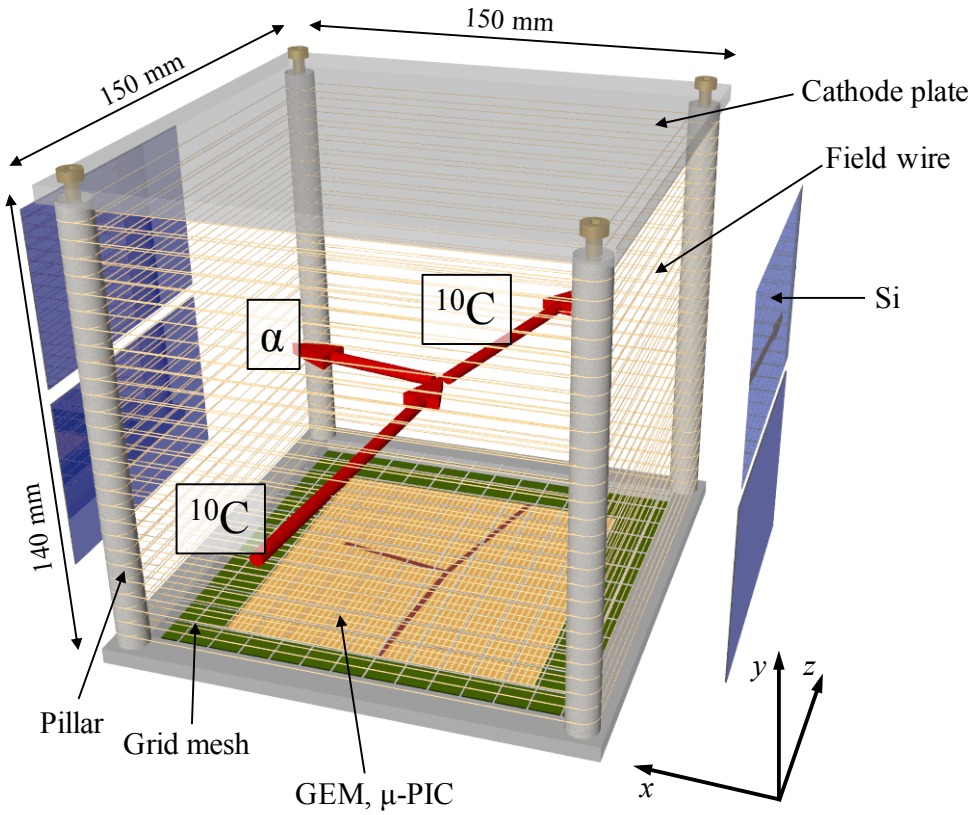

Figure 1.3: Schematic view of MAIKo.

The detailed design of MAIKo is described in Chap. 2. In the development, the following several points were especially taken care.

- Fine readout pitch realized by the μ-PIC
  By introducing the μ-PIC as the readout structure, MAIKo has the finest readout pitch among the existing active target systems. The fine readout pitch enables the identification of the short trajectory in the TPC, thus the low detection threshold for

the energy of the recoil particles. By introducing the strip readout system in MAIKo, the number of the readout channels is small, which made the cost of the development relatively small.

- Purity of the target gas
  As the first experiment using MAIKo, we planed the measurement of the inelastic scattering with alpha particles. Therefore, MAIKo should be operated mainly with He gas. To make the operation of the TPC stable, quenching gas is usually added to the He gas. However, this quench gas might be a background source to the alpha inelastic scattering, thus the fraction of the quenching gas should be as low as possible. After the first beam test with MAIKo, we introduced a gas electron multiplier (GEM) to make the operation more stable even with the smaller fraction of the quench gas.

- Installation of silicon detectors
  Silicon (Si) detectors were used as ancillary calorimetric detectors for high-energy recoil particles, which don't stop in the sensitive volume of MAIKo. The Si detectors should be placed as close to the TPC as possible to reduce the insensitive region. However, eventual discharges between the Si detectors and the TPC took place which damaged the Si detectors and the readout circuits. The discharge occurred especially when the TPC was irradiated with high-rate beam particles. We developed a dedicated structure to protect the Si detectors from the discharge.

- Track reconstruction algorithm
  The MAIKo TPC provides the trajectories of the charged particles as two sets of two-dimensional images from which the recoil alpha particles must be identified. We developed a track reconstruction algorithm based on the Hough transformation.

- Reliability of the active target method
  Compared to the cooler ring method, the detection and analysis of the scattering events with the TPC is complicated. These might cause considerable ambiguity in measuring cross sections. We verified the reliability of the MAIKo active target by comparing the cross sections of the ^{12}C+α elastic scattering with those obtained in the previous experiment.

During the development, several test experiments were performed at RCNP using alpha sources, ^{4}He beam at 56 MeV, and ^{13}C beam at 60 MeV/u. The developments and results of the test experiments have been reported in Refs. [41, 43–49].

1.4.2 Examples of application of MAIKo

MAIKo was designed as a versatile detector system to perform various missing-mass spectroscopies using RI beams at several tens MeV/u at RCNP and RIKEN. In the following, some of the planed applications are presented.

1.4.2.1 Shell structures in unstable nuclei

The magic numbers in nuclei were theoretically established by M. G. Mayer and J. H. Jensen more than 50 years ago [50, 51], which resulted in the Novel Prize in Physics to them in 1963. The nuclear shell model is quite useful to describe various observables such as energy, spin-parity, magnetic dipole and electric quadrupole moments, transition matrix elements, etc. In principle, we must solve the A-body Schrödinger equation in a vast configuration space to calculate these observables. However, the number of the configurations in the calculation explosively increases with mass numbers. The nuclear shell model with a concept of the magic numbers remarkably reduces the number of the configurations by truncating the configuration space for the closed shells.

The nuclear shell structure is still of great interest because it has been reported that the shell structures change in unstable nuclei with unbalanced proton and neutron numbers and the conventional magic numbers (2, 8, 20, 28, 50, 82, and 126) sometimes are not valid in such nuclei. It was found that the magic numbers at N =8, 20, and 28 are less distinct in the neutron-rich regions [52–59]. On the other hand, the emergence of the new magic numbers at $N = 16$ in ^{24}O [60], $N = 32$ from Ar to Cr isotopes [61–66], and $N = 34$ in ^{54}Ca [67–69] were reported. Such appearance and disappearance of magic numbers are of great importance to calculate the properties in unstable nuclei.

There exist many physical observables to pin-down the magic numbers in nuclei: binding energy, nucleon separation energy, energy of the first excited state, and number of isotopes or isotones. As we will discuss in Sec. 1.6, the quadrupole transition strength is also a useful observable. It can be deduced by measuring the inelastic scattering of unstable nuclei with protons or alpha particles with the MAIKo active target.

1.4.2.2 Search for alpha molecular structures

One application is a search for alpha molecular structures in unstable nuclei. The ground states in self-conjugate $A = 4n$ nuclei can be reasonably described with the shell-model picture and have compact structures as illustrated in the left side of Fig. 1.4. On the other hand, well-developed alpha cluster structures are expected to emerge at excitation energies close to their alpha-decay threshold energies. This speculation is based on the well-known "threshold rule" by Ikeda *et al* [70]. One of the most famous alpha cluster states is the 0^+_2 state at $E_x = 7.65$ MeV in ^{12}C. This state is known as the Hoyle state which located at only 0.38 MeV above the 3α decay threshold in ^{12}C. The Hoyle state has a well-developed 3α cluster structure as illustrated in the middle of Fig. 1.4 and plays a crucial role for the carbon synthesis in the universe [71].

Recently, several theoretical calculations predict that there exists a new type of cluster structures called "molecular structures" when excess nucleons are added to the stable self conjugate $A = 4n$ system. For example, in ^{10}Be where two neutrons are added to ^{8}Be (=2α) core, a unique α-$2n$-α structure is predicted by the antisymmetrized molecular dynamics (AMD) model [72, 73] as illustrated in the right side of Fig. 1.4. The excess neutrons play

a role of covalent particles in the molecular orbitals formed by two alpha cores just like two electrons shared by two hydrogen atoms to form a hydrogen molecule.

It is pointed out that the well-developed alpha cluster states are strongly excited by isoscalar monopole transitions [74, 75]. The strength of the isoscalar transition from the ground (0_1^+) state to a excited (0_ν^+) state is defined as

$$B(IS) \equiv \langle 0_\nu^+ || \sum_A r^2 || 0_1^+ \rangle, \tag{1.1}$$

where the summation takes over all of the nucleons. To search for the alpha molecular structures in the Be isotopes, a new measurement of the monopole transition strengths is desired. The alpha inelastic scattering is a useful prove to measure the monopole transition strengths because of its selectivity to isoscalar natural-parity transitions in which the transferred spin and isospin are zero. Since the differential cross section of the monopole transition becomes maximum at $\theta_{\text{c.m.}} \sim 0°$, the measurement should be performed at the forward angles. It requires the detection of low-energy recoil alpha particles from the kinematics. Therefore, the MAIKo active target is indispensable for this measurement.

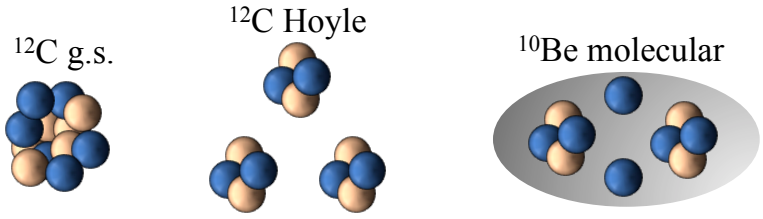

Figure 1.4: Structure of the ground state in ^{12}C (left), Hoyle state in ^{12}C (middle), and molecular state in ^{10}Be (right).

1.4.3 The First experiment with MAIKo

In the present thesis, we report the results of the first physics experiment by using the MAIKo active target [76]. We aimed to perform the missing-mass spectroscopy of the α+^{10}C scattering to investigate the recently proposed new magicity at $Z = 6$. The quadrupole transition strength from the ground state to the 2_1^+ state in ^{10}C was measured. The physics motivation of the present work is described in the next section.

1.5 Physics case in the present work: magicity at $Z = 6$

Recently, a new magicity at $Z = 6$ was proposed in neutron-rich carbon isotopes [77]. The proton radii in ^{14}Be, $^{12-17}$B, and $^{12-19}$C were systematically estimated by measuring the

charge-changing cross sections on a carbon target. The obtained proton radii of nuclei around $Z = 6$ are shown in Fig. 1.5(a). Note that the proton radii in the figure were normalized by the following empirical formula for the proton radii [78, 79]:

$$R_p^{\rm cal} = \sqrt{3/5}(1.15 + 1.80A^{-2/3} - 1.20A^{-4/3})A^{1/3} \text{ fm} \tag{1.2}$$

in order to eliminate the smooth mass-number dependence. The authors found that the proton radii show a clear kink at $Z = 6$ which is similar to those observed at Z =20, 28, 50, and 82 [80]. This indicates a possible major structural change, for example, emergence of a shell closure at $Z = 6$.

The authors also examined the reduced electric quadrupole transition rate $B(E2; 0_1^+ \rightarrow 2_1^+)$ in neutron-rich carbon isotopes. The $B(E2; 0_1^+ \rightarrow 2_1^+)$ value represents the contribution of protons to the quadrupole excitation from the ground state to the 2_1^+ state and should be small in proton-closed shell nuclei. Figure 1.5(b) shows the systematics of the $B(E2; 0_1^+ \rightarrow 2_1^+)$ values in the various isotonic chains as a function of proton number. It should be noted that the $B(E2; 0_1^+ \rightarrow 2_1^+)$ values become minimum at $Z = 6$ in the N =8, 10, 12, and 14 isotones. This fact suggests the magicity at $Z = 6$ in the neutron-rich nuclei.

To further examine the subshell closure at $Z = 6$, the authors investigated the second derivative of binding energies defined as [81]

$$\Delta_p(N, Z) \equiv (-1)^Z[S_p(N, Z) - S_p(N, Z + 1)]/2, \tag{1.3}$$

where $S_p(N, Z)$ represents the one-proton separation energy. $2\Delta_p(N, Z)$ gives the proton single-particle energy-level spacing or shell gap between the last occupied (e_p) and first occupied proton orbitals (e_{p+1}). To eliminate the effect of proton-proton (p-p) paring, they subtracted out the p-p paring energies using the empirical formula: $\Delta_{p\text{-}p} = 12A^{-1/2}$ MeV. Figures 1.5(c) and (d) show the systematics of $e_p - e_{p+1} \equiv 2\Delta_p(N, Z) - 2\Delta_{p\text{-}p}$ for even-Z nuclei. The cups at $Z = N$ for all of the isotonic chains are due to the Wigner effect [82]. Apart from the $Z = N$ nuclei, sizable enhances were observed at $Z = 6$ in N =7–14 as well as at $Z = 8$ in N =8–10 and N =12–16, which is also a signature of the magicity at $Z = 6$.

Combining the three results, the authors claimed the shell closure at $Z = 6$ in the neutron-rich $^{13-20}$C isotopes. Actually, the idea of the possible magic number at six was already pointed out by Mayer. In her Novel lecture in 1963 [83], she mentioned: "There are two different series of numbers, 2, 8, 20, 40..., of which 40 is no longer noticeable, and another, 6, 14, 28, 50, 82, 126 of which the first two at 6 and 14 are hardly noticeable. The second series is due to spin-orbit coupling." Although Mayer pointed out that the magic number six is hardly noticeable, the results in Ref. [77] shows that the effect of the magicity might be a reality, at least in the neutron-rich region.

It is a natural question whether the magicity at $Z = 6$ reported in the neutron-rich isotopes persists even in the proton-rich side. Thus, experimental information on the proton-rich carbon isotopes, for example ^{10}C, is of importance. To test the $Z = 6$ magicity in ^{10}C, we investigate its quadrupole transition matrix elements from the ground state to the 2_1^+

state. In the next section, we discuss the relation between the magicity and the quadrupole transition matrix element.

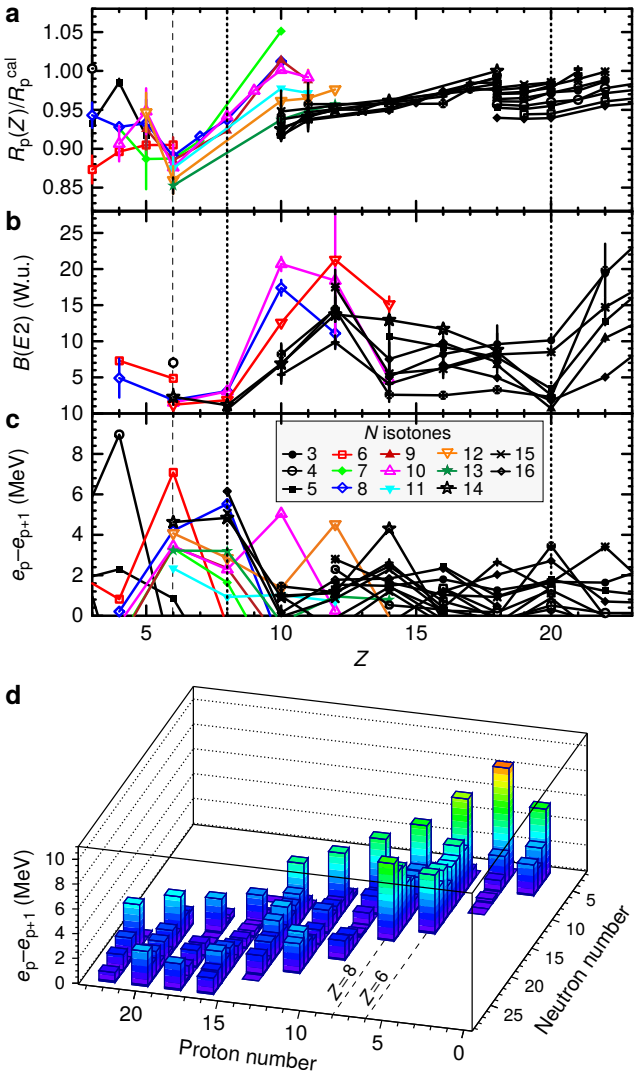

Figure 1.5: Proton-number dependencies of nuclear observables with different isotones with the neutron number N. (a): Proton radii deduced from the charge-changing cross section which are normalized with the value in Eq. (1.2). (b): The reduced electric quadrupole transition rate from the ground states to the 2_1^+ states. (c) and (d): Second derivatives of binding energies subtracted by the p-p paring energies. The positions at $Z = 6$, 8, 20 (only in (c)) are indicated by the black dashed and dotted lines, respectively. The figures are taken from Fig. 3 in Ref. [77].

1.6 Quadrupole transition matrix element

The quadrupole transitions between nuclear states provide valuable information on nuclear structures. Their strengths play key benchmarks in testing theoretical models because they give the overlaps of the wave functions between the ground state and the excited states. In even-even nuclei, the neutron (proton) transition matrix element from the ground (0_1^+) state to the 2_1^+ state defined as

$$M_{n(p)} \equiv \langle 2_1^+ || \sum_{n(p)} r^2 Y_2 || 0_1^+ \rangle, \tag{1.4}$$

is one of useful observables to investigate nuclear shell structures [84–86].

If one considers proton as a point particle, M_p can be related to the reduced electric quadrupole transition rate $B(E2; 0_1^+ \to 2_1^+)$ by the following formula:

$$B(E2; 0_1^+ \to 2_1^+) = e^2 |M_p|^2. \tag{1.5}$$

The relationship between excitation ($0_1^+ \to 2_1^+$) and deexcitation ($2_1^+ \to 0_1^+$) reduced transition rates are given by an equation

$$B(E2; 0_1^+ \to 2_1^+) = \frac{2J'+1}{2J+1} B(E2; 2_1^+ \to 0_1^+) = 5B(E2; 2_1^+ \to 0_1^+), \tag{1.6}$$

where J and J' are the spins of the 0_1^+ and 2_1^+ states.

In a naive liquid-drop model, the ratio of the neutron and proton matrix elements is given as [85]

$$\frac{M_n}{M_p} = \frac{N\delta_n}{Z\delta_p}. \tag{1.7}$$

Here, N and Z are neutron and proton numbers, respectively. $\delta_{n(p)}$ is the nuclear deformation length of neutron (proton) and it is related to the deformation parameter $\beta_{n(p)}$ as

$$\delta_{n(p)} = \frac{3}{2}\sqrt{\frac{5}{4\pi}}\beta_{n(p)}. \tag{1.8}$$

Assuming that the density distributions of proton and neutron in a nucleus are similar ($\delta_n = \delta_p = \delta$), the ratio simply yields

$$M_n/M_p = N/Z. \tag{1.9}$$

In the nuclear shell model, the quadrupole transitions from the 0_1^+ state to the 2_1^+ state are described as rearrangements of particle-hole configurations in the valence shells. When the neutron (proton) shell is closed, the transition of the neutrons (protons) is suppressed remarkably because the intra-shell excitation in the closed shell is hard to occur energetically. As a consequence, the M_n/M_p ratio becomes significantly smaller (larger) than the expectation of Eq. (1.7). After the construction of the RI beam facilities, numerous efforts

have been devoted to deduce transition matrix elements in unstable nuclei and clarify shell structures [87–112].

The proton transition matrix element M_p can be determined directly by using the electromagnetic probes such as electron inelastic scattering or gamma decay measurement from the excited states to the ground states. However, there exists no direct way to determine M_n because no probe is sensitive to the neutrons only. One method to obtain M_n in a nucleus is to adopt M_p of its mirror nucleus relying on the charge symmetry. The other method is to measure the cross section of the inelastic scattering to the 2^+_1 state using a hadronic probe such as proton or alpha particle. Since the cross section of the inelastic scattering is sensitive to both M_n and M_p, the M_n value can be estimated from a combined analysis of the measurements using the electromagnetic probe and hadronic probe.

1.7 Previous experiments on ^{10}C

The 2^+_1 state in ^{10}C locates at $E_x = 3.35$ MeV [113]. The $B(E2; 0^+_1 \to 2^+_1)$ value in ^{10}C had been known to be 9.6 ± 1.6 Weisskopf units (W.u.) [114]. This value is not small compared to those in the neutron-rich carbon isotopes, for example, 1.7 W.u. in ^{16}C [100] and 1.5 W.u. in ^{18}C [101]. In order to investigate whether $Z = 6$ shell closure persists in the proton-rich carbon isotopes, the M_n/M_p ratio in ^{10}C should be determined first If the shell closure in ^{10}C is distinct, the ratio will be larger than the expectation of Eq. (1.7) or (1.9). In ^{16}C, the M_n/M_p ratio of 3, which is much larger than $N/Z = 1.7$, was reported [92, 97, 101].

To deduce the M_n value in ^{10}C, the differential cross sections of the p+^{10}C elastic and inelastic scattering exciting the 2^+_1 state at $E_x = 3.35$ MeV were measured using a ^{10}C beam at 45 MeV/u impinged on a polypropylene $(CH_2CHCH_3)_n$ target [94]. The cross section of the inelastic scattering was measured at $20^\circ < \theta_{\rm c.m.} < 50^\circ$ as shown by the solid circles in Fig. 1.6.

In this experiment, the missing-mass spectroscopy was performed by detecting the recoil protons with a semiconductor detector system named MUST [115]. In case of the proton inelastic scattering, the differential cross section becomes maximum around $\theta_{\rm c.m.} \sim 35^\circ$. The recoil energy of the proton emitted to this angle is approximately 13 MeV, and they are easily detected because they can escape from the target material and reach the MUST detector.

The authors performed a distorted-wave Born approximation (DWBA) calculation using the Jeukenne-Lejeune-Mahaux (JLM) potential which is based on infinite nuclear matter calculation [116]. By comparing the measured cross section with the DWBA calculation (solid line in Fig. 1.6), the authors in Ref. [94] determined the M_n/M_p ratio to be 0.70 ± 0.08. This small value suggests that the shell closure effect at $Z = 6$ is not distinct because the large value is expected if the proton shell is closed.

The authors took the $B(E2; 0^+_1 \to 2^+_1)$ value of 9.6 ± 1.6 W.u. from Ref. [114] in their analysis. A more recent lifetime measurement of the 2^+_1 state in ^{10}C, however, reported a smaller value of $B(E2; 0^+_1 \to 2^+_1) = 6.9 \pm 0.2$ W.u. [117] with much smaller uncertainty compared to the previous measurement. The smaller value of $B(E2; 0^+_1 \to 2^+_1)$ might lead

Table 1.2: Ratios of the external-field interaction strengths b_n^F/b_p^F for various probes at different incident energies [84].

External field	Energy	b_n^F/b_p^F
Electromagnetic	All	0
Proton	10-50 MeV	3
Proton	0.8 GeV	0.83
Proton	1 GeV	0.95
Neutron	10-50 MeV	1/3
Alpha	All	1
π^-	160-200 MeV	3
π^+	160-200 MeV	1/3

to the larger value of M_n, thus the M_n/M_p ratio can become larger.

To disentangle the neutron transition matrix element from the measured cross section of the inelastic hadron scattering, the Bernstein prescription is widely used [84]:

$$\frac{d\sigma}{d\Omega} \propto |b_n^F M_n + b_p^F M_p|^2. \tag{1.10}$$

Here, b_n^F and b_p^F are external-field interaction strengths which reflect the effective interaction between an incident particle and a proton or neutron in nuclei. The values of b_n^F and b_p^F depend on the incident energy of the probe and the target nucleus. The presently accepted b_n^F/b_p^F ratios for various probes are presented in Table 1.2 [84]. In the case of the proton inelastic scattering, the ratio b_n/b_p phenomenologically determined has a strong energy dependence varying from 0.83 to 3 in the incident-energy range of 10–1000 MeV, and it also depends on nuclides. These dependencies cause a serious model ambiguity in the determination of the M_n/M_p ratio from the measured cross section [112]. On the other hand, in the case of the alpha inelastic scattering, the b_n^F/b_p^F ratio is always 1 because of the isospin zero nature of an alpha particle. Thus, the alpha inelastic scattering is more suitable to deduce M_n than the proton inelastic scattering.

1.8 New experiment on ^{10}C

1.8.1 Overview

In the present work, the cross sections of the elastic and inelastic alpha scattering on ^{10}C were measured with the MAIKo active target. The effective α-N interaction and the point-nucleon density distribution in the ground state in ^{10}C were determined to reproduce the cross sections of the alpha elastic scatterings. Using the effective interaction and the density

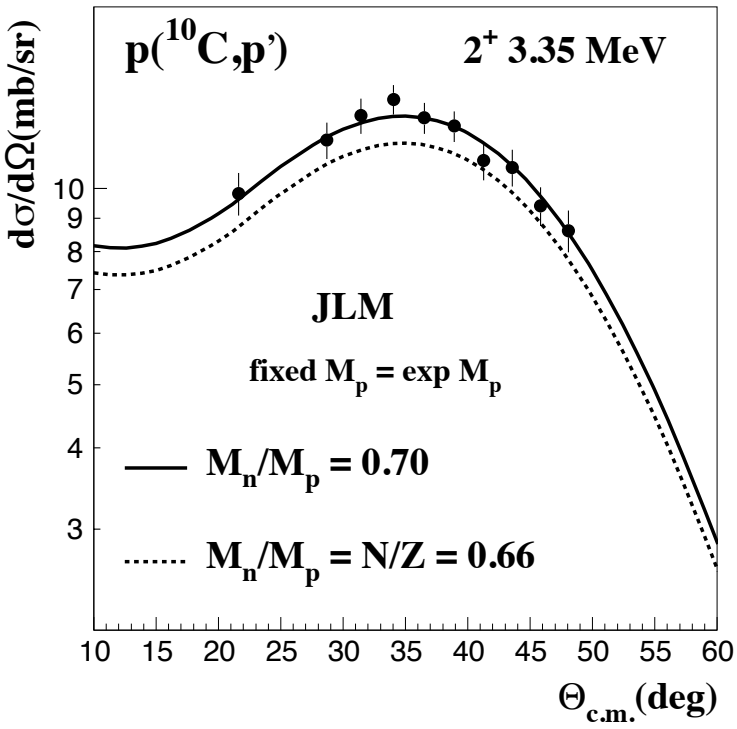

Figure 1.6: Differential cross section of the proton inelastic scattering on ^{10}C exciting the 2_1^+ state at E_x = 3.35 MeV at a beam energy of 45 MeV/u. The solid and dashed lines represent the DWBA calculation with the JLM potential [116], assuming the M_n/M_p values of 0.70 and 0.66 (=N/Z), respectively. The figure was taken from Fig. 17 in Ref. [94].

distribution, the DWBA calculation was performed to deduce the M_n value from the measured cross section of the alpha inelastic scattering without ambiguity of the parameters in the Bernstein prescription.

Although the cross section of the inelastic scattering could be measured by detecting the decay gamma rays from the 2_1^+ state to the ground state, this technique cannot be applied to measure the cross section of the elastic scattering which is needed to determine the effective α-N interaction and the point-nucleon density distribution. Therefore, the missing-mass spectroscopy should be performed to measure both the elastic and inelastic scattering cross sections.

1.8.2 Kinematic condition

Figure 1.7 shows the differential cross sections of the alpha inelastic scattering on ^{10}C at 68 MeV/u with different angular momentum transfers ΔL calculated with the DWBA. The adopted energy of the ^{10}C beam was set at the highest energy available at RCNP to make the intensity as high as possible. The DWBA calculation was carried out with the single-folding model potentials (see Chap. 5) assuming that an excited state at E_x = 3.35 MeV exhausts

100% of the energy-weighted sum-rule strengths. This figure suggests that the measurement of the $\Delta L = 2$ transition exciting the 2^+_1 state should cover $\theta_{\mathrm{c.m.}} \sim 7^\circ$ where the differential cross section takes the maximum. The energy of the recoil alpha particle in the inverse kinematic scattering is plotted as a function of the recoil angle in the laboratory frame in Fig. 1.8. The blue, orange, green, and red lines show the correlation between the energy and angle at the excitation energies of 0, 5, 10, and 15 MeV, respectively. The c.m. angles are plotted by the black solid circles. At $\theta_{\mathrm{c.m.}} \sim 7^\circ$, the energy of the recoil alpha particles is as low as 2 MeV and it is hard to detect such a low energy alpha particles in the conventional experimental setup. Since the half life of ^{10}C is only 19 seconds, the cooler ring method cannot be applied. Therefore, MAIKo is a unique device to realize the present measurement.

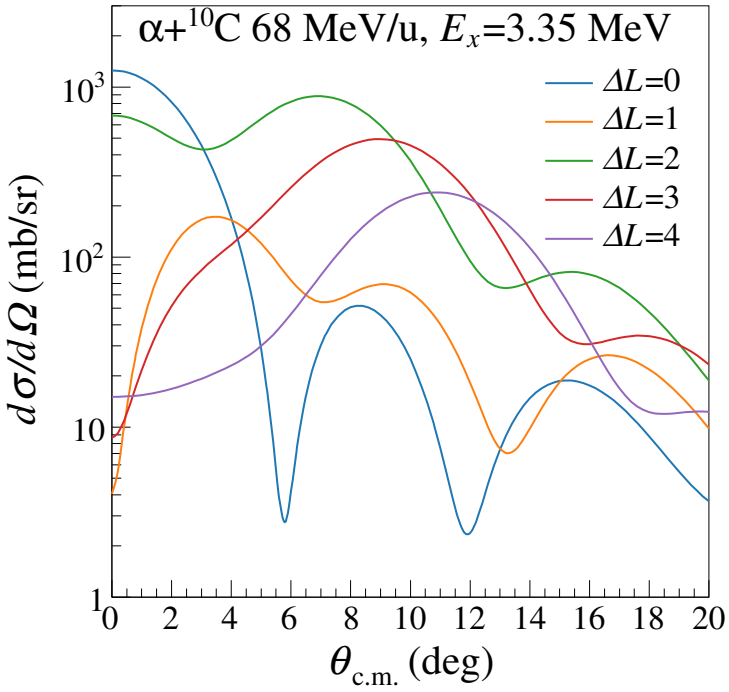

Figure 1.7: Differential cross sections of the α+^{10}C inelastic scattering at 68 MeV/u calculated by the DWBA. The blue, orange, green, red, and purple lines represent the cross sections with different transferred angular momenta ΔL.

1.9 Contents of the thesis

The present thesis is organized as follows. Firstly, the detailed design of the MAIKo system is described in Chap. 2. The experimental details such as experimental apparatus, data acquisition, and summary of the measurement are described in Chap. 3. The analysis of the MAIKo TPC data is presented in detail in Chap. 4. The DWBA analysis to deduce M_n from the measured cross section is described in Chap. 5. The results are discussed in Chap.

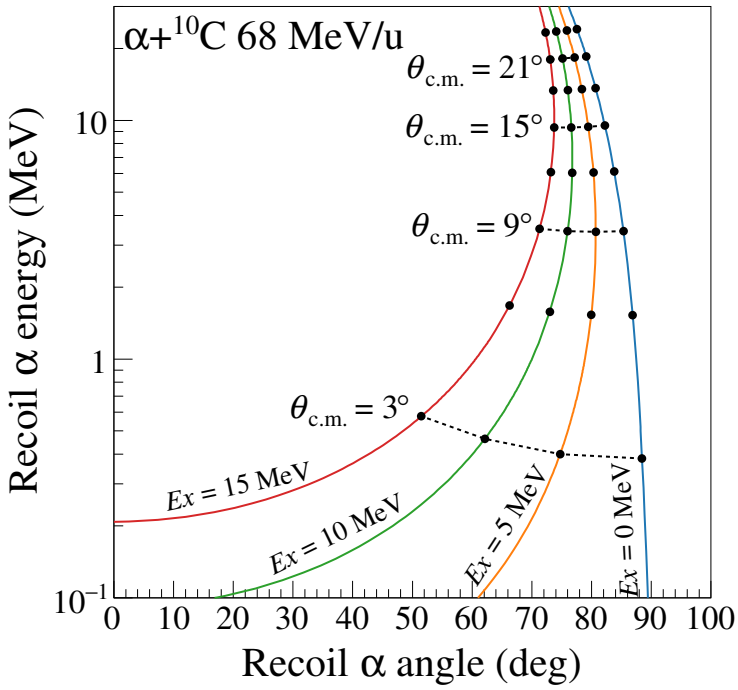

Figure 1.8: Energy of recoil alpha particle as a function of the recoil angle in the α+^{10}C scattering at 68 MeV/u with different excitation energies in ^{10}C.

6. Finally, the conclusions and future outlooks are given in Chap. 7.

2 DESIGN OF MAIKO

2.1 Overview

The schematic view of the MAIKo active target is shown in Fig. 1.3. The system is based on a cubic-shape TPC detector . The volume of the TPC field cage is $150 \times 150 \times 140$ mm^3 and the sensitive volume is $102.4 \times 102.4 \times 140$ mm^3. The detector is installed in a stainless-steel vacuum chamber with a volume of approximately 30 L. The chamber is filled with helium gas which plays a role of a helium target. A small fraction of quenching gas is added to the helium gas for the stable operation of the TPC. The pressure of the TPC gas can be changed from 100 to 2000 hPa depending on the experimental requirements.

The charged particles ionize the mixture gas along their trajectories in the TPC and the ionization electrons drift vertically downwards along the electric field formed by the TPC field cage. At bottom of the TPC, the electrons are multiplied first by a gas electron multiplier (GEM) and then by the μ-PIC. The μ-PIC is also used to determine the two-dimensional position of the electrons. The electron drift time multiplied by the drift velocity determine the vertical position of the primary electrons. These information was used to determine the three-dimensional position of the charged particles.

The angle of the recoil particles is determined from the reconstructed trajectory. If the recoil particles stop inside the TPC sensitive volume, the recoil energy is determined from the length of the trajectory in the gas. High-energy recoil particles which pass through the TPC are detected with four silicon detectors installed at the left and right sides of the TPC.

2.2 TPC field cage

The electric field inside the sensitive volume of the TPC is formed by applying negative high voltages on the stainless-steel cathode plate and the nickel grid mesh. Figure 2.2 shows the electric circuit of the field cage. The cathode plate has a dimension of $150 \times 150 \times 3$ mm^2. The surface of the plate is buff-polished to avoid an electric discharge. The wires of the grid mesh have a diameter of 150 μm and its pitch size is 0.85 mm (30 wires per inch). The grid mesh is glued on a frame made of Macor. Macor is a machinable glass-ceramic and it is a low-outgassing material. The high voltage applied to the grid mesh is tuned so that it is transparent to the electrons but opaque for the positive ions generated by the avalanche at the GEM and the μ-PIC. The distance between the cathode plate and the grid mesh is kept at 140 mm with four pillars made from Macor. Field wires with diameters of 125 μm are wound doubly around the pillars to make the drift field uniform. The pitch between the

wires is 5 mm. They are connected via 10-MΩ metal-film resistor[1] chain to make a voltage divider. The precision of the resistance value is 0.1%. The tension of the field wires is kept at 2 N.

A finite element simulation with the computer codes Garfield [118] and neBEM [119] was performed to calculate the uniformity of the electric field. The calculation was carried out including the Si detectors which may worsen the uniformity of the electric field. Figure 2.1 shows the result of the calculation. The color map in the figure shows the distortion of the vertical electric field at the middle height of the TPC field cage ($y = 70$ mm). The distortion ΔE_y at a point (x, y, z) is defined as:

$$\Delta E_y(x, y, z) = \frac{E_y(x, y, z) - E_y(0, y, 0)}{E_y(0, y, 0)}, \tag{2.1}$$

where the origin of the coordinate is the center of the μ-PIC sensitive surface. The boundary of the μ-PIC sensitive region is shown by the black solid line. The Si detectors are indicated by the blue solid lines. The direction of the incident beam is shown by the black dashed arrow. According to the simulation, the present field cage ensures that the distortion of the electric field is kept smaller than 0.4% within the sensitive volume.

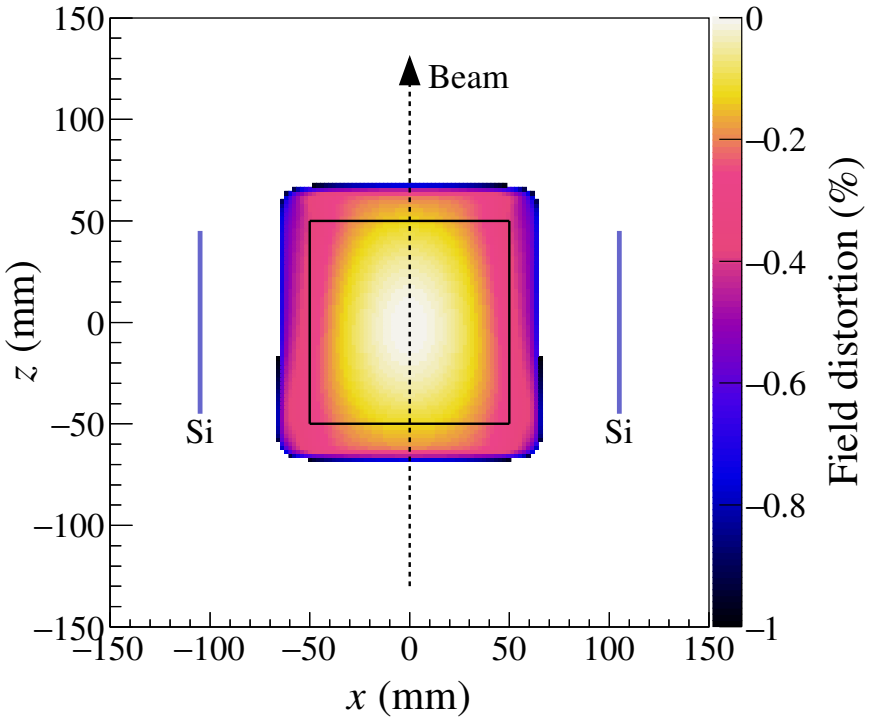

Figure 2.1: Distortion of the vertical electric field with respect to the field at the center of the TPC. The distortion is defined by Eq. (2.1). The calculation was performed using computer codes Garfield [118] and neBEM [119].

[1] SM5 by JAPAN FINECHEM COMPANY, INC., Tokyo, Japan

The negative high voltage of the cathode plate is applied via a low-pass filter which consists of a 1000 kΩ resistor and a 1000 pF capacitor. This low-pass filter suppresses the ripple of the high voltage module[2] for the cathode plate to reduce the noise on the Si detectors. Since the measured ripple frequency of the high voltage module was about 60 kHz, the cutoff frequency of the low-pass filter was determined to be $f_c = 1/(2\pi C_f R_f) = 1.6$ kHz.

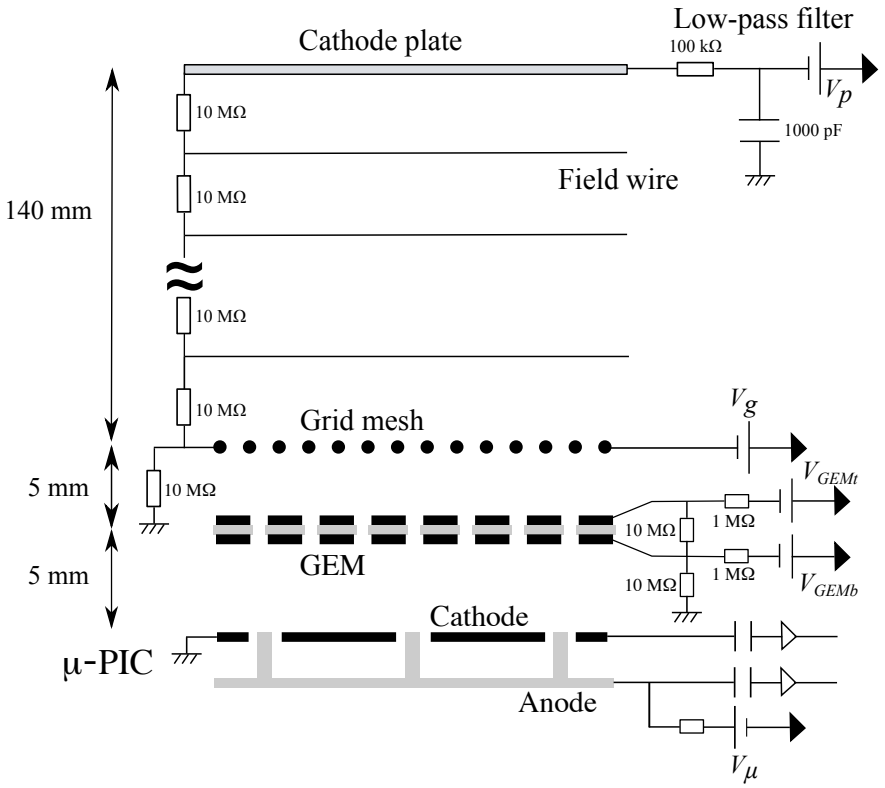

Figure 2.2: Electric circuit of the field cage, GEM, and μ-PIC.

2.3 Si detectors

The four Si detectors are placed at 30 mm away from the TPC field cage to detect high-energy recoil particles. Two Si detectors are installed at the left side of the TPC and the other two Si detectors are installed at the right side. Figure 2.3 shows a photograph of the two Si detectors. Each Si detector has a sensitive area of 90×60 mm^2 and a thickness of 500 μm. These Si detectors can stop alpha particles with energies up to 33 MeV if the particles hit the detectors perpendicularly.

[2]HARb-15N by Matsusada Precision Inc., Shiga, Japan

The surfaces of the Si detectors are grounded while the cathode plate is applied high voltage (typically -5 kV). Since the shortest distance from the Si detectors to the cathode plate is as short as 30 mm, we should take care with the electric discharge between them. If an electric discharge occurs, a large current flows in the Si detectors which may damage the Si detectors and the readout circuits. Thus the Si detectors are protected from the electric discharge by putting an electrostatic shield between the cathode plate and the Si detectors. Since the electrostatic shield is grounded, the discharge occurs not to the Si detectors but to the shield. The electrostatic shield is made of the Cu-Be wires with a diameters of 125 μm soldered on a glass epoxy (grade FR4) frame with a pitch of 5 mm as shown in Fig. 2.4. These wires are connected to the vacuum chamber through the red cable shown in the figure. During the measurement with the ^{10}C beam, several discharges occurs, but none of the Si detectors were damaged.

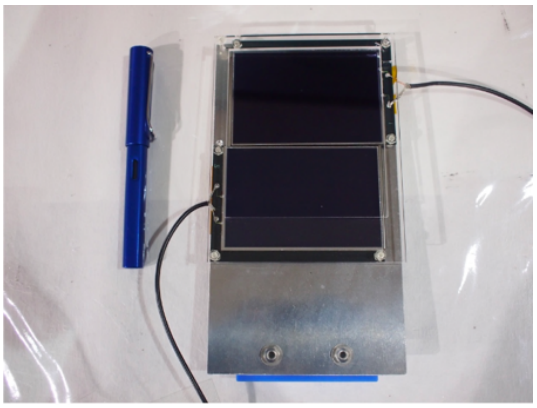

Figure 2.3: Photograph of two Si detectors.

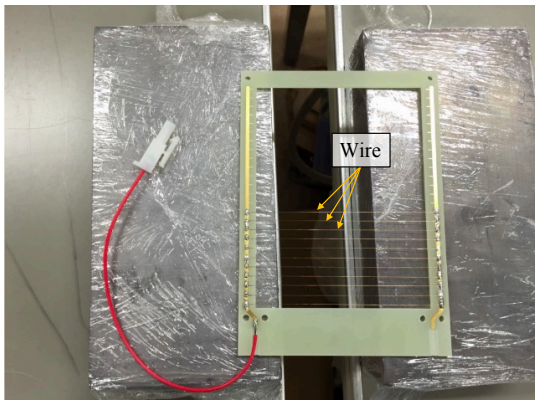

Figure 2.4: Electrostatic shield made of Cu-Be wires to protect the Si detectors.

2.4 μ-PIC

The drift electrons are multiplied by the μ-PIC placed 10 mm below of the grid mesh. The μ-PIC also provides the two-dimensional position information of the electrons.

The μ-PIC was developed in 2001 [120] and continuously under improvement by the cosmic-ray group at Kyoto University. It is one of micro pattern gaseous detectors (MPGD). It achieves high position resolution owing to a fine readout pitch while the number of the readout channels is relatively small. The μ-PIC has been successfully employed in Compton cameras for gamma-ray imaging [121–124], in the dark matter search experiment [125, 126], and in neutron imagings [127, 128].

A schematic structure of the μ-PIC is shown in Fig. 2.5. The μ-PIC has a sensitive area of 102.4×102.4 mm^2. It is constructed using a print circuit board (PCB) technology. The μ-PIC consists of 256 cathode electrode strips, each with a width of 314 μm. They are fabricated on a 100-μm-thick polyimide base at 400-μm intervals. Each cathode strip has

256 holes along the strip, each with a 256-μm diameter, arranged at equal intervals of 400 μm. At the center of each cathode hole, an anode pixel of 50-μm diameter is fabricated. The anode pixels are extended to the back side of the base and connected to form the anode strips which are perpendicular to the cathode strips. A positive high voltage is applied to the anode strips while the cathode strips are grounded. A strong electric field, enough to occur an electron avalanche, is formed around the anode pixels.

Each strip of the anode or cathode is connected to the readout board to provide a two-dimensional image of the charged particles. The number of the readout channels is 256 for the anode strips and 256 for the cathode strips.

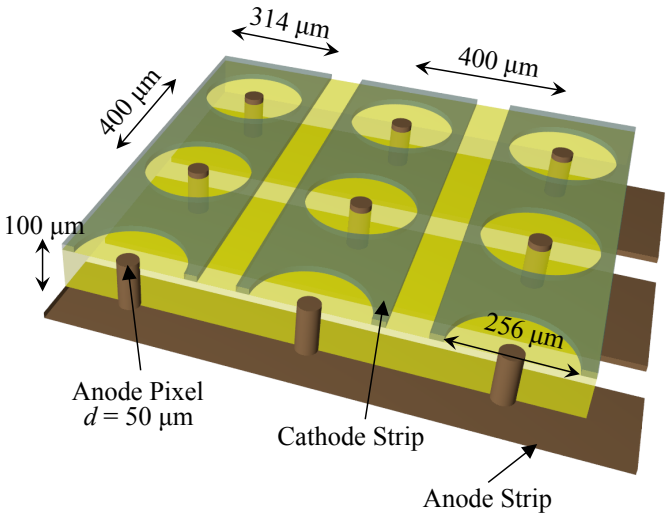

Figure 2.5: Schematic structure of the μ-PIC.

2.5 GEM

A GEM is installed between the grid mesh and the μ-PIC for the pre-amplification of the electrons. Figure 2.6 shows an photograph of a GEM [129]. The GEM is a thin polymer sheet whose from and back sides are coated with thin copper layers. The sheet is chemically perforated by holes with a high density, typically 100 holes per square mm [130]. A high voltage of typically 300 V is applied between the front and the back sides of the GEM which forms a strong electric field in the holes. The electrons enter the holes and are multiplied by the strong electric field. The GEM with a sensitive area of 100×100 mm^2, which is almost same as that of the μ-PIC, was commercially purchased[3] and mounted on a frame made of Macor to install in MAIKo. The hole geometry of the GEM is the so-called standard GEM: diameter of 70 μm and 140 μm apart in a triangular pattern. The thickness of the GEM is 100 μm, which is twice as thick as the standard one and achieves higher gas gain. The

[3]Manufactured by SciEnergy Inc., Kanagawa, Japan.

electric circuit to apply high voltages on the GEM electrodes is shown in Fig. 2.2.

The two-stage electron amplification with the GEM and μ-PIC contributes to the stable operation of the detector system because it reduces the discharge probabilities. The electric fields formed around the GEM or μ-PIC can be smaller compared to that in the amplification system with the μ-PIC only, while keeping the total gas gain high. As reported in Ref. [41], the operation of the TPC without the GEM was unstable during a test measurement with the He(93%)+CO_2(7%) gas at 430 hPa due to the electric discharges of the μ-PIC. After the test measurement, we introduced the GEM to the MAIKo TPC and the operation without any discharge of the GEM or μ-PIC became possible even with the smaller fraction of the CO_2 gas.

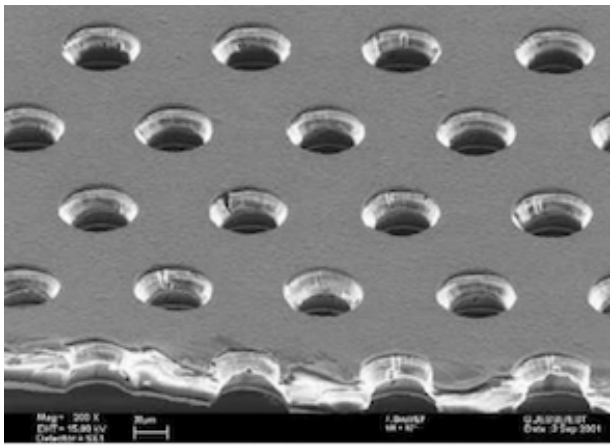

Figure 2.6: Photograph of a GEM. Taken from Ref. [129].

2.6 Readout electronics

The anode and cathode strips of the μ-PIC are connected to the capacitor and resistor (CR) circuit boards. The CR circuits consist of 1-GΩ resistors and 100-pF capacitors. Figure 2.7 shows a photograph of the CR circuit board. The CR circuit boards are mounted on the TPC chamber and directly connected to the μ-PIC board in the TPC chamber via a hole on the top flange of the chamber. The CR circuit boards are sandwiched between the top flange and another blind flange with O-rings to seal the TPC gas, *i.e.*, these CR circuit boards work also as the vacuum feed-through for the μ-PIC analog signals.

The analog signals from the μ-PIC are processed by the dedicated readout electronics boards called Iwaki board [131]. The Iwaki boards are connected on the CR circuit boards as shown in Fig. 2.7. Each Iwaki board processes signals from 128 channels, thus the four Iwaki boards are used in MAIKo: two boards for the 256 anode strips and the other two boards for the 256 cathode strips.

A block diagram of the signal processing in the Iwaki board is shown in Fig. 2.8. The

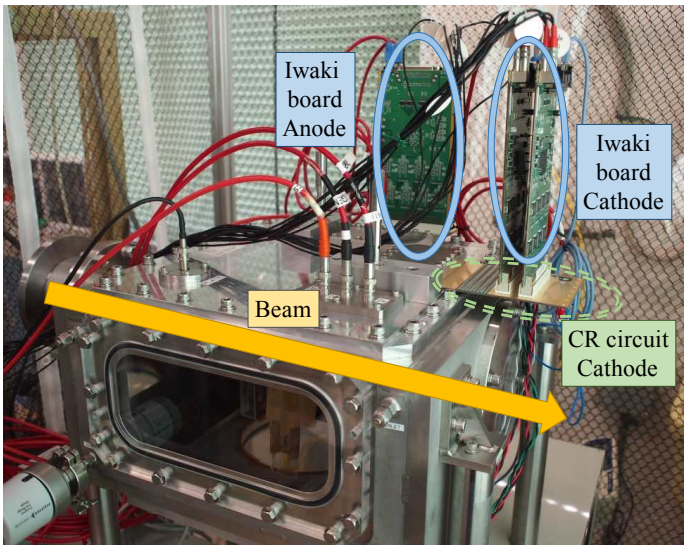

Figure 2.7: Photograph of the CR circuit board and the Iwaki boards. The CR circuit board for the cathode strips is circled by the green dashed lines and the Iwaki boards are circled by the blue solid lines.

Table 2.1: Performances of the FE2009bal ASIC.

Number of channels	16
Peaking time	30 ns
Gain of the amplifier	800 mV/pC
Dynamic range	-1 to $+1$ pC
Cross talk	$< 0.5\%$
Noise	$\sim$ 6000 electrons
Power consumption	18 mW/ch

input signals from 128 strips on the μ-PIC are preamplified, shaped, and discriminated by the eight application specific integrated circuit (ASIC) chips named FE2009bal [131]. Each FE2009bal chip processes 16 channels of the analog signal. The performances of the FE2009bal chip are summarized in Table 2.1. The threshold levels for the individual channels of the discriminators on the ASIC chips are remotely controlled via the SiTCP connection.

The high or low status of the discriminators is synchronized with a 100-MHz clock to provide timing information of drift electrons. The ASIC chips also output the shaped analog signals of the sum of the adjacent 32 strips. These sum of the analog signals can be read out from the 4 LEMO connectors for the signal check or making the internal triggers for the data acquisition. These analog signals are also digitized by 25-MHz 8 bit flash analog-to-digital converters (FADCs). The clock-synchronized status of the discriminators and the digitized waveforms of the analog signals are continuously recorded in a ring buffer implemented in

a field-programmable gate-array (FPGA) chip for a duration of 10.24 μs. When a trigger signal is provided to the Iwaki boards, the digitized data stored in the ring buffer are written out to two VME memory modules after the data formatting in the FPGA. The TPC data are acquired event-by-event together with the data from the Si detectors and the other beamline detectors via the VME bus using the standard data acquisition system for RI beam experiments at RCNP, which was originally developed at RIKEN [132].

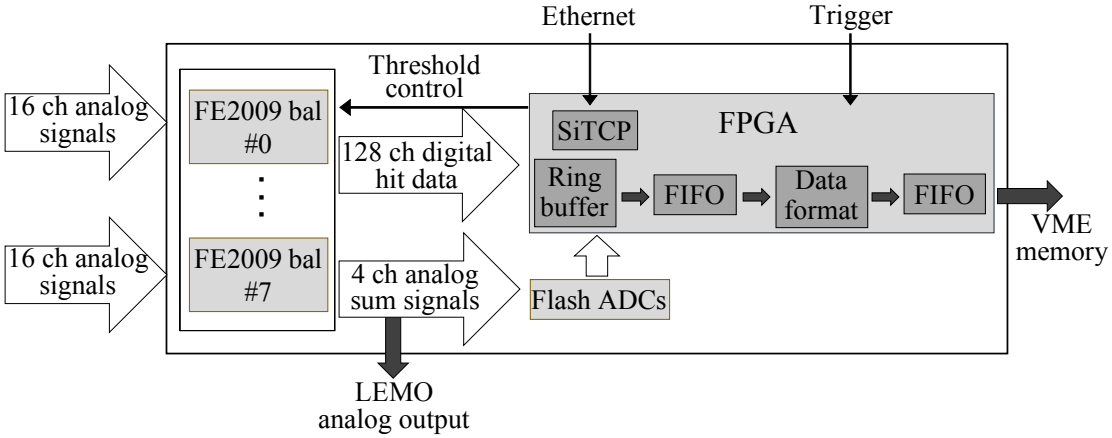

Figure 2.8: Block diagram of the signal processing in the Iwaki board.

By plotting the clock numbers when the discriminators are in the high status as a function of the strip number, two black-and-white images with 256 $\times$ 1024 pixels are obtained. Each image represents the particle trajectories projected onto the plane perpendicular to the anode or cathode strips as shown in Fig. 2.9. Since the anode strips are perpendicular to the beam axis and the cathode strips are parallel to the beam axis, the anode image gives the side view of the particle trajectories while the cathode image gives the front view.

2.7 Selection of TPC gas

The TPC gas should be composed mainly of the He gas to perform the alpha inelastic scattering inside the TPC. The operation without any quenching gas is ideal from a view of the backgrounds, however, the MAIKo TPC could not be operated stably with the pure helium gas due to the discharges at the cathode plate or the μ-PIC. Therefore, a quenching gas should be added to the gas for the stable operation. Hydrocarbon gasses such as iso-butane or methane gas have been widely used as a quenching gas in various gaseous radiation detectors, but these gasses cause the background events due to the (p, p') scattering. Because the (α, α') and (p, p') scatterings are kinematically similar, distinguishing the (α, α') events from the (p, p') events is not easy although the background events due to the carbon are easily distinguished from the (α, α') scattering owing to the kinematic effect. Another candidate for the quenching gas is CO_2 or CF_4. Considering that CO_2 contains less number of atoms

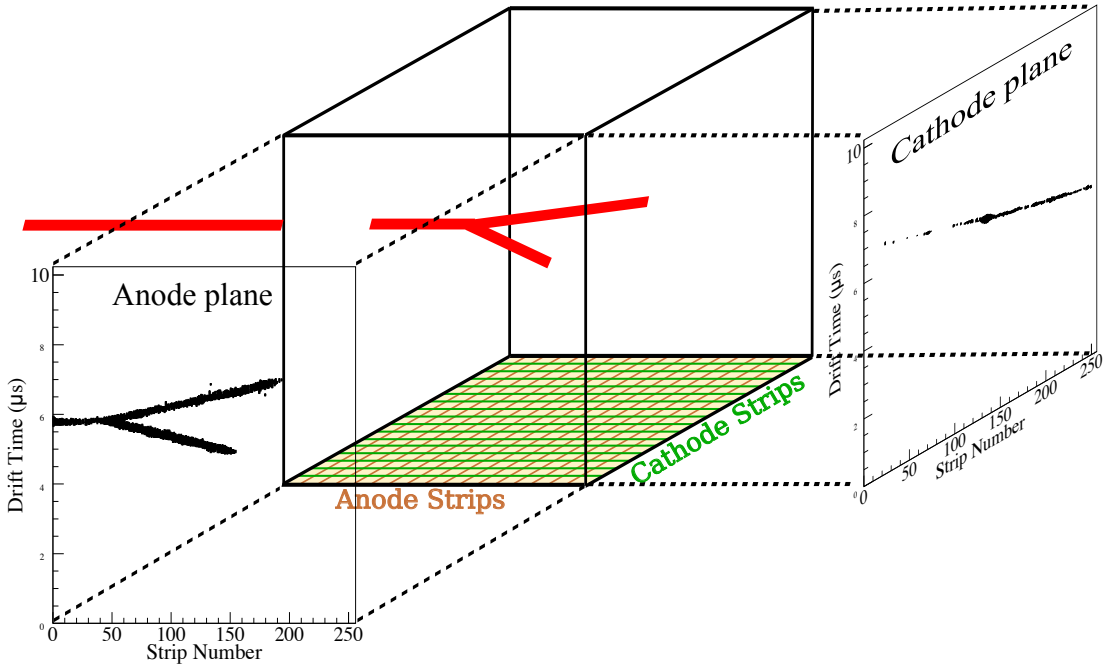

Figure 2.9: Three-dimensional particle trajectories in the MAIKo TPC and their projections on the anode and cathode planes.

than CF_4, we chose the CO_2 gas for the quenching gas. The fraction of the CO_2 gas should be as small as possible. We carried out test measurements and found that 4% is the minimum mixing ratio to operate the TPC stably.

2.8 Gas handling system

We developed a gas handling system to flow the mixture gas and suppress the gas impurity inside the TPC chamber. A schematic diagram of the MAIKo TPC gas handling system is shown in Fig. 2.10. The route of the gas flow is indicated by the red thick solid lines. The He and CO_2 gasses were individually supplied into the TPC chamber with two mass flow controllers[4] (MFC) to keep the mixture ratio of 96:4 and the flow rate constant. The total flow rate during the present α+^{10}C experiment was 100 cm^3/min. The pressure and temperature inside the chamber were monitored with a diaphragm gauge[5] and a Pt-100 thermometer[6], respectively. The humidity inside the TPC chamber was also measured using a capacitive dew-point transmitter[7]. The measured gas pressure, temperature, humidity,

[4]HM1000 by TOKYO KEISO CO., LTD., Tokyo, Japan
[5]VHR(G3) by VALCOM CO., LTD., Osaka, Japan
[6]TN2531 by ifm electronics gmbh, Essen, Germany
[7]Easidew Online by Michell Instruments Ltd., Cambridgeshire, England

and gas flow rate at the MFCs were digitized by analog-to-digital converter (ADC) modules and periodically read out by a programmable logic controller[8] (PLC). The mixture gas inside the TPC chamber was continuously exhausted using a oil-free scroll pump[9]. A piezo valve[10] was installed between the pump and the TPC chamber. The PLC calculated the density of the TPC gas from the pressure and temperature and a digital-to-analog converter (DAC) module output a voltage level according to the gas density to the piezo valve controller. The aperture of the piezo valve was automatically tuned by a proportional-integral-differential (PID) controller to keep the gas density constant referring to the DAC output.

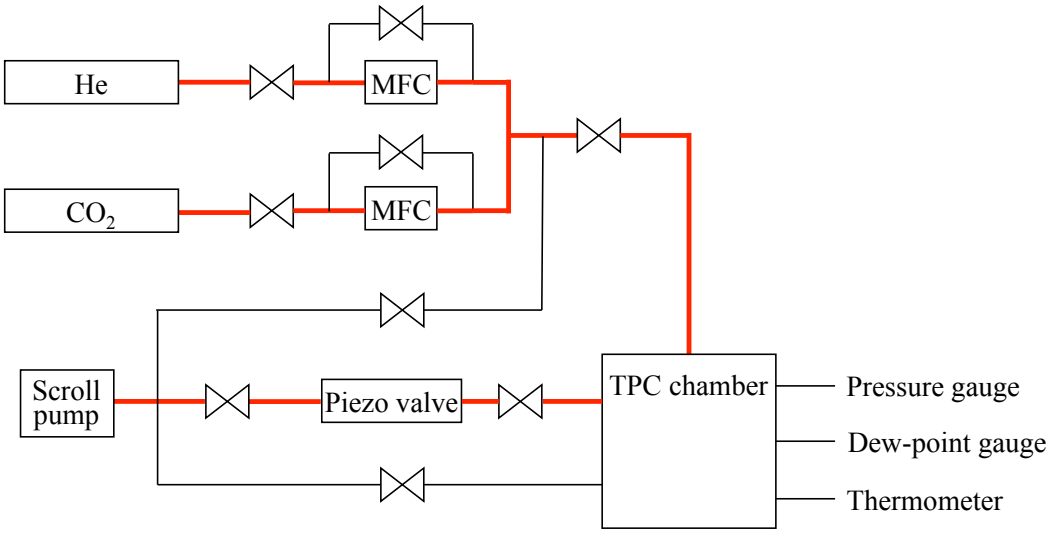

Figure 2.10: Schematic diagram of the MAIKo TPC gas handling system. The gas flow route is indicated by the red thick solid lines.

[8] F3RP61 by Yokogawa Electric Corporation, Tokyo, Japan
[9] FOSSA FO by Kerr Pump & Supply Inc., Michigan, USA
[10] PV-1501MC and PCU-2100 by HORIBA, Ltd., Kyoto, Japan

3 EXPERIMENT

3.1 Primary beam

The first physics experiment (E463) to measure the α+^{10}C scattering was carried out at the cyclotron facility of Research Center for Nuclear Physics (RCNP), Osaka University. Figure 3.1 shows an overview of the RCNP cyclotron facility. The ^{10}C secondary beam was produced through the projectile fragmentation reaction from a ^{12}C primary beam. The primary beam from the super-conducting electron cyclotron resonance (SCECR) ion source was first accelerated to 22 MeV/u with the K140 azimuthally varying field (AVF) cyclotron and then further accelerated to 96 MeV/u with the K400 six-sector ring cyclotron. This energy is the maximum energy with the ring cyclotron. The intensity of the ^{12}C beam was 50–100 pnA. The ^{12}C beam was transported to the exotic nuclei (EN) beamline to obtain the ^{10}C secondary beam.

3.2 Production of the ^{10}C secondary beam

The ^{12}C primary beam bombarded on a ^{9}Be production target with a thickness of 450 mg/cm^2 at the F0 focal plane. The size of the beam spot at F0 was typically 1 mm in diameter. The ^{10}C nucleus was separated from other nuclei with the fragment separator at the EN course.

Figure 3.2 shows a schematic layout of the EN course fragment separator. The beamline was originally developed in 1990s [133, 134]. It was upgraded in 2013 [135] in which the beamline was extended from the F2 focal plane to the F3 focal plane to improve the purity of the secondary beam. The fragment separator consists of two dipole magnets (D1 and D2) and nine quadrupole magnets (Q1–Q9). Some of the basic properties of the EN course fragment separator are listed in Table 3.1.

The separation of the secondary particles was performed by the following principles. The secondary particles produced at the F0 focal plane were first analyzed by the D1 magnet. After the D1 magnet, the particles satisfying Eq. (3.1) were selected at the first focal plane (F1).

$$\frac{Z}{A} = \frac{p_{\mathrm{nucleon}}}{e(B\rho)_{\mathrm{D1}}}, \tag{3.1}$$

where Z and A are the proton and mass numbers, p_{nucleon} is the momentum per nucleon, and $(B\rho)_{\mathrm{D1}}$ is the magnetic rigidity of the D1 magnet. Here we note that the ions from the projectile fragmentation are fully ionized in the present energy region, thus the electric charge of the ions is equal to its atomic number Z. After the momentum selection, the fragments

Table 3.1: Properties of the EN course fragment separator.

Configuration	Q-Q-Q-D-SX (F1, dispersive focus) SX-Q-D-Q-Q-Q (F2, double achromatic focus) Q-Q (F3, double achromatic focus)
Maximum magnetic rigidity	3.4 Tm
Bending radius	2.2 m
Bending angle	60°
Energy degrader at F1	uniform thickness
Energy dispersion at F1	8.66 mm/%
Momentum dispersion at F1	17 mm/%
Momentum acceptance to F2	±4%
Horizontal angular acceptance to F2	±20 mrad
Vertical angular acceptance to F2	±14 mrad
Horizontal magnification at F2	2.0
Vertical magnification at F2	1.4

Table 3.2: Parameters of the beamline during the ^{10}C measurement.

Parameter	Value
Magnetic rigidity of D1	2.3 Tm
F1 degrader	Aluminum 2 mm
F1 collimator	±6 mm
Magnetic rigidity of D2	2.1 Tm
F2 collimator	±15 mm

penetrated a degrader at the F1 focus point. The energy loss through the degrader depends on A and Z, thus the the magnetic rigidities of the particles are different according to A and Z. The particles are spatially separated after the D2 magnet. The particles at the second focal plane (F2) were purified by a pair of horizontal collimators.

After the separation, the purified beam was focused onto the MAIKo active target by the Q8 and Q9 magnets. The Q8 and Q9 magnets were used to focus vertically and horizontally, respectively. The energy spread of the secondary beam was determined by the width of the slits at F1. The parameters of the fragment separator during the present ^{10}C measurement are summarized in Table 3.2. The average energy of the ^{10}C beam before MAIKo was 68 MeV/u and the energy spread was less than ±1%.

During the tuning of the secondary beam, the beam was detected, identified, and monitored with a 320-μm-thick silicon detector (F3 Si) installed at upstream of MAIKo at F3

and a 1-mm-thick plastic scintillator (F3PL) placed downstream of MAIKo. The details of the F3PL are described in Sec. 3.3.2. Figure 3.3 shows the correlation between the energy loss of the beam particles in the F3 Si detector and the time of flight from the F0 target to the F3PL. The time of flight was obtained from the timing information of the F3PL and the radio-frequency signal from the AVF cyclotron. This correlation was used for the particle identification (PID) of the secondary beam. It is seen that ^{10}C is clearly separated from ^{12}C and ^{11}C. Because the purity of the ^{10}C particle was as high as 96%, event-by-event PID was not necessary during the measurement, and we did not use the F3 Si detector after the beam tuning.

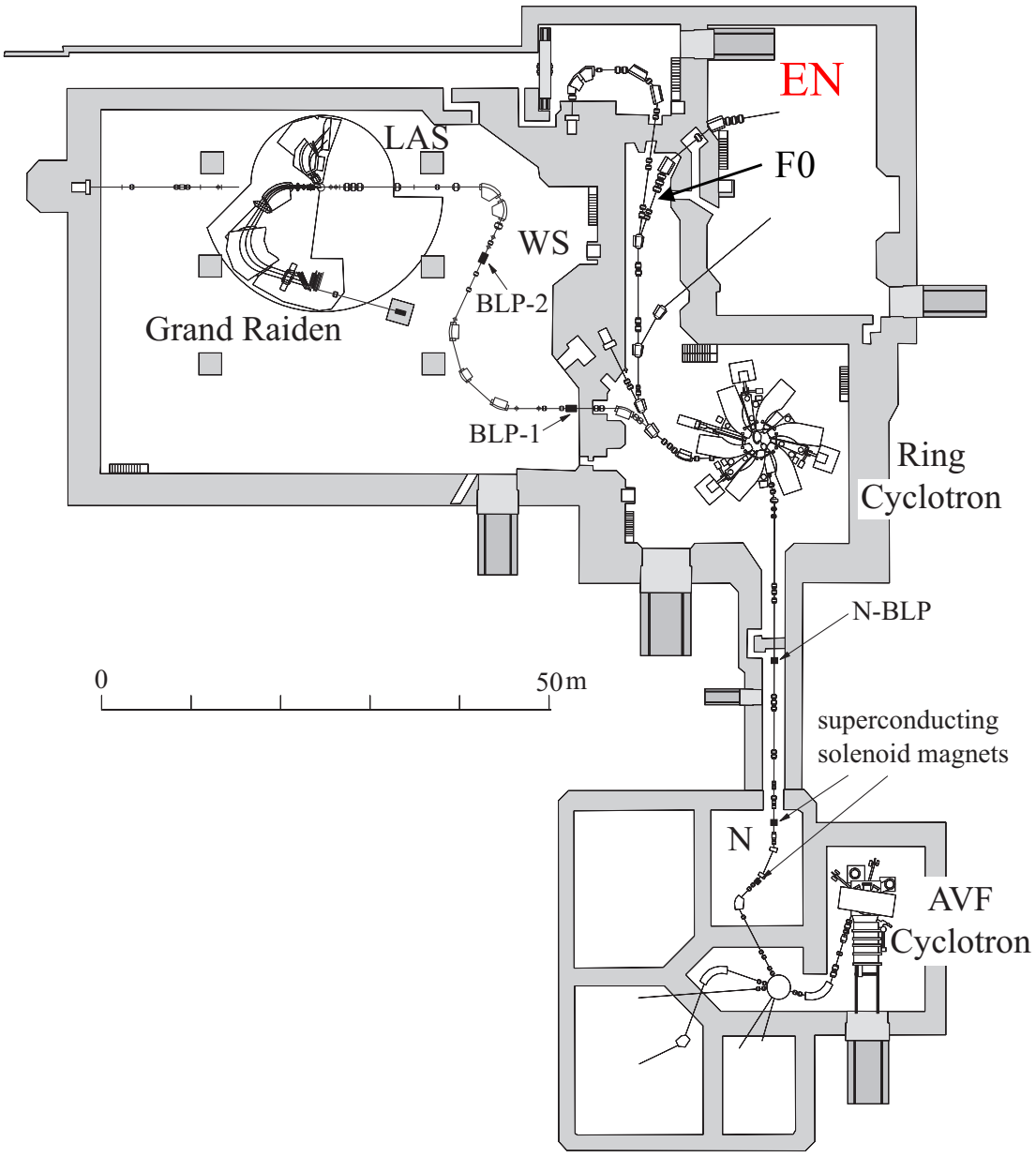

Figure 3.1: Overview of the RCNP cyclotron facility.

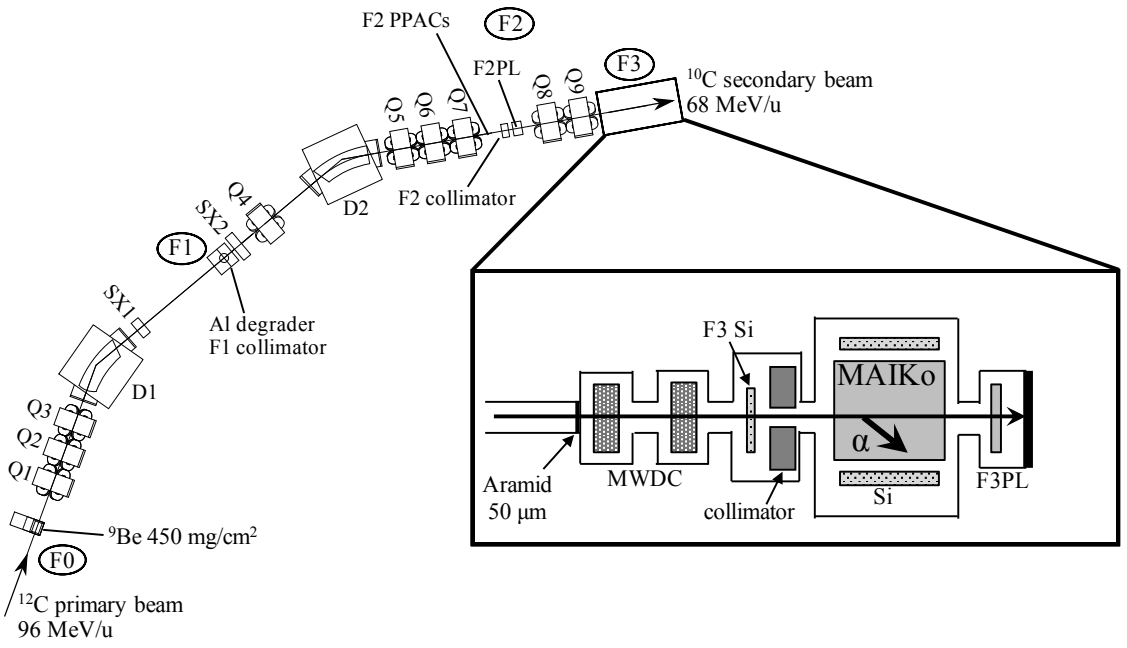

Figure 3.2: Schematic view of the EN course fragment separator. The setup near the F3 focal plane is shown in the inset.

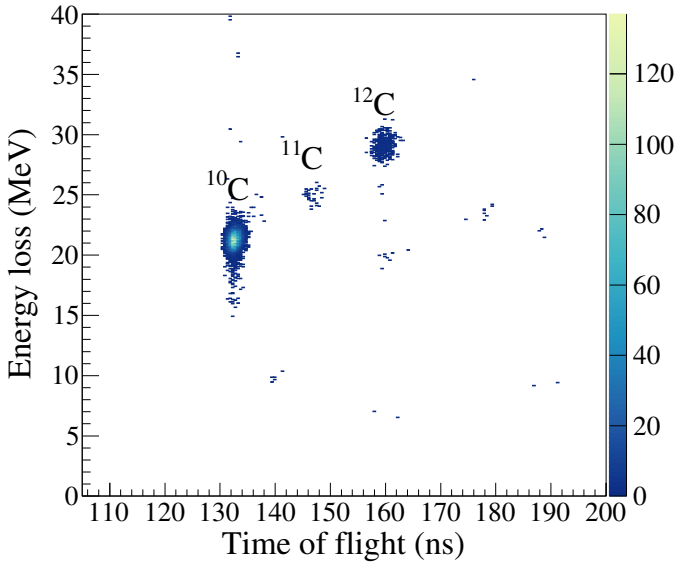

Figure 3.3: Correlation between the energy loss in the F3 Si and the time of flight from the F0 target to the F3 plastic detector.

Table 3.3: Specifications of each MWDC.

Configuration	X-X'-Y-Y'-X-X'-Y-Y'
Sensitive area	77.5 mm (X)×77.5 mm (Y)
Drift length	2.5 mm (Anode-Potential)
Gap	4.8 mm (Cathode-Cathode)
Anode wire	Au plated W-Re (d =16 μm)
Potential wire	Au plated Al (d =80 μm)
Cathode foil	Alminized Kapton (t =7.5 μm)

3.3 Beamline detectors

The setup at F3 is shown in the inset of Fig. 3.2. The incident trajectory of the ^{10}C was monitored with the two low-pressure multi-wire drift chamber (MWDC) installed at upstream of MAIKo. After the MWDCs, the ^{10}C beam was horizontally collimated by a pair of tungsten collimators with thicknesses of 10 mm. The aperture of the collimators was set at 20 mm. The intensity of the ^{10}C beam was measured with the F3PL installed at downstream of MAIKo. Each detector is described in detail in the following sections.

3.3.1 Low-pressure MWDC

In the previous experiments at the EN course [136–140], the incident position of the beam was measured using the parallel-plate avalanche counters (PPAC) [141]. However, the detection efficiency of the PPACs for ^{10}C at 68 MeV/u was not good enough to monitor the beam position. Therefore, we developed a low-pressure MWDC system at RCNP.

The system is an imitation of the similar system developed for the ESPRI experiment to measure the elastic scattering of protons with RI beams at RIKEN [142]. The system consists of two sets of MWDCs, which are installed in a vacuum chamber. The relative distance of the two detectors is 600 mm and the distance from the downstream MWDC to the entrance of MAIKo TPC is 733 mm. The vacuum chamber of the MWDCs and the MAIKo chamber was connected without any separation window films, thus the MWDCs were operated with the same gas as the MAIKo TPC.

The specifications of the MWDC are summarized in Table 3.3. Each MWDC consists of four planes (X-X'-Y-Y'-X-X'-Y-Y'). Structure of each plane is shown in Fig 3.4. Each plane consists of 16 anode wires with a pitch of 5 mm. Between the anode wires, potential wires are placed. These wires are sandwiched by the cathode planes with a gap of 4.8 mm. Negative high voltages are applied to the potential wires and the cathode planes. Signals from the 256 anode wires are amplified, shaped, and discriminated with 16 ASD cards. The discriminator output from the ASD cards are recorded with two multi-hit time to digital converters (TDC).

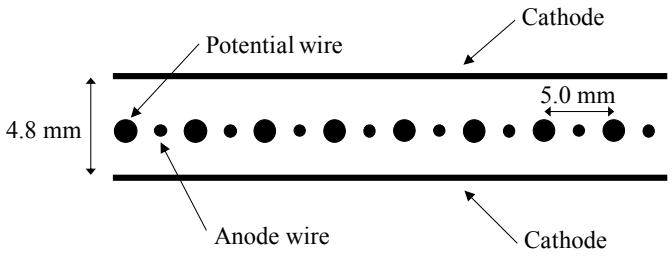

Figure 3.4: Structure of each MWDC plane.

3.3.2 F3 plastic scintillator

We developed a plastic scintillator system (F3PL) to measure the intensity of the ^{10}C beam at downstream of MAIKo. Figure 3.5 shows a photograph of the F3PL. The plastic scintillator has a dimension of 100 mm in width, 110 mm in height, and 1 mm in thickness. The plastic scintillator is installed inside a vacuum chamber which is connected to the MAIKo vacuum chamber. It can be moved out from the beamline by hand. The lights emitted from the scintillator pass through the light guides installed inside the chamber and converted to an electric signal by two photo-multiplier tubes (PMT) placed at the left and right sides. The light guides are also used to separate the vacuum chamber volume from the outside air. While the plastic scintillator is installed in the TPC gas atmosphere, the PMTs are placed outside of the vacuum chamber to avoid exposure to the TPC gas containing He.

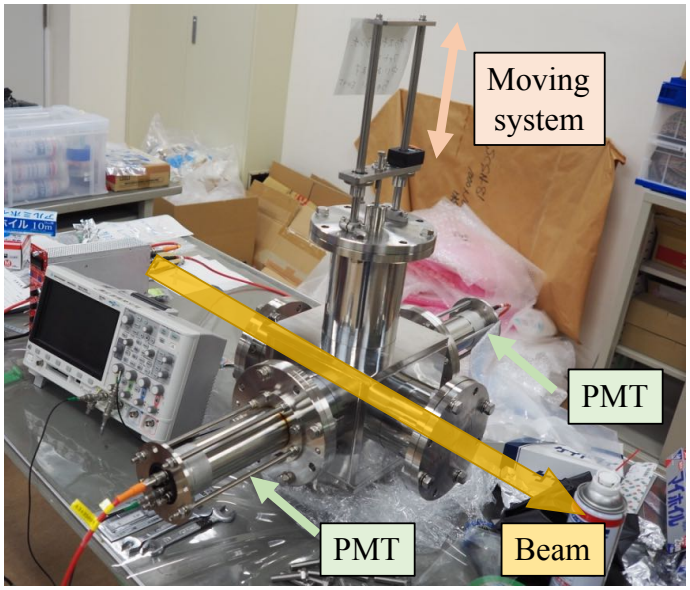

Figure 3.5: Photograph of F3PL.

3.4 Data acquisition

Since the recoil alpha particles from the α+^{10}C elastic and inelastic scattering at $q \sim 0.5$ fm^{-1} are emitted at $\theta_{\rm lab} \sim 90°$, the trigger signal for the data acquisition was made with the Si detectors or the cathode strips of MAIKo. Figure 3.6 shows a schematic drawing of the trigger circuit. As described in Sec. 2.6, the Iwaki readout boards output the shaped analog signals of the sum of the 32 strips (8 channels for the anode strips and 8 channels for the cathode strips). The trigger signal induced by the cathode strips was generated by to a leading edge discriminator (L.E.D.) module for the shaped analog signals. To suppress the triggers due to the beam particles, Ch. 2, 3, and 4 of the shaped analog signals from the cathode strips were excluded from the trigger as shown in Fig. 3.7.

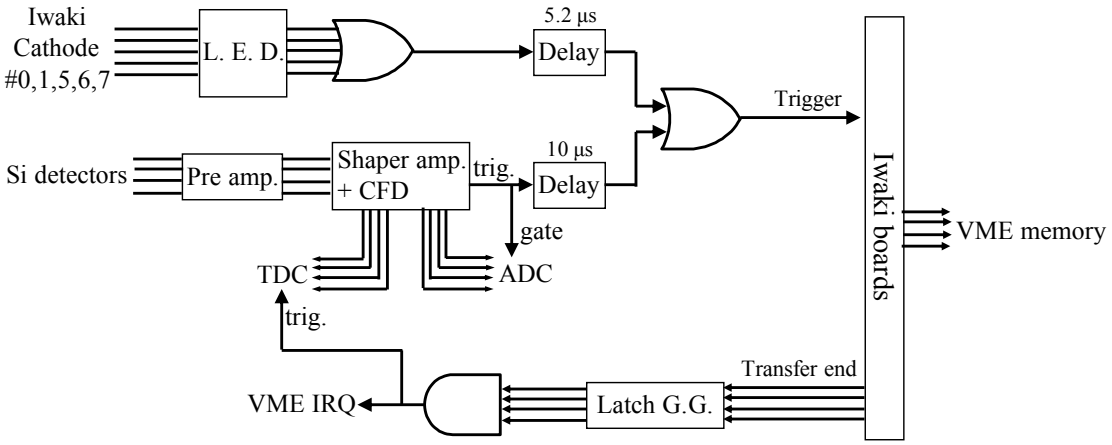

Figure 3.6: Schematic diagram of the trigger circuit.

The analog signals from the Si detectors were amplified and shaped by a preamplifier module and a shaping amplifier module, respectively The shaping amplifier module was also equipped with a constant fraction discriminator module to output a trigger signal. The trigger signal from the Si detectors and the cathode strips were summed and transmitted to the Iwaki boards for the data acquisition (DAQ). After receiving the trigger signal, the Iwaki boards transferred the TPC data to the VME memory modules. This procedure took typically 100 μs depending on the data size. Each Iwaki board outputted a signal to latch a gate generator (GG) module when it finished transferring the data. When all of the Iwaki boards finished transferring the data, all of the four channels of the GG module were latched and an interrupt signal was sent to the VME system.

The DAQ system read the data from the TPC and the other detectors event-by-event. The VME memory module for the TPC had double-buffer memories. After the interruption, the DAQ system first switched the buffer for writing data to the another one, and then read the data of the Si detectors and the beamline detectors without reading the data of the TPC. The used readout modules are listed in Table 3.4. After the readout, the DAQ system

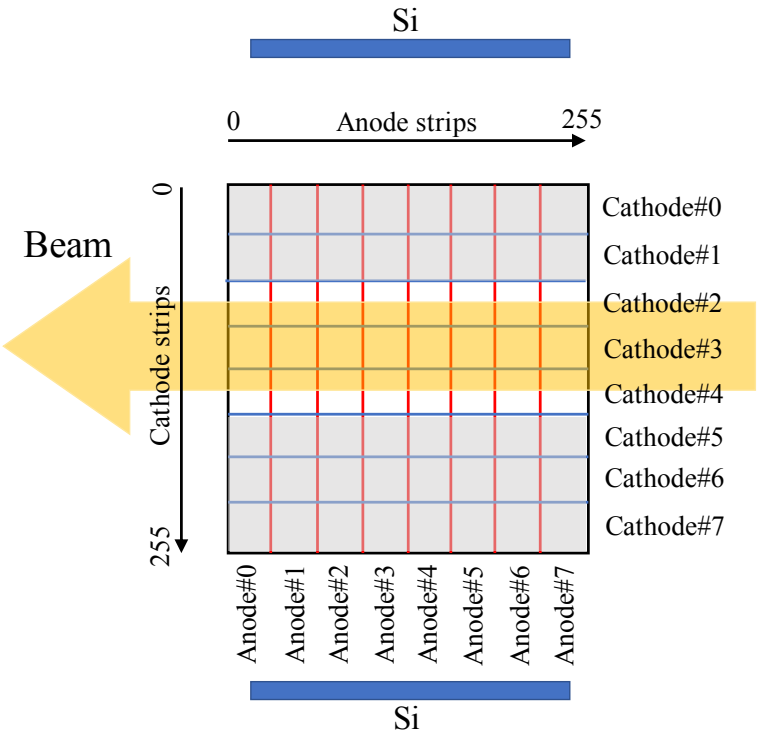

Figure 3.7: Layout of the μ-PIC anode and cathode strips. The broad orange arrow shows the direction and approximate width of the ^{10}C beam. The cathode analog signals in the shaded region were used to generate the trigger.

enabled the next interrupt signal. During waiting for the next interruption, the DAQ system read out the TPC data. This treatment helped to reduce the dead time of the readout. When the ^{10}C beam intensity was 77 kHz and the gas pressure was 500 hPa, the total trigger rate was 270 Hz. The live time ratio of the data acquisition was 88%.

3.5 Operation of MAIKo

3.5.1 TPC gas

The MAIKo TPC was operated with the He(96%)+CO_2(4%) mixture gas. The recoil alpha energy was determined from the range in the gas or the Si detectors. However, when the recoil alpha particles stop between the sensitive volume of the TPC and the Si detectors, the recoil energy cannot be determined. Because the insensitive energy region depends on the gas pressure, the TPC was operated at different gas pressure, 500 and 1000 hPa. When the gas pressure is 500 hPa, alpha particles with an energy of $E_\alpha < 1.0$ MeV stop in the sensitive volume of the TPC and alpha particles with $E_\alpha > 4.0$ MeV reach the Si detectors with their energies high enough above the detection threshold. When the gas pressure is

Table 3.4: List of the readout modules.

Module type	Module name
Si pre-amplifier	Mesytec MSI-8
Si shaping amplifier	Mesytec MSCF-16
VME CPU	Abaco V7768
TPC memory	ARKUS TMB-2
Si ADC	Mesytec MADC-32
Si TDC	CAEN V1190A
Plastic scintillator ADC	QTC+V1190A
Plastic scintillator TDC	V1190A
MWDC TDC	V1190A
VME scaler	CAEN V830
VME IRQ	CAEN V977

Table 3.5: Operating conditions of the TPC at 500 and 1000 hPa.

Pressure (hPa)	V_p (V)	V_g (V)	V_{GRMt} (V)	V_{GEMb} (V)	V_μ (V)	v (cm/μs)
500	-4300	-820	-616	-276	420	1.69(4)
1000	-7500	-820	-576	-276	350	1.69(7)

1000 hPa, alpha particles with $E_\alpha < 3.6$ MeV stop inside the TPC.

The vacuum chambers of the MAIKo TPC, MWDCs, and the F3PL detectors were connected without any separation materials and they were filled with the TPC gas. The gas volume was separated from the upstream beamline with a 50-μm-thick aramid foil which was installed at the entrance of the MWDC chamber. As described in Sec. 2.8, the gas density of the chamber was kept constant. Figure 3.8 shows the monitored temperature (a), density (b), and concentration of moisture (c) during the operation at 500 hPa. The temperature of the gas fluctuated about $\pm 0.3\%$ (± 1 K) during the measurement. The gas density variation due to this temperature fluctuation was compensated by adjusting the gas pressure inside the chamber by the piezo valve. As the result, the variation of the gas density was only 0.08%. Although the moisture of the gas was gradually increased during the measurement, it was kept as low as 220 ppm.

3.5.2 Measurement of the drift velocity

The applied high voltages to the cathode plate (V_p), grid mesh (V_g), top and bottom sides of the GEM (V_{GEMt} and V_{GEMb}), and μ-PIC anode (V_μ) (see Fig. 2.2) in the measurements at 500 and 1000 hPa are listed in Table 3.5.

Table 3.6: Measurement time for each beam particle and TPC gas pressure

Beam	Pressure (hPa)	Measurement time (hours)
^{10}C at 68 MeV/u	500	81
^{10}C at 68 MeV/u	1000	28
^{12}C at 94 MeV/u	500	6
^{12}C at 94 MeV/u	1000	2

Because the vertical position of the charged particles are determined by the electron drift time multiplied by the electron drift velocity, the drift velocities at the conditions listed in the table must be measured. The drift velocities were measured by using alpha particles from an ^{241}Am standard alpha source. The alpha particles were collimated at 30 degrees from the horizontal line, and injected to the TPC as illustrated in Fig. 3.9.

An example of the obtained anode images is shown in Fig. 3.10. The horizontal length (L_h) of the trajectory was determined from the number of the hit strips multiplied by 400 μm, since the horizontal length (L_h) of the trajectory in the sensitive volume was determined from the number of the hit strips multiplied by 400 μm. The vertical length (L_v) should be $L_v = L_h \tan 30^\circ$. Thus, the drift velocity was determined to be $v = L_v/D_t = L_h/D_t \tan 30^\circ$ from the measured horizontal length and drift time (D_t). For each event, the ratio L_h/D_t was obtained by fitting a straight line to the hit pixels in the anode image. Figure 3.11 shows the measured drift velocity when the gas pressure was at 500 hPa. The resolution of the drift velocity was limited by the hole size of the collimator. We fitted a Gaussian function to the distribution and took the central position of the peak for the drift velocity. The obtained drift velocities are listed in Table 3.5.

3.6 Summary of the measurement

Table 3.6 summarize the present measurements. We measured the α+^{10}C scattering at two different TPC gas pressures. In addition to the α+^{10}C measurements at 68 MeV/u, we also carried out similar measurements using the ^{12}C primary beam in order to check the consistency between the present measurement with MAIKo at 94 MeV/u and the previous measurement under the normal kinematic condition [143].

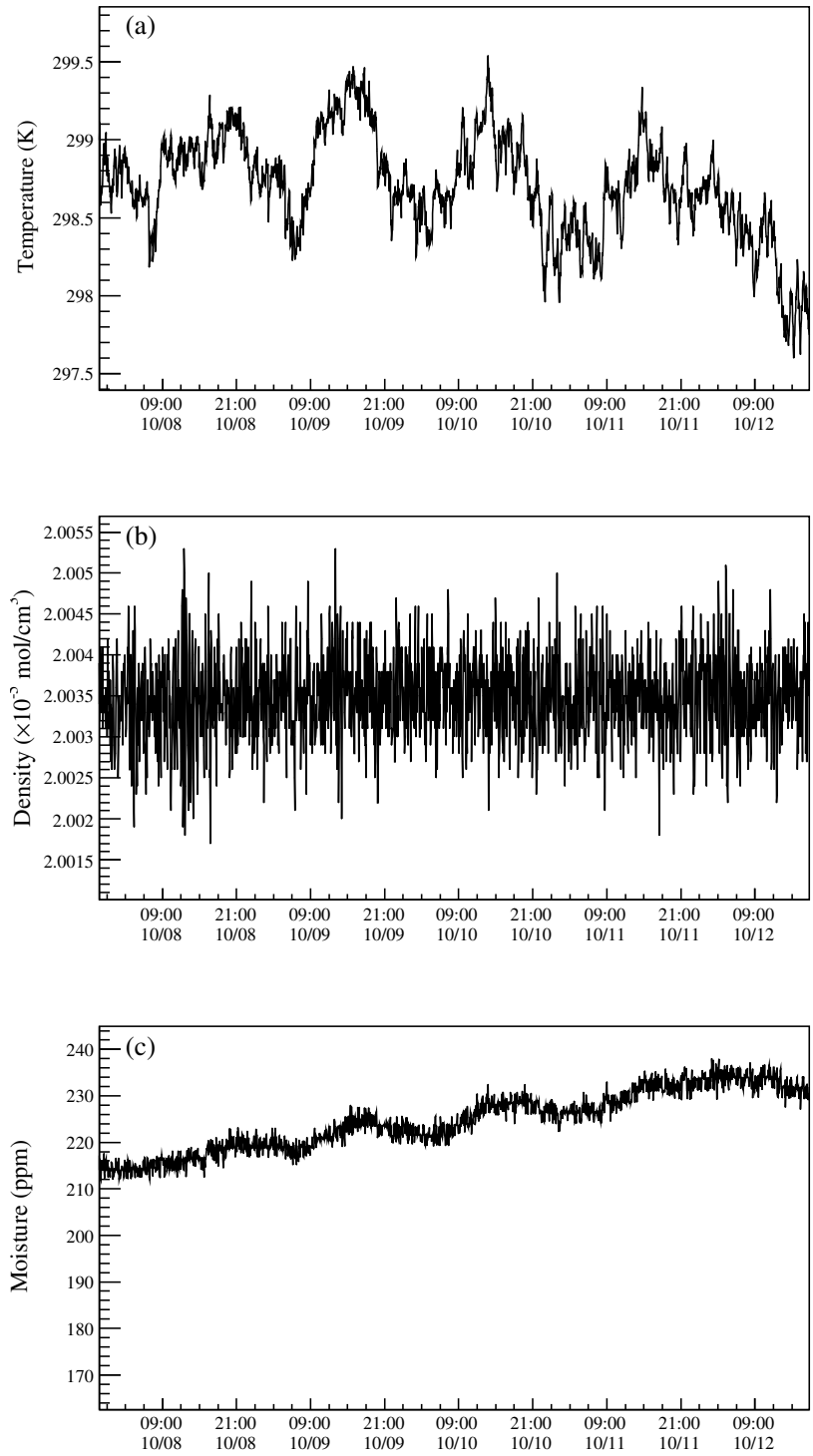

Figure 3.8: Monitored temperature (a), density (b), and moisture concentration (c) of the TPC gas during the measurement at 500 hPa from October 7 to 12, 2017.

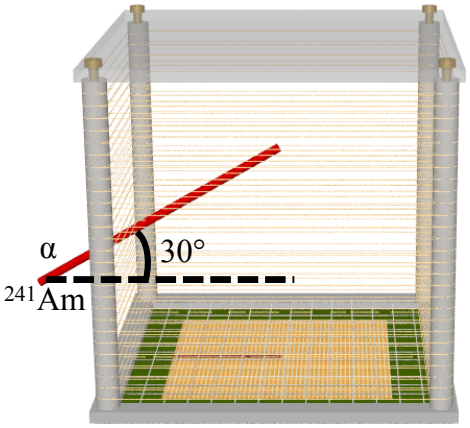

Figure 3.9: Schematic view of a trajectory of collimated alpha particle in the TPC.

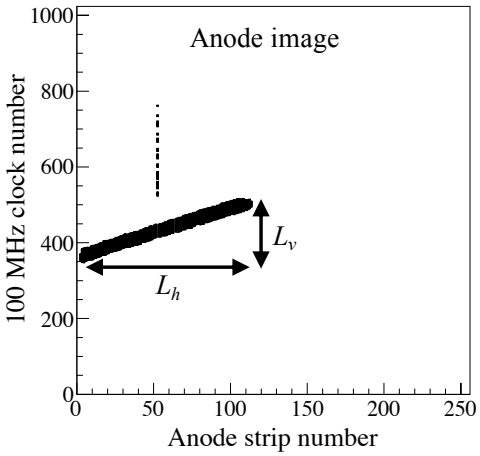

Figure 3.10: Example of the anode image acquired for a collimated alpha particle from ^{241}Am.

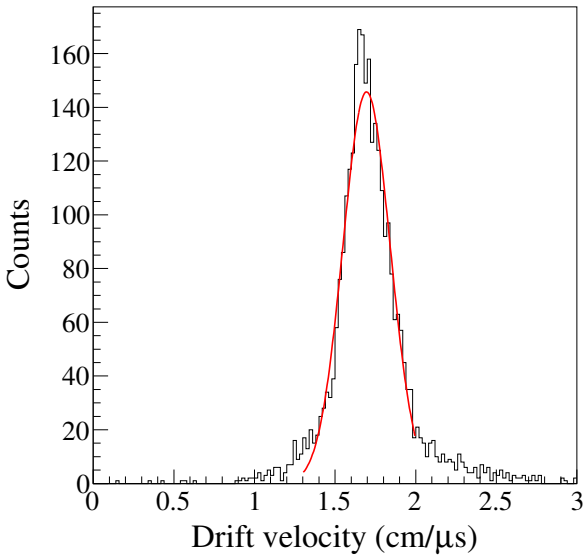

Figure 3.11: Measured drift velocity when the gas pressure in the TPC chamber was at 500 hPa.

4 DATA REDUCTION

In order to determine energies and angles of the recoil alpha particles for the missing-mass spectroscopy, we need to reconstruct the trajectories of the recoil alpha particles from the acquired data. As explained in Sec. 2.6, the acquired data contains two black-white images with 256×1024 pixels and 2×8 waveforms recorded by the 25-MHz FADCs. Using these information, we first distinguish the α+^{10}C scattering events and background events. After selecting the α+^{10}C scattering events, the trajectories of the recoil alpha particles were extracted to determine the recoil energies and angles. In this chapter, details of the data analysis procedures are described.

4.1 Examples of anode and cathode images

4.1.1 Examples of α+^{10}C scattering events

Two examples of the α+^{10}C scattering events are presented in Figs. 4.1 and 4.2. Figs. 4.1(a) and 4.2(a) represent the anode images, and Figs. 4.1(b) and 4.2(b) represent the cathode images. The pressure of the TPC gas was 500 hPa. Both of the examples record the trajectories of the incident ^{10}C particles and the recoil alpha particles. The trajectories of the unreacted ^{10}C particles were also recorded accidentally.

Since the beam axis was perpendicular to the anode strips and parallel to the cathode strips, the trajectories of the ^{10}C particles, which flew from the right side of the anode images, look horizontal lines in the anode images whereas they look elliptical shapes in the cathode images. On the other hand, the trajectories of the recoil alpha particles have large angles from the beam axis in the anode images and have longer lengths than the ^{10}C trajectories in the cathode images. The trajectories of the recoil alpha particles are thicker than those of the ^{10}C particles because dE/dx of the recoil alpha particles is larger than that of the ^{10}C particles.

After the scattering points, the trajectories of the scattered particles look different according to the excitation energy of ^{10}C. The known excited states and particle decay thresholds in ^{10}C are shown in Fig. 4.3. When ^{10}C was in the ground or the 2^+_1 (3.35 MeV) state below the particle decay threshold at $E_x = 3.73$ MeV, the trajectory of the scattered ^{10}C is recorded in the anode image with a similar thicknesses to that of the incident ^{10}C as shown in Fig. 4.1(a), since dE/dx of the scattered ^{10}C is almost same as that of the incident ^{10}C. On the other hand, when the scattered ^{10}C was excited above the particle decay threshold at 3.73 MeV, ^{10}C was not observed after the scattering point as shown in Fig 4.2(a) because such highly excited ^{10}C immediately decay into $2\alpha + 2p$. Even if ^{10}C decays to ^{8}Be, ^{9}B, and

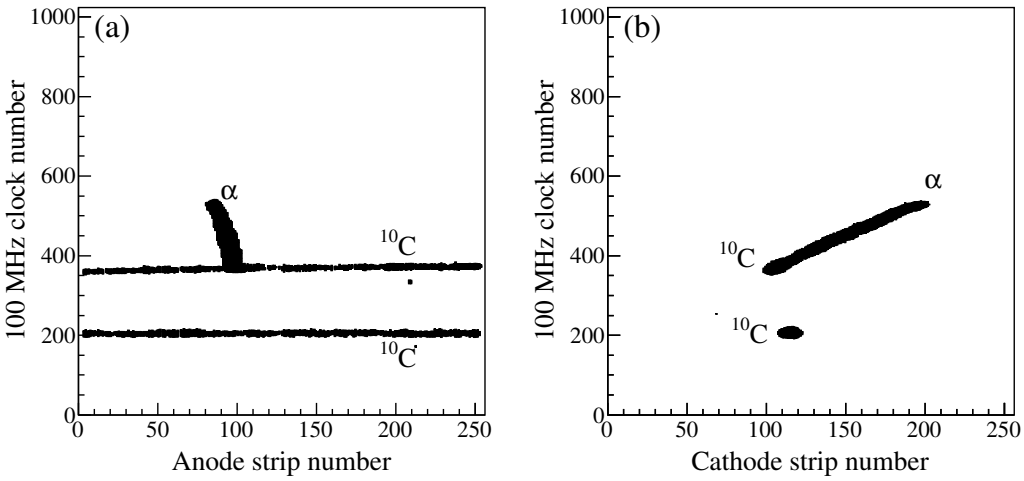

Figure 4.1: Example of acquired track images of the α+^{10}C event. (a) Anode image. (b) Cathode image.

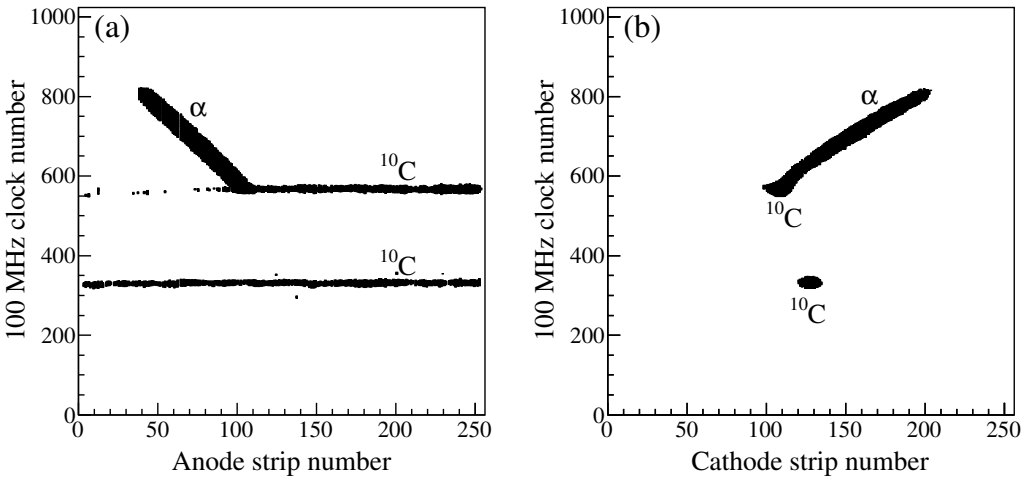

Figure 4.2: Same as Fig. 4.1, but track images of an inelastic scattering event exciting a highly excited state above the $2\alpha + 2p$ decay threshold at $E_x = 3.73$ MeV.

^{6}Be, they are unbound nuclei and eventually decay into protons and alpha particles

$$^{8}\mathrm{Be} \rightarrow 2\alpha \tag{4.1}$$
$$^{9}\mathrm{B} \rightarrow {}^{8}\mathrm{Be} + p \rightarrow 2\alpha + p \tag{4.2}$$
$$^{6}\mathrm{Be} \rightarrow \alpha + 2p. \tag{4.3}$$

Considering that dE/dx is proportional to Z^2/β^2, where Z is the charge of the particle and β is the velocity, the energy loss per unit length of the $2\alpha + 2p$ particles is about 1/3 of the incident ^{10}C. As a consequence, the observed horizontal trajectories in the anode image after the scattering point become thinner than before the scattering point as seen in Fig 4.2(a).

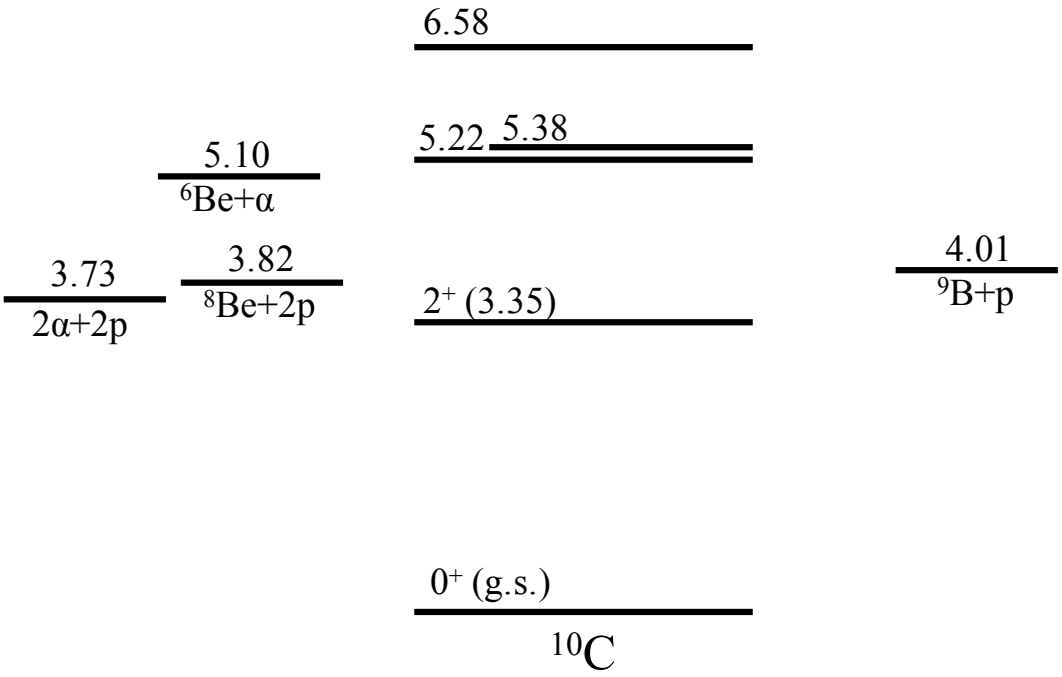

Figure 4.3: Known energy levels in ^{10}C taken from Ref. [113].

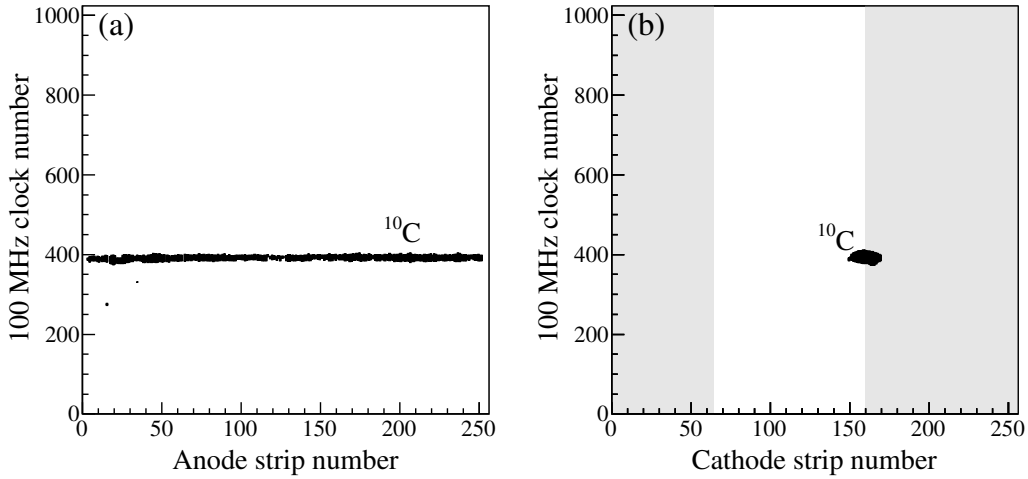

Figure 4.4: Example of background events in which the beam particle passed through the cathode trigger region. The gray areas show the trigger region.

4.1.2 Examples of background events

Not only the α+^{10}C scattering events, background events were also acquired in the present measurement. The background events were mainly caused by the ^{10}C beam particles that just passed through the cathode trigger region without a scattering in the sensitive volume of the TPC as shown in Fig. 4.4. The trigger region is indicated with the gray areas in the figure. Hereafter, we call these events "beam-particle events".

The background events were also caused by the quenching CO_2 gas. Figure 4.5 shows an example of the $^{10}C + CO_2$ scattering events. Because the mass of carbon and oxygen nuclei in the CO_2 gas is close to that of the incident ^{10}C, ^{10}C was scattered at a large angle. The trajectories of the scattered ^{10}C and the recoil carbon or oxygen after the scattering were recorded. Another example of the ^{10}C + CO_2 events is presented in Fig. 4.6. In this event, carbon or oxygen nucleus was highly excited above particle decay thresholds and decayed into lighter particles. Multiple trajectories due to the scattered ^{10}C and the decay products from carbon or oxygen are observed.

In case of the beam-particle events, no trajectory with a large angle is observed in the anode images. In case of the ^{10}C + CO_2 events, two or more trajectories with large angles from the beam axis are observed in the anode images.

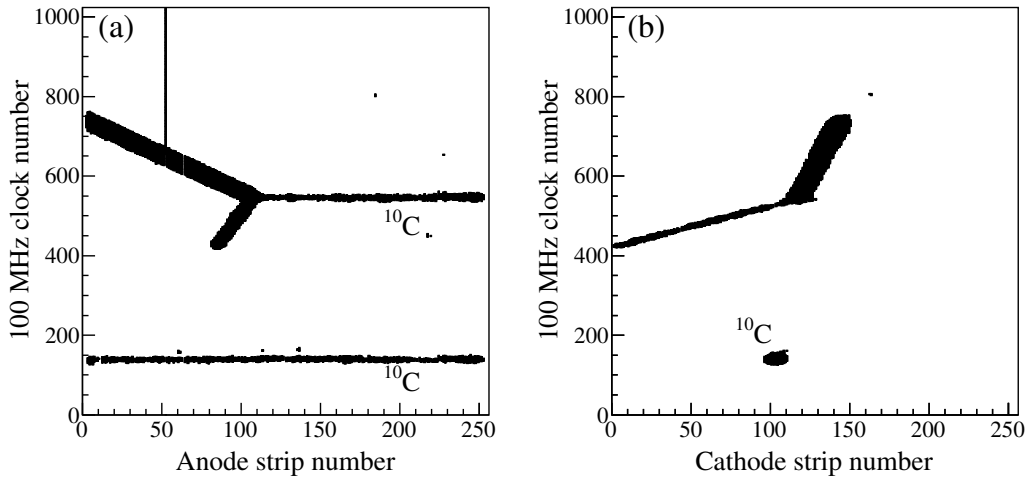

Figure 4.5: Example of the ^{10}C + CO_2 event. The incident ^{10}C particle was scattered from carbon or oxygen contained in the CO_2 gas. Both the scatted ^{10}C and recoiled carbon or oxygen trajectories are observed.

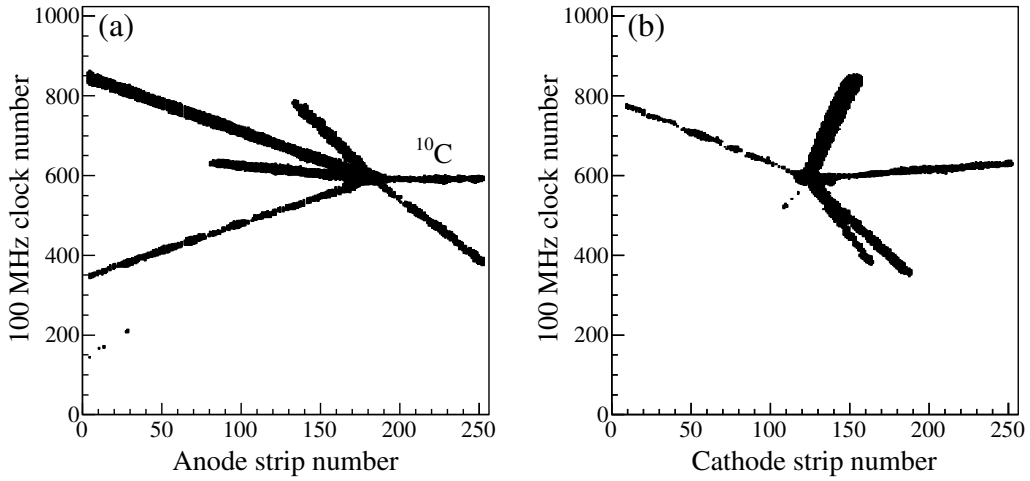

Figure 4.6: Another example of the ^{10}C + CO_2 event. The carbon or oxygen nucleus was excited above the particle decay thresholds and immediately decayed into lighter particles.

4.2 Examples of the FADC data for the α+^{10}C scattering events

The waveform information obtained by the FADCs is also useful for the analysis. Fig. 4.7 presents typical recorded waveforms in the α+^{10}C event shown in Fig. 4.1. The vertical axes represent the recorded pulse heights. The horizontal axes represent the 25-MHz clock numbers which are synchronized with the 100-MHz clock numbers used as the vertical axes in the anode and cathode images. While the polarity of the anode signals is positive, that of the cathode signals is negative. The baselines of the recorded waveforms should be subtracted in the analysis of the charge collected. The baseline values were assumed to be constant for each FADC channel.

The waveforms after the baseline subtraction are presented in Fig. 4.8. As seen in Ch. 7 of Fig. 4.8(a), the analog signals due to the incident ^{10}C particles are observed as sharp peaks. Because the trajectories of the recoil alpha particle has vertical component, the distribution of the electron drift time of the electrons spreads and the analog signals become wider than those due to the beam particles as seen in Ch. 2 and Ch. 3.

The integration of the pulses, which corresponds to dE/dx of the particles, would be helpful to distinguish the recoil alpha particles and the ^{10}C particles.

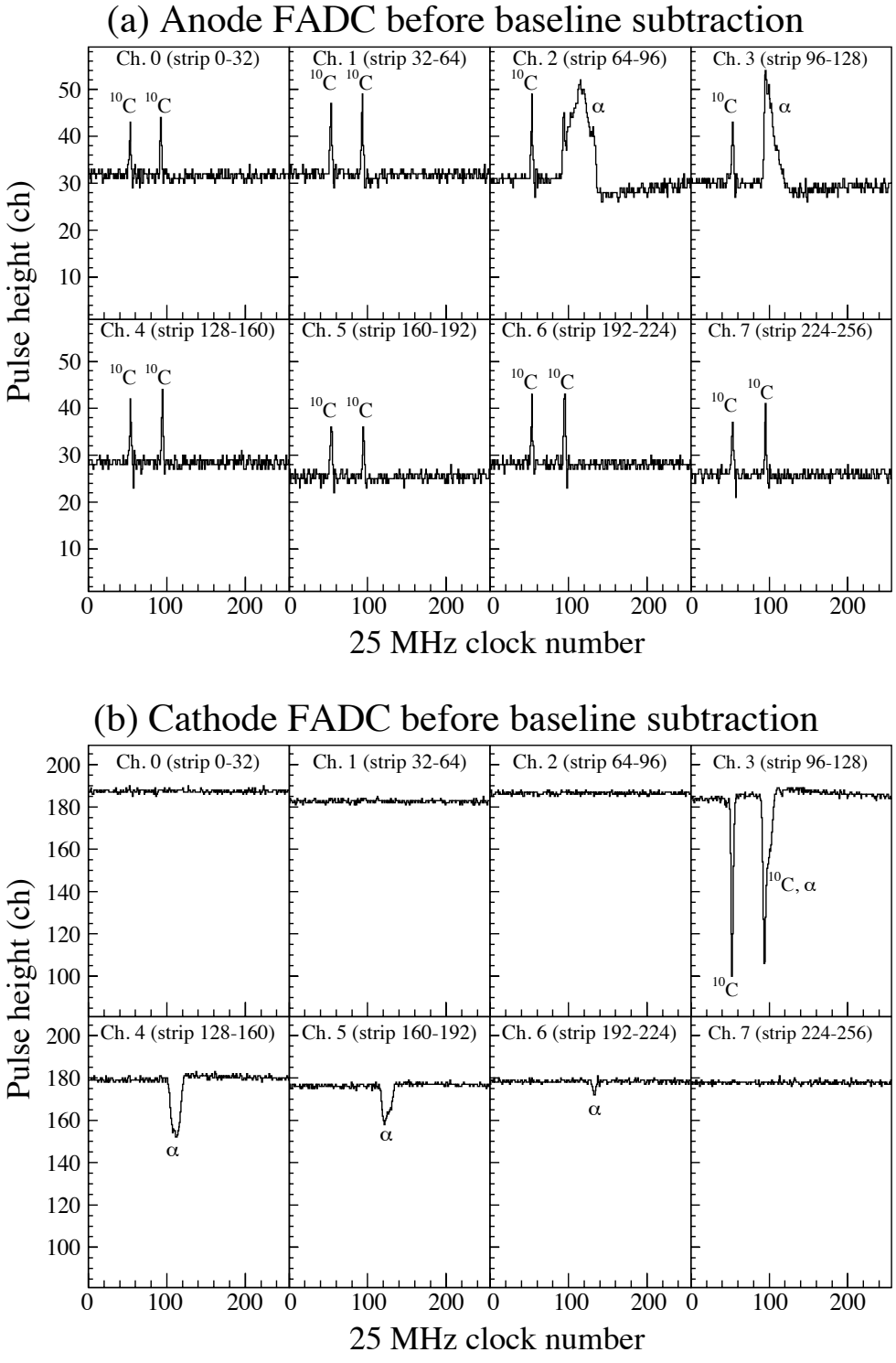

Figure 4.7: Waveforms acquired by the FADCs before the baseline subtraction in the event shown in Fig. 4.1. (a) Anode waveforms. (b) Cathode waveforms.

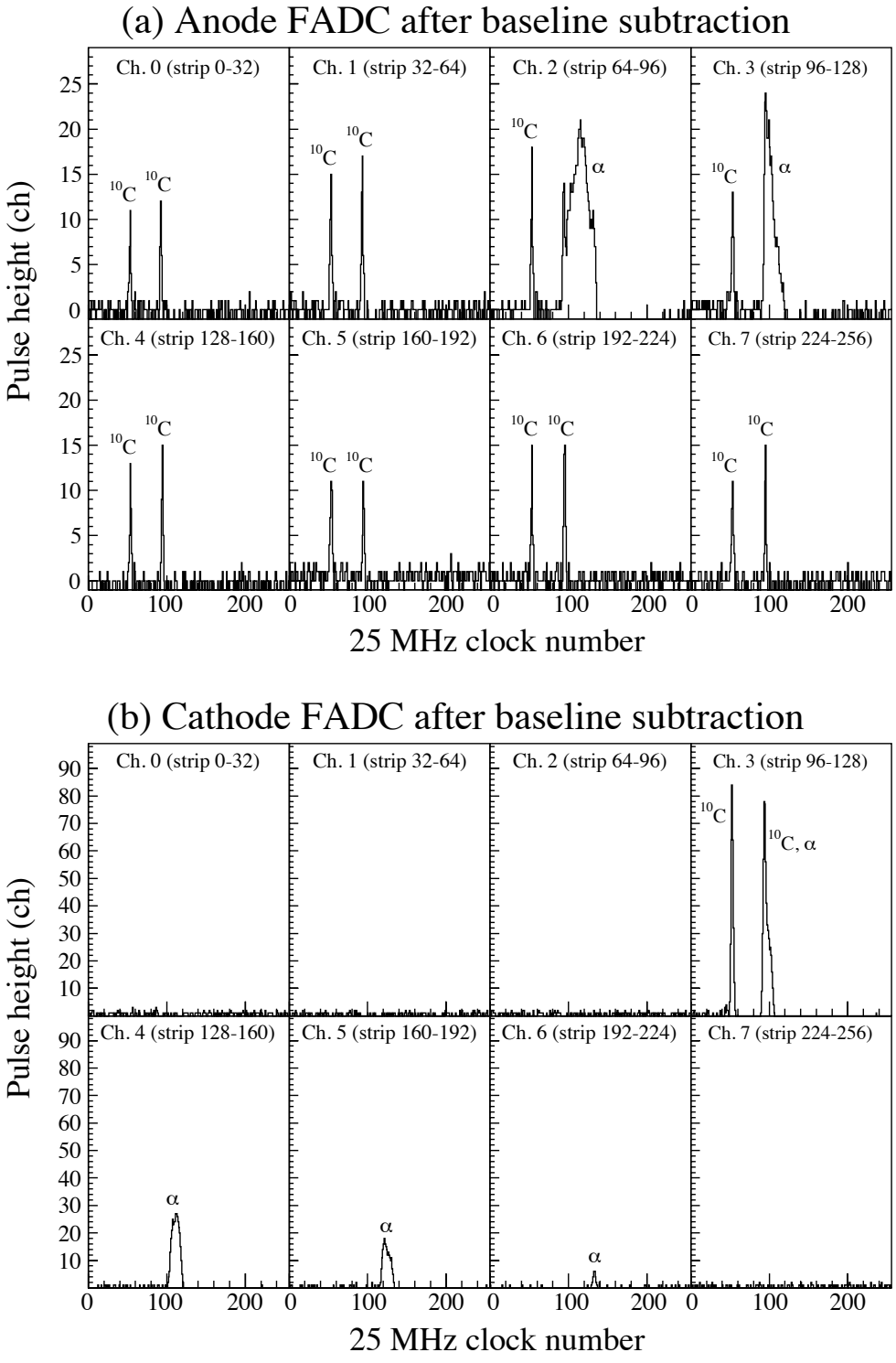

Figure 4.8: Same with Fig. 4.7, but after the baseline subtraction.

4.3 Procedure of the TPC data analysis

The α+^{10}C events exhibit the following two features. First, the energy loss per unit length of the recoil alpha particle at $E_\alpha \sim 0.5$ MeV is about 7 times larger than that of the incident ^{10}C beam at 68 MeV/u. Second, because of the large mass ratio between ^{10}C and alpha particle, ^{10}C hardly changes its angle in the scattering with alpha particles but alpha particles are recoiled at large angles from the beam axis. Therefore, just one tilted trajectory from the horizontal line due to the recoil alpha particle is observed in the anode image as seen in Figs 4.1(a) and 4.2(a). On the other hand, in a beam-particle event, no tilted trajectory is observed in the anode image as seen in Fig. 4.4(a). In a CO_2 + ^{10}C background event, multiple tilted trajectories are observed as seen in Figs 4.5(a) and 4.6(a). Considering the above two features, the analysis of the TPC data was carried out with the following procedures. As an example, we present the data analysis of the event shown in Figs. 4.1 and 4.8.

i) Count the number of pulses in the baseline subtracted FADC data, and integrate each pulse over time to obtain the energy loss of the particle. The threshold for the pulse height was determined to be 2. Figure 4.9 shows a typical pulse shape of the anode analog signal from Ch. 2 [see Fig. 4.8(a)] after the baseline subtraction for the FADC data. The threshold level is indicated by the black dashed line. In this example, two pulses (Pulse 1 and Pulse 2) were extracted which are indicated by the blue and green regions in Fig. 4.9.

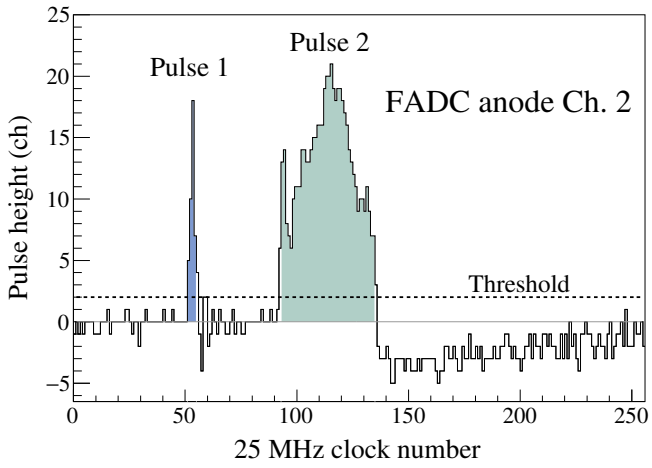

Figure 4.9: Typical pulse shape of the anode analog signal from Ch. 2 [see Fig. 4.8(a)] after the baseline subtraction for the FADC data. The extracted two pulses are indicated by the blue and green regions.

ii) If the integrated values of the FADC pulses were lower than a certain threshold ($p_{\rm pulse}$), the corresponding pixels in the anode and cathode images were eliminated from the

analysis. This procedure was necessary to exclude hit pixels due to the ^{10}C beam particles and to facilitate the extraction of the recoil alpha particle trajectories. Since the energy loss of the ^{10}C beam is much smaller than those of the recoil alpha particles, the pixels due to the ^{10}C beam were selectively eliminated using the FADC integral information. The threshold value was determined to 80 as described in Sec. 4.4. Figure 4.10 shows the same anode image of Fig. 4.1(a) but the pixels which correspond to the analog signals of Pulse 1 and Pulse 2 in Fig. 4.9 are indicated by the blue and green pixels, respectively. In this example, the integration of Pulse 1 was lower than the threshold value but the integration of Pulse 2 was higher than the threshold. Therefore, only the green pixels in Fig. 4.10 remained after the pixel elimination for FADC Ch. 2. The images after the pixel elimination are shown in Figs. 4.11(a) and (b).

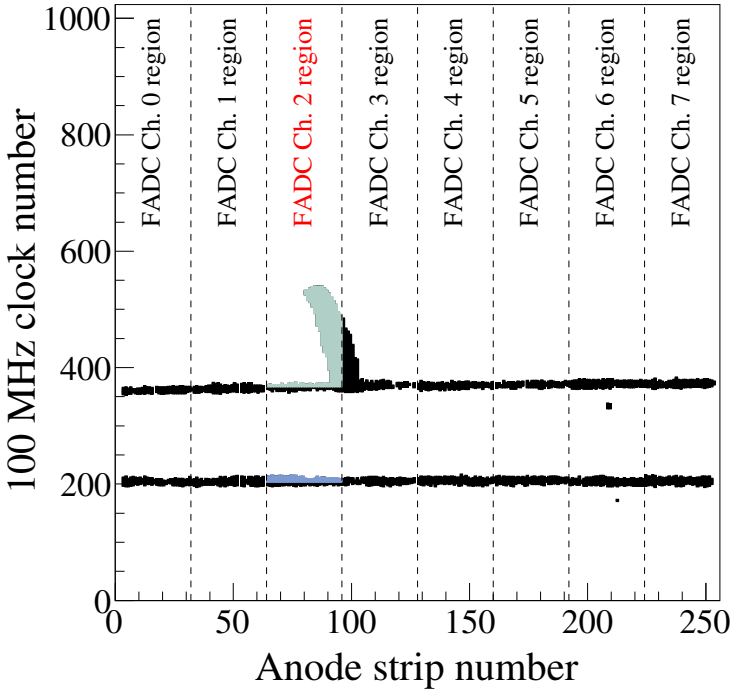

Figure 4.10: Same with Fig. 4.1(a) but the pixels which correspond to the analog signals of Pulse 1 and Pulse 2 in Fig. 4.9 are indicated by the blue and green pixels, respectively.

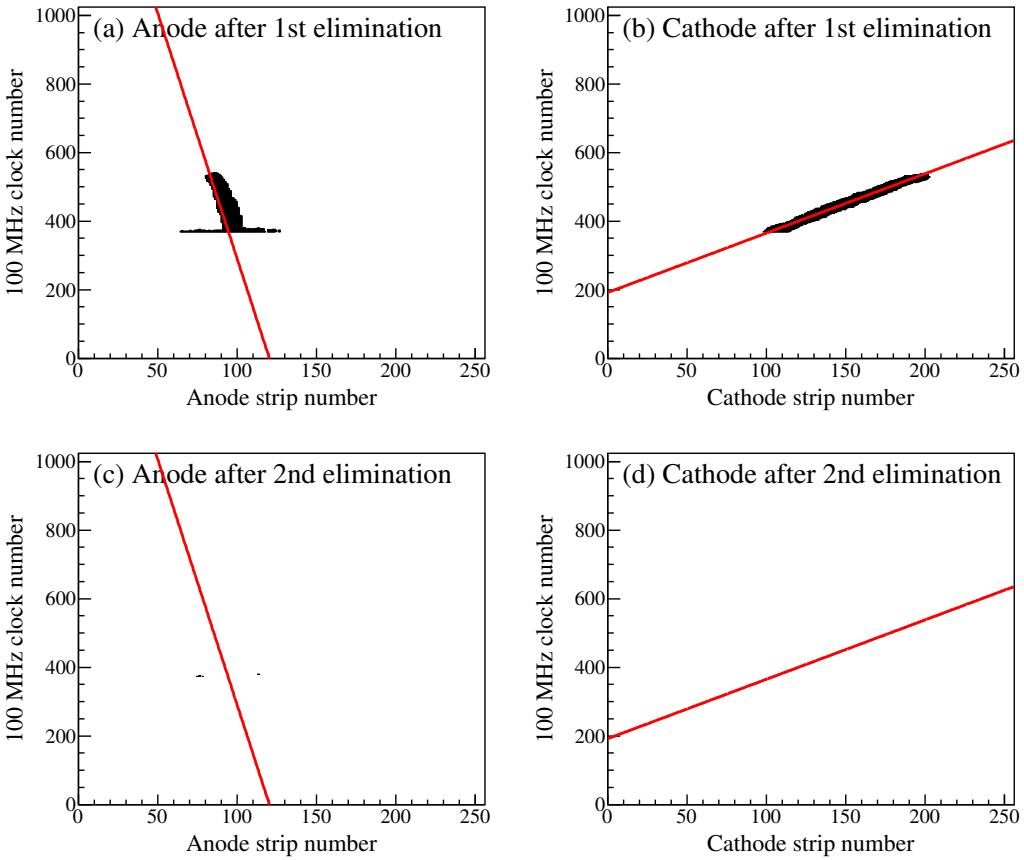

Figure 4.11: (a) and (b) Anode and cathode images after eliminating the pixels using the FADC integral information [see the procedure ii)]. (c) and (d) Anode and cathode images after eliminating the pixels near the straight lines extracted by the Hough transformation [see the procedure v)]. The straight lines extracted by the Hough transformation are plotted by the red solid lines.

iii) Transform the anode and cathode images after the pixel elimination to the anode and cathode Hough histograms, according to the Hough transformation which is explained in detail in Appendix A. The Hough histograms transformed from the anode and cathode images in Figs. 4.11(a) and (b) are shown in Figs. 4.12(a) and (b), respectively.

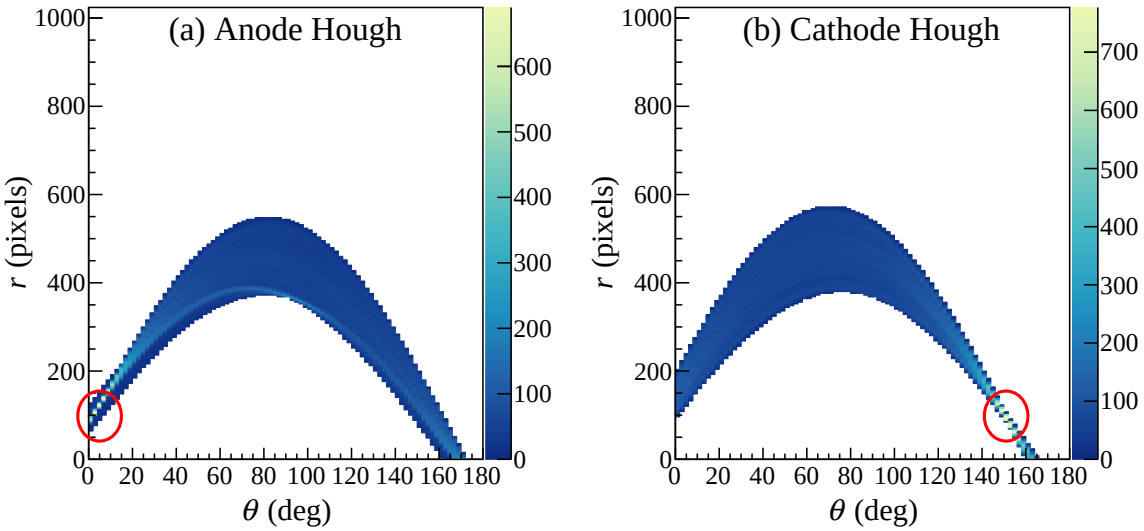

Figure 4.12: Two-dimensional histograms in the Hough spaces obtained from Figs 4.11(a) and (b). The red circles show the positions of the bins with the maximum entries in the Hough histograms.

iv) After the Hough transformation, find the bins of the maximum entries in the Hough histograms. The bins of the maximum entries are indicated by the red circles in Fig. 4.12. From the coordinates of the maximum bins, one straight line is extracted from the anode and cathode images. The extracted straight lines are drawn by the red solid lines in Figs. 4.11(a) and (b).

v) Eliminate the pixels near the straight lines determined in the previous procedure from the anode and cathode images in Figs. 4.11(a) and (b). The anode and cathode images after the elimination are shown in Figs. 4.11(c) and (d), respectively. In this event, all pixels were eliminated except for the small spots around $(80, 400)$ in the anode image.

vi) Transform the remaining pixels again into the Hough spaces.

vii) Repeat iv), v), and vi) until the maximum bin counts in the anode and cathode Hough histograms become smaller than thresholds. The threshold values are denoted as C_{anode} and C_{cathode} for the anode and cathode Hough histograms, respectively, and they are optimized in Sec. 4.4. In this event, the Hough transformation was carried out only once.

viii) Count the number of straight lines in the anode image whose angle from the horizontal axis is larger than a certain threshold value θ_{tilt} (tilted line). In Fig. 4.11(a), this

number was one. The optimization procedures of $\theta_{\rm tilt}$ values are described in Sec. 4.4.

ix) Count the number of extracted straight lines in the cathode image. In Fig. 4.11(b), this number was one.

x) If the number of the tilted lines in the anode image and the number of the straight lines in the cathode image were both one, the event was regarded as a candidate of the α+^{10}C scattering event and the extracted lines were regarded as the trajectory of the recoil alpha particle. If the number of the tilted lines in the anode image was zero, the event was classified as a beam-particle event. If the number of the tilted line was more than one, the event was classified as a ^{10}C + CO_2 event.

xi) For a candidate of the α+^{10}C scattering event, find edge hit-pixels along the extracted straight lines by the Hough transformation. In the anode image, the edge points were searched by the following procedure. At every clock number, calculate the anode strip number on the extracted line according to the equation of the line. If the calculated point is a black pixel, search the left and right edges of the trajectory at the same clock number, and calculate the middle point between the left and right edges. In a cathode image, the edge points were extracted by the similar procedure to the anode ones, but the up and down edges at every strip were searched, and the middle point between the two edges was calculated. The extracted edge points are shown in Fig 4.13. In the anode image (a), the left and right edges and the middle points are plotted by the green, blue, and red solid circles, respectively. In the cathode image (b), the up and down edges and the middle points are plotted by the green, blue, and red solid circles, respectively.

xii) Fit straight lines to the extracted middle points in the anode and cathode images, respectively, to determine the angle of the recoil alpha particle with better precision because the angular resolution was limited by the bin size of the Hough histogram. The extracted middle points tend to deviate from the straight line near the track stop point because charged particles significantly deflects just before they stop. Therefore, the second fitting was performed for the anode image after excluding the points which were more than 3 pixels away from the first fitted line. In the cathode image, the second fitting was not necessary because the number of the extracted middle points was much larger than that in the anode image, and the fitting was not affected by the points near the stop point. The straight lines determined by the first fit are plotted by the red solid lines in Figs. 4.13(a) and (b), and the other line determined by the second fit is plotted by the blue dashed line in Fig. 4.13(a).

xiii) Find the edge pixels in the anode and cathode images along the fitted lines. These points are the scattering point and track stop point of the recoil alpha particle. They are plotted by the cyan solid circles in Fig. 4.13.

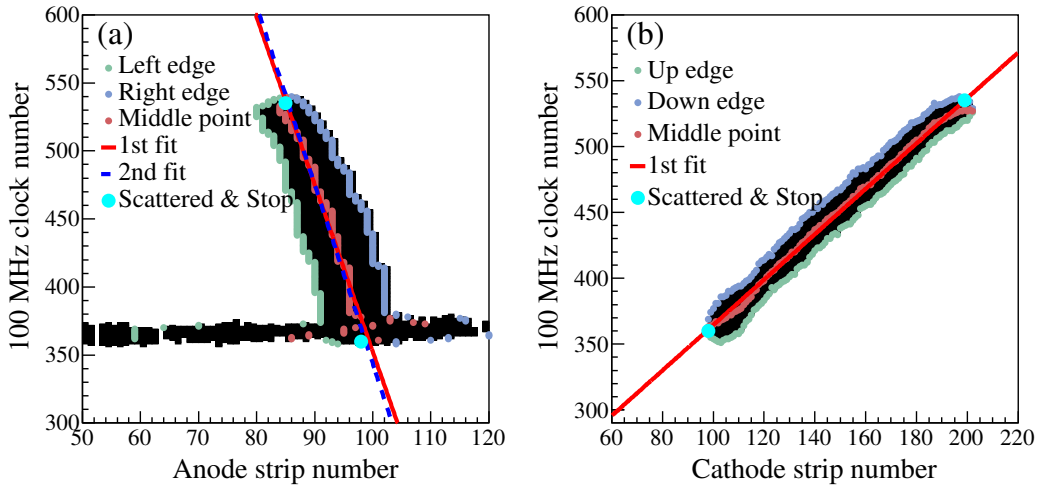

Figure 4.13: (a) Zoomed anode image for the event shown in Fig. 4.1. The extracted left and right edges and the middle points are plotted by the green, blue, and red solid circles. The lines determined by the first and second fit are plotted by the red solid and blue dashed lines, respectively. The scattered and track stop points are plotted by the cyan solid circles. (b) Zoomed cathode image for the event shown in Fig. 4.1. The line determined by the first fit is plotted by the red solid line. The extracted up and down edges and the middle points are plotted by the green, blue, and red solid circles.

xiv) From the straight lines in the anode and cathode images, the polar angle in the laboratory frame ($\theta_{\text{lab.}}$) and the azimuthal angle (ϕ) of the recoil alpha particle were calculated assuming the beam axis was parallel to the cathode strips of the μ-PIC as

$$\theta_{\text{lab.}} = \arccos\left(\frac{|\Delta z|}{\Delta r}\right), \tag{4.4}$$

$$\phi = \arctan\left(\frac{\Delta y}{\Delta x}\right), \tag{4.5}$$

where

$$\Delta x = \frac{\Delta y}{\tan\theta'_c}, \tag{4.6}$$

$$\Delta y = 1, \tag{4.7}$$

$$\Delta z = -\frac{\Delta y}{\tan\theta'_a}, \tag{4.8}$$

$$\tan\theta'_a = \frac{v\tan\theta_a}{0.40}, \tag{4.9}$$

$$\tan\theta'_c = \frac{v\tan\theta_c}{0.40}. \tag{4.10}$$

Here, $\tan\theta_a$ and $\tan\theta_c$ are the slope parameters of the fitted lines in the anode and cathode images, and v is the measured electron drift velocity.

xv) Calculate the range of the recoil alpha particle in the TPC gas from the distance between the scattered and stop points.

xvi) Integrate the analog signals from the cathode FADCs to calculate the induced charges. The integration was performed between the scattered and stop points to avoid the contributions from the accidental-coincidence beam particles.

We selected the α+^{10}C events in which the scattered point locates between the 33–224th strip in the anode image. Thus, the effective thickness of the He target gas was 76.8 mm.

4.4 Optimization of analysis parameters

In the analysis procedures described in the previous section, the values of the following parameters must be determined:

- The threshold value p_{pulse} for the integrals of the FADC pulse in the procedure ii).
- The threshold values C_{anode} and C_{cathode} for the number of the maximum entry in the Hough histograms described in the procedure vii).
- The angular threshold θ_{tilt} for the "tilted line" in the anode image described in the procedure viii).

In order to optimize the above four parameters, we sampled 2,000 events from the acquired data and labeled these events as α+^{10}C scattering or background by eyes. Before the sampling, the main background events "beam-particle events" were roughly excluded from the analysis by selecting the events in which at least one FADC pulse integral higher than 150 was recorded in the anode data. The sampled 2,000 events were composed of the 889 α+^{10}C scattering events and the 1,111 background events. Assuming certain values of the four parameters, the 2,000 events were classified into the α+^{10}C scattering or the background. The goodness of the parameters was evaluated comparing the classification of the 2,000 events with the answers labeled by eyes.

The result of the comparison was classified into four types which are known as *confusion matrix* shown in Fig. 4.14. True positive (TP) means that the model correctly predicted the α+^{10}C event (positive) as an α+^{10}C event. False positive (FP) means that the model mis-predicted the α+^{10}C event as a background event (negative). False negative (FN) means that the model mis-predicted the background event as an α+^{10}C event. True negative (TN) means that the analyzer correctly predicts the background event as a background event.

In order to estimate the goodness of the parameters, we used the Jaccard coefficient which is defined as

$$J = \frac{N_{\mathrm{TP}}}{N_{\mathrm{TP}} + N_{\mathrm{FP}} + N_{\mathrm{FN}}}, \tag{4.11}$$

where N_{TP}, N_{FP}, and N_{FN} are the numbers of the TP, FP, and FN events in the analysis of the 2,000 events. The Jaccard coefficient falls into the range $0 \leq J \leq 1$. This value decreases

		Actual	
		Positive	Negative
Prediction	Positive	True Positive (TP)	False Positive (FP)
	Negative	False Negative (FN)	True Negative (TN)

Figure 4.14: Confusion matrix.

Table 4.1: Optimized parameters in the present analysis tabulated with the Jaccard coefficient, the signal efficiency, and the background rejection ratio when these optimized parameters were used.

Parameter	Value
p_{pulse}	80
C_{anode}	160
C_{cathode}	200
θ_{tilt}	12 deg
Jaccard	0.79
Signal efficiency	0.93
Background rejection	0.86

when the model mis-predict the events and increases when the model correctly extract the α+^{10}C events.

The four parameters were optimized by a mesh-search method to maximize the Jaccard coefficient. Figure 4.15 shows correlations of the Jaccard coefficient versus the four parameters. The optimized parameters and their Jaccard coefficients are listed in Table 4.1. The signal efficiency and background rejection ratio, defined as

$$\text{Signal efficiency} = \frac{N_{\mathrm{TP}}}{N_{\mathrm{TP}} + N_{\mathrm{FP}}}, \tag{4.12}$$

$$\text{Background rejection} = \frac{N_{\mathrm{TN}}}{N_{\mathrm{TN}} + N_{\mathrm{FN}}} \tag{4.13}$$

are also listed in the table. Here, we note that the achieved background rejection ratio is not high compared to the signal efficiency. However, this ratio was improved to 0.99 after applying the PID to select only the $Z = 2$ recoil particles as described in Sec. 4.5.

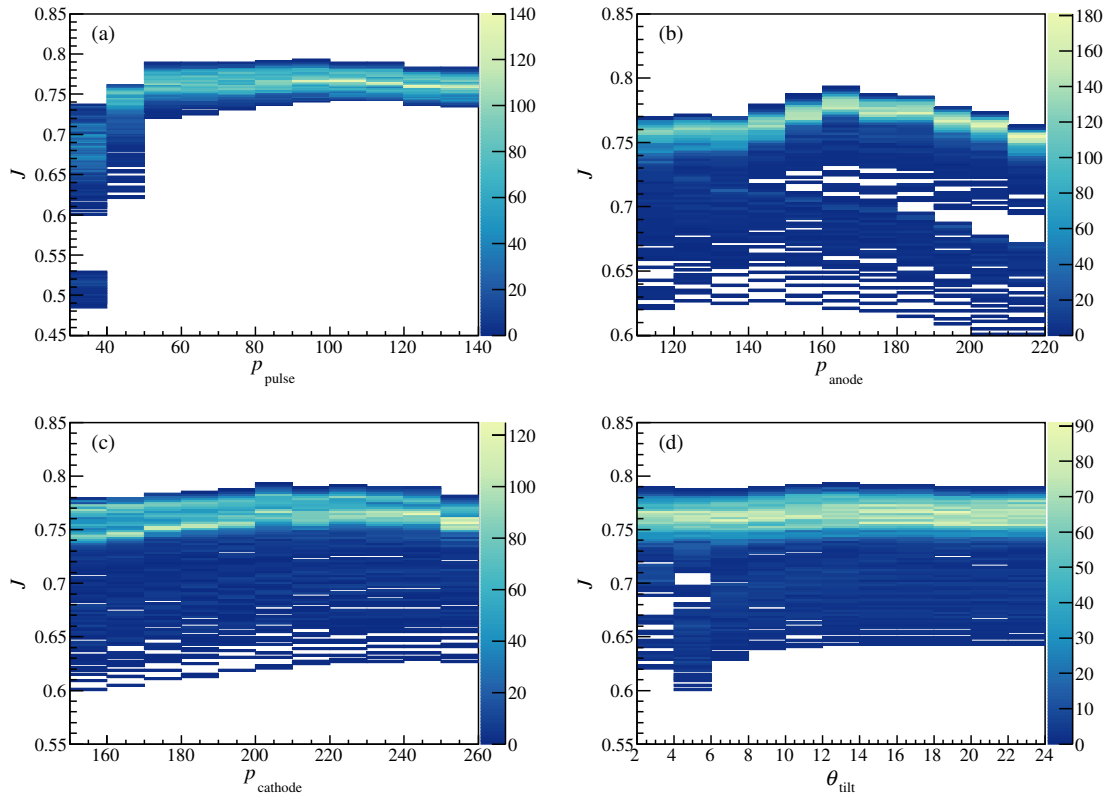

Figure 4.15: Correlations of the Jaccard coefficient versus (a) p_{pulse}, (b) p_{anode}, (c) p_{cathode}, and (d) θ_{tilt}.

4.5 Particle identification of the recoil particles

As seen in Table 4.1, the present analysis with the optimized parameters cannot reject all of the background events. Further background rejection was done by the recoil PID.

The range of charged particles in the TPC gas is proportional to $E^2/(AZ^2)$, and the total charge collected by the μ-PIC is proportional to the kinetic energy of the charged particles if the charged particles stop inside the sensitive volume of the TPC. Figure 4.16 shows the correlations between the total charge collected by the μ-PIC and the range of the recoil particle in the measurements with the ^{10}C beam. In these figures, only the the events in which the stop point locates inside the TPC sensitive volume are presented. Figure 4.16(a) is the correlation in the measurement at a gas pressure of 500 hPa, while Fig. 4.16(b) is at 1000 hPa. In both of the plots, the loci due to the $Z = 2$ particles are clearly separated from those due to $Z = 1$ and $Z > 2$ particles. The $Z = 1$ and $Z > 2$ particles are the decay products of the carbon or oxygen nuclei in the CO_2 quenching gas. We selected the $Z = 2$ events enclosed by the red solid lines in the figures. For the reliable track reconstruction, we set the minimum range for the recoil alpha particles at 25 mm.

If the recoil particles escaped from the sensitive volume of the TPC and hit one of the

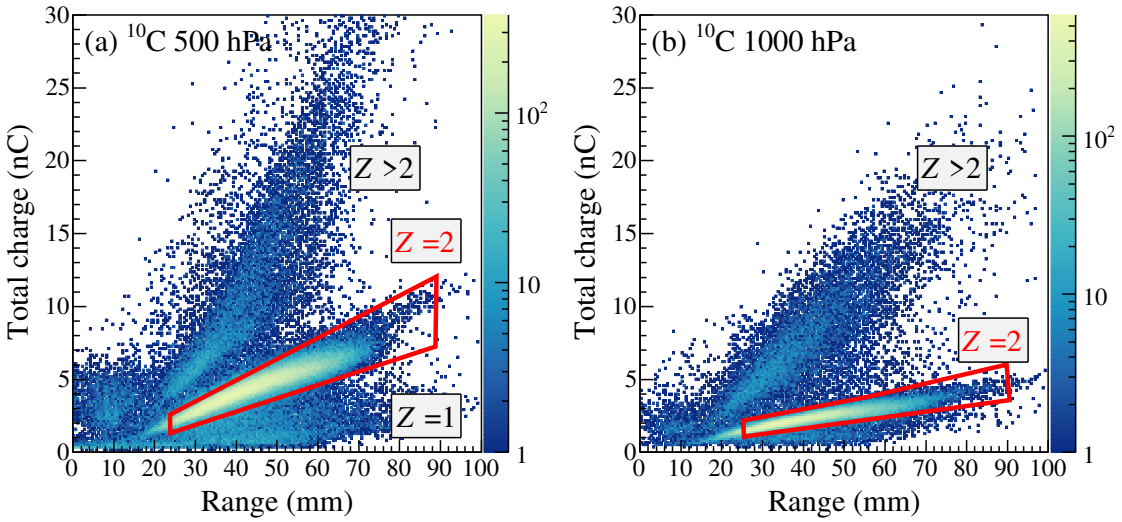

Figure 4.16: Scatter plot of the total charge measured by μ-PIC and the range of the recoil particle. The labels of "$Z = 1$", "$Z = 2$", and "$Z = 3$" are drawn near the loci due to the $Z = 1$, $Z = 2$, and $Z = 3$ particles, respectively. (a) PID plot for the measurement with the ^{10}C beam and at a gas pressure of 500 hPa. (b) PID plot for the measurement with the ^{10}C beam and at 1000 hPa.

Si detectors, PID can be performed by the correlation between the energy measured by the Si detector and the charge collected by the μ-PIC as shown in Fig. 4.17. The horizontal axis represents the charge obtained by integrating the analog pulse from Ch.7 of the cathode FADC and the vertical axis represents the energy measured by the left down side Si detector. The loci due to the $Z = 2$ particles are clearly separated from the $Z = 1$ loci. The $Z = 2$ particles were selected by gating events which locate in the regions enclosed by the red solid lines.

4.6 Reconstruction of kinematics

If the recoil alpha particle stopped inside the TPC sensitive volume, the recoil energy was determined from the range in the gas using the computer program SRIM [144]. The calculated recoil energies as a function of range in the TPC gas are plotted in Fig. 4.18. The red solid line and blue dashed lines represent the recoil energies when the gas pressure is at 500 and 1000 hPa, respectively.

When the recoil alpha particle hit one of the Si detectors, the recoil alpha energy E_α was calculated by integrating the energy loss in the TPC gas from the the position where the recoil alpha particle hit the Si detector ($\boldsymbol{r}_{\mathrm{Si}}$) to the scattered point ($\boldsymbol{r}_{\mathrm{s}}$) as

$$E_\alpha = E_{\mathrm{Si}} + \int_{\boldsymbol{r}_{\mathrm{Si}}}^{\boldsymbol{r}_{\mathrm{s}}} \left.\frac{dE}{dx}\right|_{E=E(\boldsymbol{r})} d\boldsymbol{r}, \tag{4.14}$$

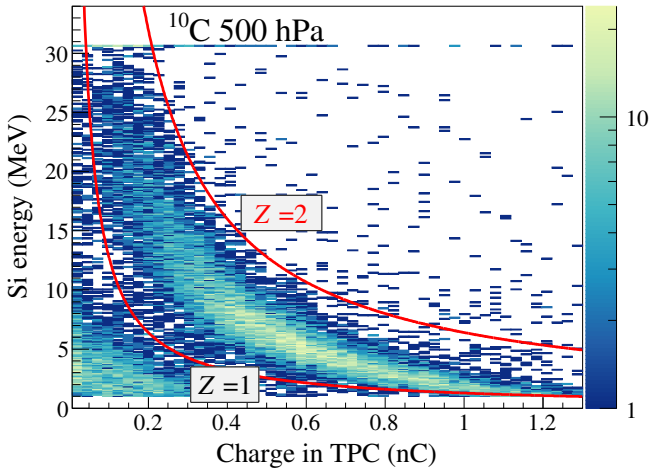

Figure 4.17: Correlation between the energy measured with the left down Si detector and the charge obtained by integrating the analog pulse from Ch. 7 from the cathode. The gas pressure was at 500 hPa.

where E_{Si} is the energy measured by the Si detector. The energy loss in the TPC gas as a function of the energy of the alpha particle was calculated by the SRIM code. The calculated dE/dx values as a function of energy of the alpha particle are shown in Fig. 4.19.

The two dimensional scatter plot of the measured kinetic energy versus recoil angle in the α+^{10}C events is shown in Fig. 4.20(a). The red and blue dots represent the events in which the recoil alpha particles stopped inside the TPC sensitive volume in the measurements at 500 and 1000 hPa (denoted as "500 hPa events" and "1000 hPa events"), respectively. The green dots represent the events in which the recoil alpha particles hit one of the Si detectors in the measurement at 500 hPa (denoted as "Si events"). The kinematic correlation between energies and angles of the recoil alpha particles at different excitation energies (E_x) in ^{10}C are shown by the black solid lines and the c.m. angles ($\theta_{\mathrm{c.m.}}$) are plotted by the black solid circles.

Owing to the active target technique, the detection threshold for the recoil alpha particles was successfully lowered down to 0.5 MeV. This detection threshold of the recoil energy is determined by the minimum range of 25 mm in the PID procedure (See Sec. 4.5).

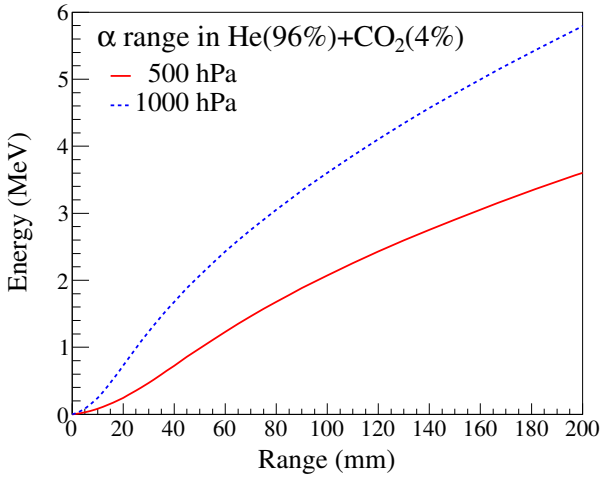

Figure 4.18: Energies of alpha particles as a function of range in the He(96%)+CO_2(4%) mixture gas calculated by SRIM [144]. The red solid line and blue dashed lines represent the recoil energies when the gas pressure is at 500 and 1000 hPa, respectively.

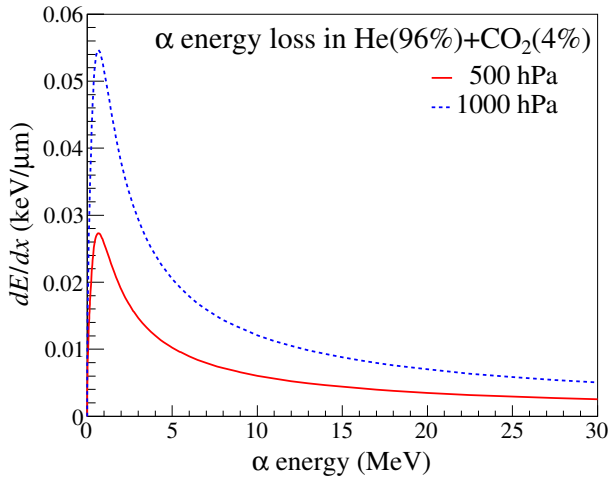

Figure 4.19: dE/dx values of the alpha particle through the TPC gas as a function of energy of the alpha particle calculated by the SRIM code [144]. The red solid line and blue dashed lines were calculated at a gas pressure of 500 and 1000 hPa, respectively.

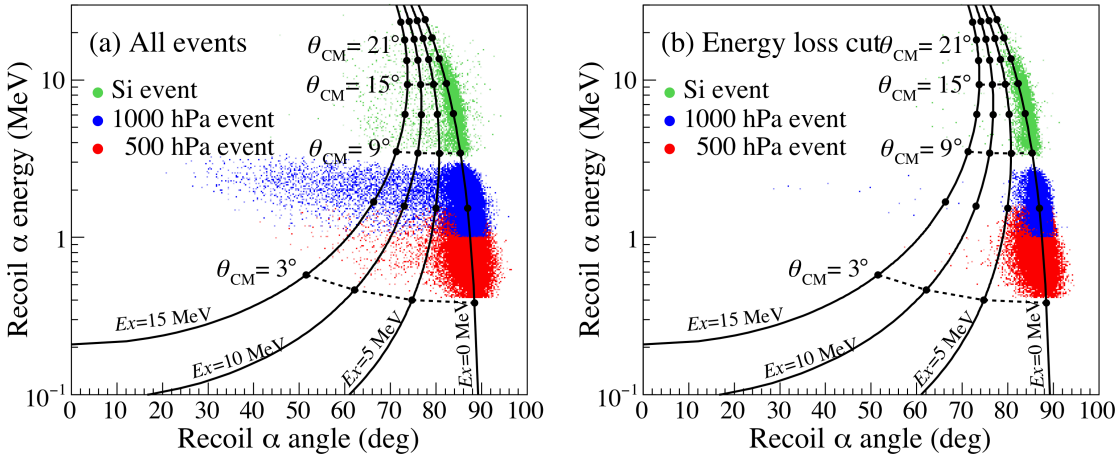

Figure 4.20: Two dimensional scatter plot of kinetic energy versus angle of the recoil alpha particles. The red, blue, and green dots represent the "500 hPa events", "1000 hPa events", and "Si events", respectively. The kinematic correlation between energies and angles of the recoil alpha particles at different excitation energies in ^{10}C are shown by the black solid lines and the c.m. angles are plotted by the black solid circles. (a) All of the α+^{10}C scattering events. (b) The elastic and inelastic scattering events to low excited states selected by the energy-loss cut condition (see Sec. 4.7).

4.7 Excitation-energy spectra

The excitation energy E_x of ^{10}C and $\theta_{\mathrm{c.m.}}$ were calculated from the measured angle and energy of the recoil alpha particle and the central energy of the ^{10}C beam (68 MeV/u) using the missing-mass formulae described in Appendix B. Fig. 4.21 shows the excitation-energy spectrum obtained from the measurement when the gas pressure was at 1000 hPa. A prominent peak due to the elastic scattering was observed at $E_x = 0$ MeV as well as small contribution from inelastic scatterings.

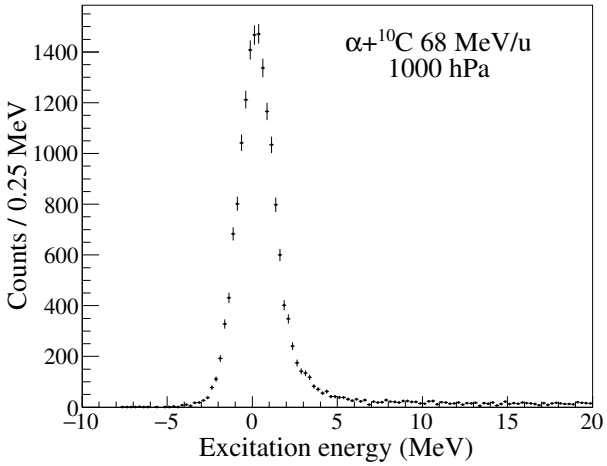

Figure 4.21: Excitation-energy spectrum of the α+^{10}C scattering at 68 MeV/u. The spectrum was obtained from the measurement when the gas pressure was at 1000 hPa.

In the present work, we focus on the analysis of the elastic scattering and the inelastic scattering to the 2^+_1 state at $E_x = 3.35$ MeV to deduce the neutron transition matrix element from the ground state to the 2^+_1 state. Therefore, contributions from the highly excited states above the particle decay threshold at $E_x = 3.37$ MeV, which may overlap onto the 2^+_1 region, should be excluded. As discussed in Sec. 4.1.1, the elastic scattering and the inelastic scattering exciting the 2^+_1 state can be distinguished from the inelastic scattering exciting the highly excited states at $E_x > 3.73$ MeV by using the information on the energy loss obtained from the anode FADCs. Since both the incident and scattered particles are ^{10}C in the elastic scattering and the inelastic scattering exciting the 2^+_1 state, the energy losses of these particles per unit length in the TPC gas are almost same. On the other hand, highly excited states above the threshold immediately decay to $2\alpha + 2p$ particles. Since the energy loss of the $2\alpha + 2p$ particles is about 1/3 of the incident ^{10}C, the energy loss after the scattering point become smaller than before the scattering point when $E_x > 3.73$ MeV. Figure 4.22 shows the correlation between the pulse heights of the analog signals from the most downstream channel (Ch. 0) and the most upstream channel (Ch. 7) in the anode. Figures 4.22(a) and (b) are the correlations at 500 hPa and 1000 hPa,

respectively. We selected the low-excitation events at $E_x < 3.73$ MeV by gating the region enclosed by the red solid lines. On the other hand, the high-excitation events at $E_x > 3.73$ MeV were selected by gating the region enclosed by the cyan dashed lines. Figure 4.20(a) is the scatter plot before applying the gate and Figure 4.20(b) is that after applying the gate to select the low-excitation events. With the above gate condition, only low-lying states below the particle decay threshold were successfully selected. The excitation-energy spectra of the low-excitation events at different $\theta_{\mathrm{c.m.}}$ and the high-excitation events are shown in Figs. 4.23 and 4.24, respectively.

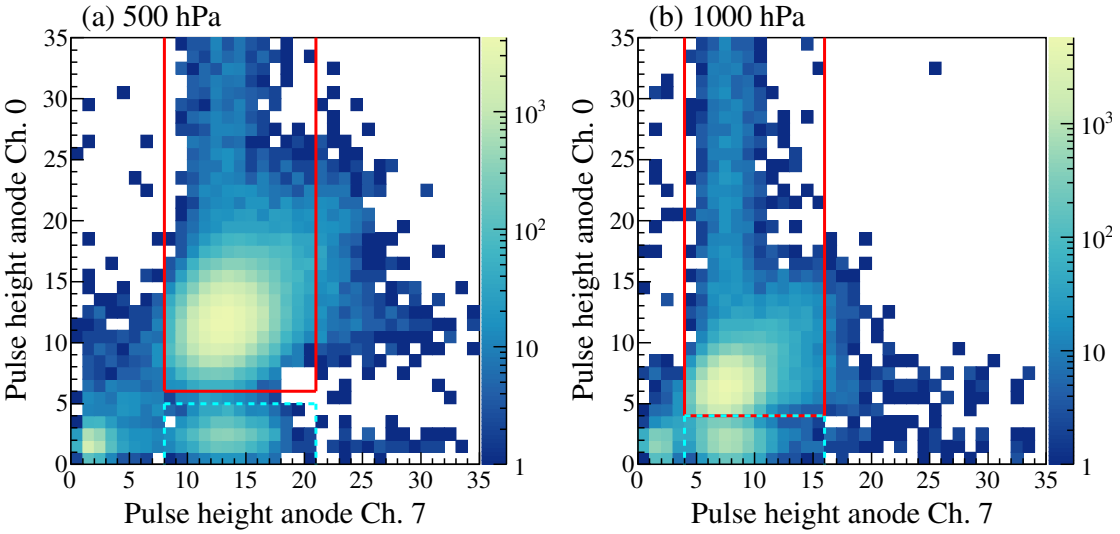

Figure 4.22: Correlation between the pulse heights of the analog signals from the most downstream (vertical axis) and the most upstream (horizontal axis) channels in anode. (a) Measurement at 500 hPa with ^{10}C beam. (b) Measurement at 1000 hPa with ^{10}C beam.

The excitation-energy spectra at $4.0° < \theta_{\mathrm{c.m.}} < 5.0°$ and $5.8° < \theta_{\mathrm{c.m.}} < 7.2°$ in Fig. 4.23 were obtained by selecting the low-energy recoil alpha particles, which stopped inside the sensitive volume of the TPC, when the gas pressure was 500 and 1000 hPa ("500 hPa events" and "1000 hPa events"). The excitation-energy spectra at $9.0° < \theta_{\mathrm{c.m.}} < 16.0°$ were obtained by selecting the high-energy recoil alpha particles, which were detected by one of the Si detectors, when the gas pressure was 500 hPa ("Si events").

The prominent peaks due to the ground state are observed with a small contributions from the 2^+_1 state at $E_x = 3.35$ MeV. The excitation-energy resolution for the ground state is 0.9 MeV in sigma at $4.0° < \theta_{\mathrm{c.m.}} < 4.5°$. The resolution becomes worse to 2.0 MeV at $14.0° < \theta_{\mathrm{c.m.}} < 16.0°$. This is because the kinematic condition depends on the c.m. angles. As seen from Fig. 4.20, the distances between the black solid lines at different excitation energies are smaller at backward c.m. angles, and thus the excitation-energy resolution becomes worse. The kinematic curves are almost vertical at $3° < \theta_{\mathrm{c.m.}} < 20°$. This means that the excitation-energy resolution is determined mainly from the angular resolution for the recoil alpha particle.

By fitting two Gaussians to each spectrum, the yields of the ground and 2_1^+ states at each c.m. angle were obtained. The distances between the centers of the Gaussians were fixed at 3.35 MeV. In Fig. 4.23, the Gaussians for the ground and 2_1^+ states are plotted by the blue dashed and the green dotted lines, respectively. The sum of the two Gaussians are plotted by the red solid lines. The values of the reduced chi square (χ^2/ndf) of the fitting are given in each histogram. The yields for the 2_1^+ state at $4.0^\circ < \theta_{\mathrm{c.m.}} < 5.0^\circ$ were not reliably determined because cross sections for the 2_1^+ state are very small compared to those for the ground state. Therefore, the yields of the 2_1^+ state were deduced at $\theta_{\mathrm{c.m.}} > 5.8^\circ$ only, and the yields of the ground state at $4.0^\circ < \theta_{\mathrm{c.m.}} < 5.0^\circ$ were obtained neglecting the tiny contributions from the 2_1^+ state.

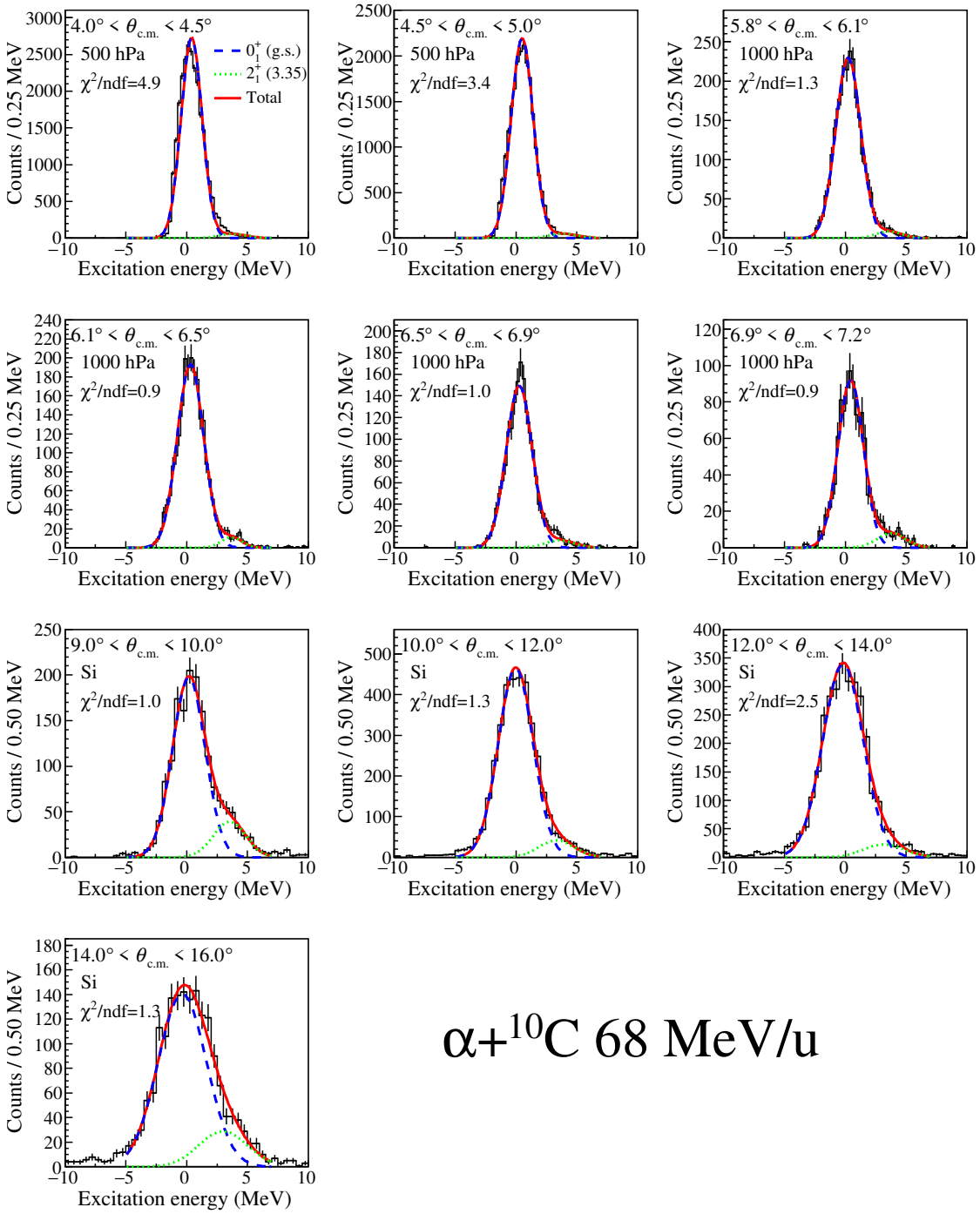

Figure 4.23: Excitation-energy spectra of the low-excitation events at different c.m. angles fitted by the two Gaussian functions. The blue dashed and the green dotted lines are the Gaussians due to the ground and 2^+_1 states at $E_x = 3.35$ MeV, respectively. The sums of the two Gaussians are plotted by the red solid lines.

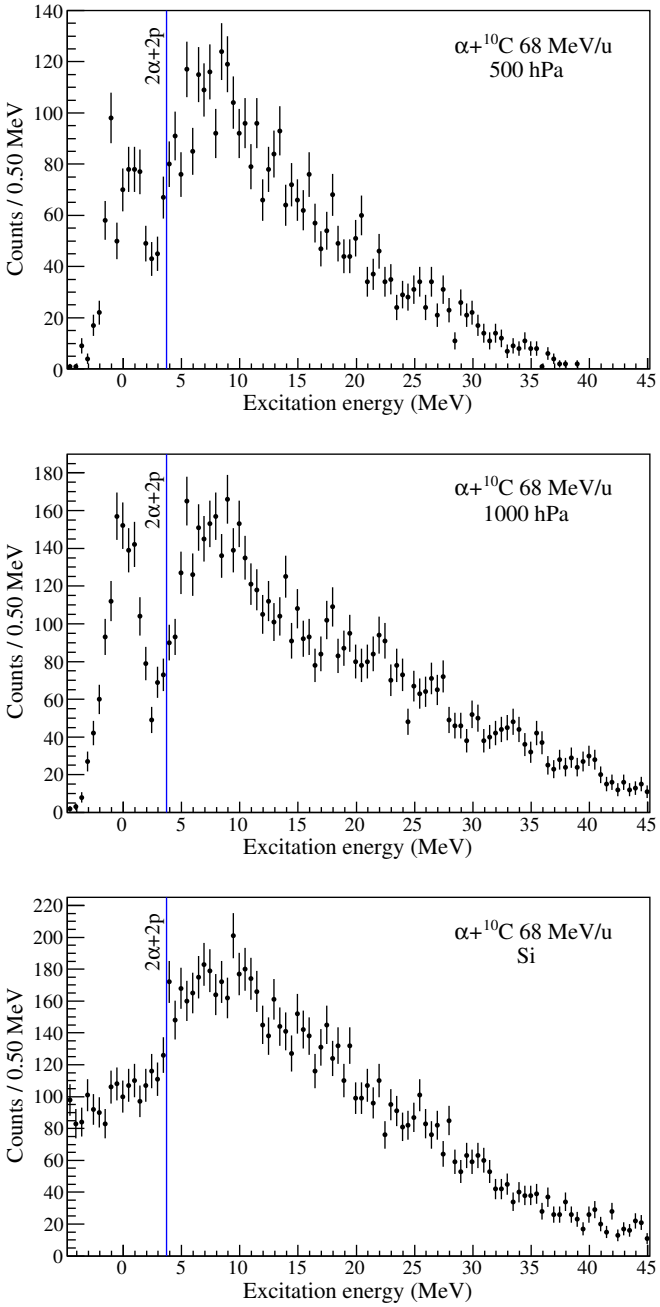

Figure 4.24: Excitation-energy spectra of the high-excitation events. The spectra of "500 hPa events", "1000 hPa events", and "Si events" are plotted in the top, middle, and bottom panels, respectively. The blue vertical lines show the $2\alpha + 2p$ threshold at $E_x = 3.73$ MeV.

4.8 Efficiency simulation

The geometrical detection efficiency and the track reconstruction efficiency of MAIKo were estimated from a Monte Carlo simulation. In the simulation, α+^{10}C events were generated. Positions and angles of incident ^{10}C particles, positions of scattering points, polar ($\theta_{\mathrm{lab.}}$) and azimuthal (ϕ) angles, and energies (E_α) of recoil alpha particles in the laboratory frame were randomly generated. "True values" of scattering angles in the c.m. system $\theta^t_{\mathrm{c.m.}}$ and excitation energies E^t_x were calculated from $\theta_{\mathrm{lab.}}$, E_α, and the ^{10}C energy. The spot size of the beam at the entrance of the TPC was set at 5 mm in sigma for both the horizontal and vertical positions. The energy of incident ^{10}C particles was fixed at 68 MeV/u. The incident angular spread of the beam were set at 6 mrad (horizontal) and 15 mrad (vertical) in sigma. These parameters were determined according to those measured by the beamline MWDCs.

Primary electrons were generated along the trajectories of the incident and scattered ^{10}C particles and the recoil alpha particles according to the SRIM calculation. The straggling of the recoil alpha particles through the TPC gas was considered. These primary electrons drifted towards the μ-PIC taking into account the transverse and longitudinal diffusions of the electrons. The diffusion coefficients were calculated with the computer code Magboltz [145]. An example of the generated trajectories of the incident and scattered ^{10}C and recoil alpha particle are plotted by the red lines in Fig. 4.25. In this example, $\theta_{\mathrm{lab.}}$ and ϕ of the recoil alpha particle are 85.4° and 60°, respectively. The recoil energy is 0.7 MeV.

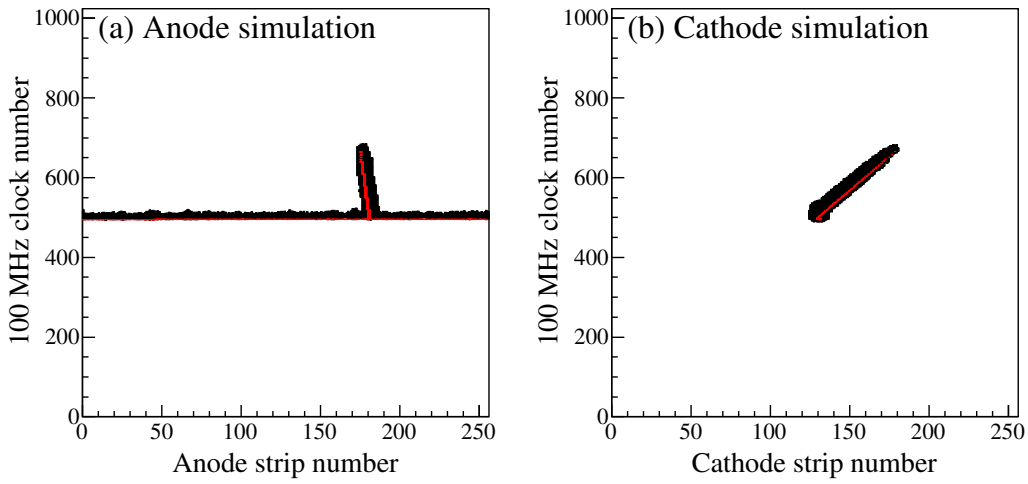

Figure 4.25: The simulated (a) anode and (b) cathode images of an α+^{10}C scattering. In this event, $\theta_{\mathrm{lab.}} = 85.4°$, $\phi = 60°$, and $E_\alpha = 0.7$ MeV. The generated trajectories are plotted by the red lines.

The analog signal from the μ-PIC for a single electron including the gas amplification on the electrodes and the response of the readout circuit was simulated using the computer code Garfield++ [146]. Figure 4.26 shows the average of the simulated waveforms over 2,000 events divided by the gas gain as a function of time [147]. The arrival time of the electrons at

the μ-PIC was folded by the analog signal for a single electron in Fig. 4.26, multiplied by the gas gain to simulate the induced signals in the scattering event. In the present simulation, the gas gain was assumed to have the Polya distribution according to Ref. [147]. The simulated signals were virtually processed and the anode and cathode images were generated as shown in Fig. 4.25.

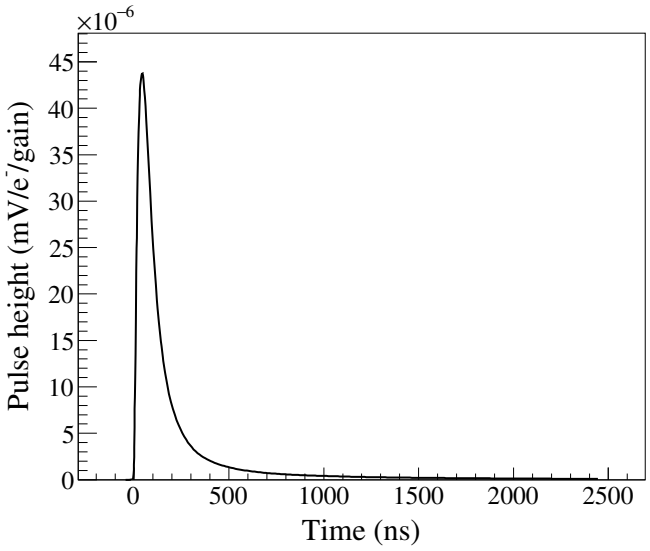

Figure 4.26: Averaged analog signal of the μ-PIC in the simulation for a single electron including the gas amplification processes on the electrodes and the response of the readout board [147]. The pulse height was divided by the gas gain.

The generated images were analyzed in the same manner as done for the real data, and the excitation energies E_x and the scattering angles $\theta_{\mathrm{c.m.}}$ were determined. The reconstructed excitation-energy spectrum for $-0.3 < E_x^t < 0.3$ MeV at $6.5^\circ < \theta_{\mathrm{c.m.}}^t < 6.9^\circ$ is shown in Fig. 4.27. The excitation-energy resolution at $E_x^t = 0$ MeV is 1.2 MeV in sigma, which is almost same with the experimental result of 1.1 MeV in Fig. 4.23. According to the simulation, this resolution is limited by the angular straggling of the recoil alpha particles.

At each $(E_x^t, \theta_{\mathrm{c.m.}}^t)$, the number of events reconstructed as a scattering event was divided by the number of the generated events at $(E_x^t, \theta_{\mathrm{c.m.}}^t)$ to estimate the detection and track reconstruction efficiencies $\epsilon(E_x^t, \theta_{\mathrm{c.m.}}^t)$. The obtained efficiencies as a function of E_x^t and $\theta_{\mathrm{c.m.}}^t$ are shown in Fig. 4.28. The top, middle, and bottom panels shows the efficiencies for the "500 hPa events", "1000 hPa events", and "Si events", respectively.

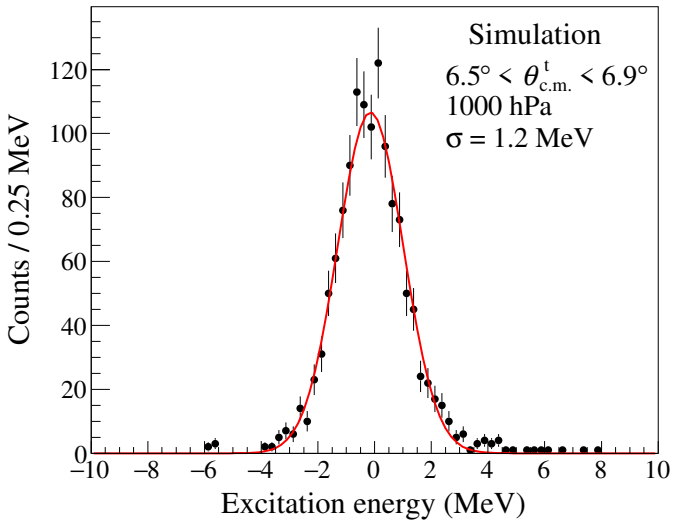

Figure 4.27: Reconstructed excitation-energy spectrum for $-0.3 < E_x^t < 0.3$ MeV at $6.5^\circ < \theta^t_{\mathrm{c.m.}} < 6.9^\circ$ in the simulation.

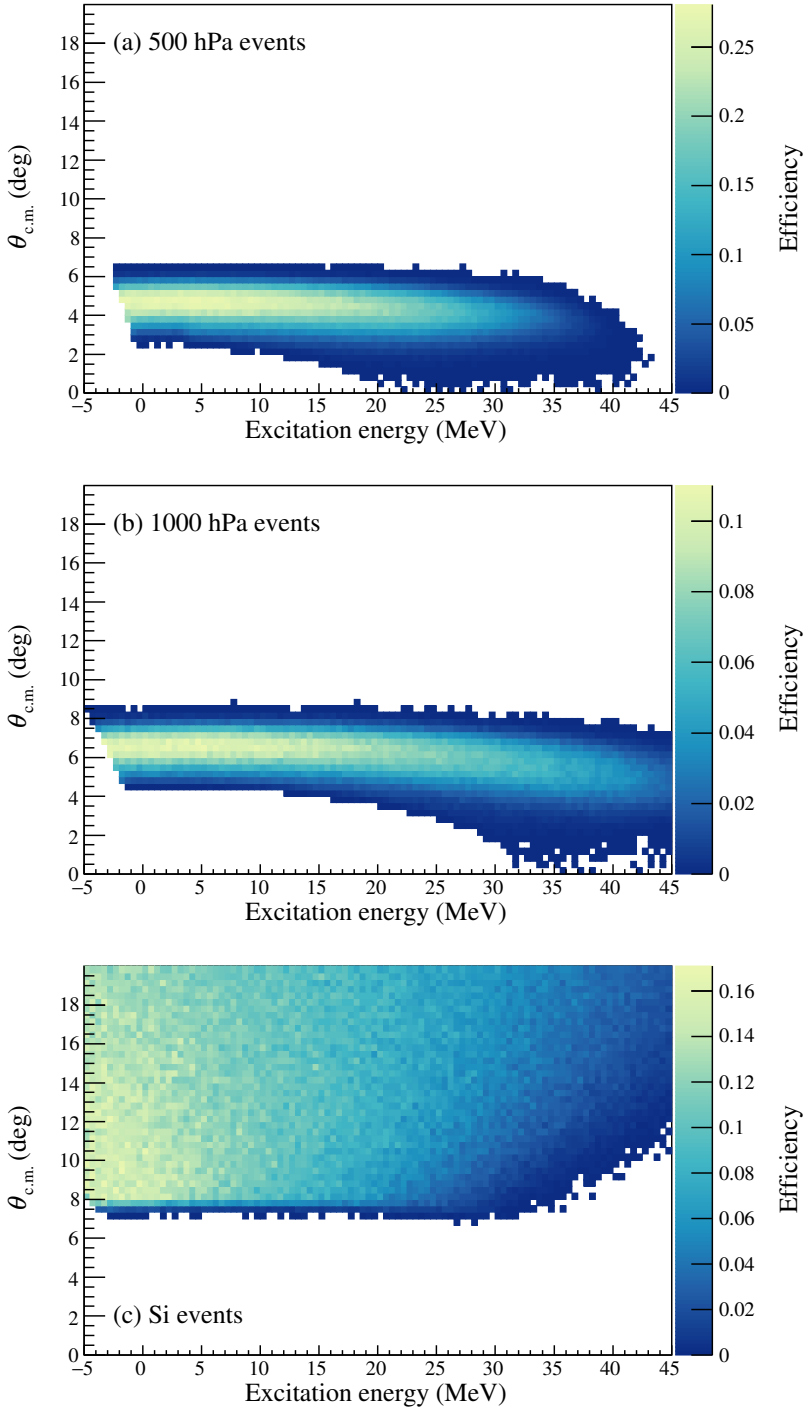

Figure 4.28: Geometrical detection and track reconstruction efficiency as a function of E_x^t and $\theta_{\mathrm{c.m.}}^t$. (a) "500 hPa events", (b) "1000 hPa events", and (c) "Si events".

4.9 Differential cross sections

Finally, the differential cross sections for the elastic scattering and the inelastic scattering to the 2_1^+ state at $E_x = 3.35$ MeV were obtained by

$$\frac{d\sigma}{d\Omega}(E_x, \theta_{\text{c.m.}}) = \frac{dN(E_x, \theta_{\text{c.m.}})}{2\pi \sin\theta_{\text{c.m.}} d\theta_{\text{c.m.}}} \times \frac{1}{\epsilon(E_x^t, \theta_{\text{c.m.}}^t) N_{\text{beam}} N_{\text{target}} t_{\text{live}}}. \tag{4.15}$$

Here, $dN(E_x, \theta_{\text{c.m.}})$ is the yield of the ground or 2_1^+ state. $\epsilon(E_x, \theta_{\text{c.m.}})$ is the detection and track reconstruction efficiency estimated by the simulation. N_{beam} is the number of the incident ^{10}C beam measured by the F3PL. N_{target} is the number of the ^{4}He atom per unit area. t_{live} is the live time ratio of the DAQ. Figure 4.29 shows the obtained differential cross sections of the elastic scattering and the inelastic scattering to the 2_1^+ state. The numerical values of the differential cross sections are listed in Appendix D.

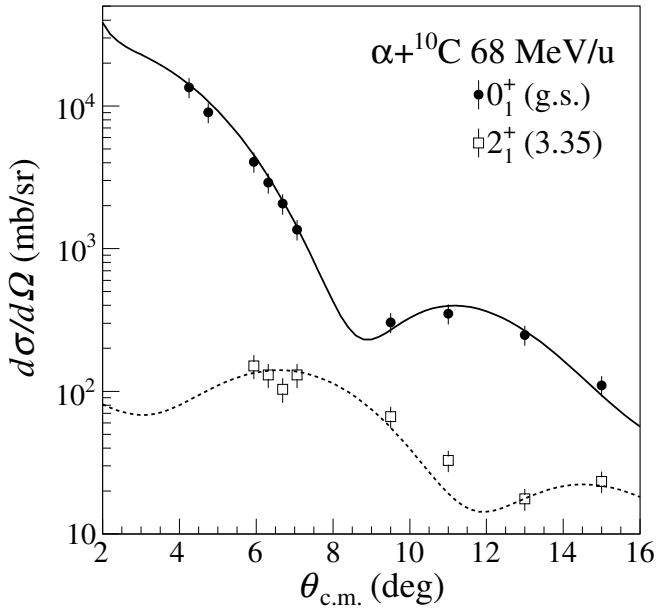

Figure 4.29: Differential cross sections of the α+^{10}C elastic (solid circles) and inelastic scattering to the 2_1^+ state at $E_x = 3.35$ MeV (open squares). The cross section of the elastic scattering calculated with the optical-model potential is plotted by the solid line. The cross section of the inelastic scattering obtained by the DWBA calculation is plotted by the dashed line.

4.10 Accuracy of the present analysis evaluated by the α+^{12}C elastic scattering

The differential cross sections of the α+^{12}C elastic scattering were measured with the present experimental setup and the ^{12}C primary beam in order to check the accuracy of the present analysis by comparing the present result with the previous result reported in Ref. [143].

In the present measurement, the ^{12}C primary beam was slowed down from 96 MeV/u to 94 MeV/u before entering of MAIKo due to the beamline detectors. The present cross section was obtained with the same analysis procedures with the α+^{10}C scattering described in the present chapter.

The previous data was measured at RCNP using a ^{4}He beam at 386 MeV (96.5 MeV/u) and the magnetic spectrometer Grand Raiden (GR) [148]. The two results are compared in Fig. 4.30. The solid circles and open squares represent the cross sections from the present and previous measurements, respectively. The uncertainties of the cross section were statistical only.

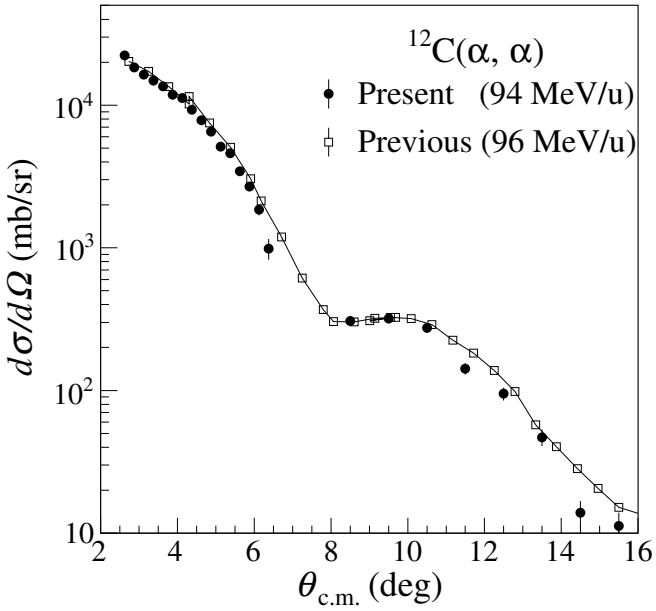

Figure 4.30: Differential cross sections for the α+^{12}C elastic scattering. The solid circles are the cross sections measured with MAIKo in the present work and the open squares represent the cross sections measured with the ^{4}He beam in the previous work [143]. The solid line connecting the open squares is drawn for guiding eyes.

The fractional differences between the present and previous results $[(d\sigma/d\Omega)_{\mathrm{MAIKo}} - (d\sigma/d\Omega)_{\mathrm{GR}}]/(d\sigma/d\Omega)_{\mathrm{MAIKo}}$ at various c.m. angles are plotted in Fig. 4.31. The present result agrees with the previous result qualitatively but it is systematically smaller than the previous result by 10% in average. The fractional differences fluctuate ±16% around the av-

erage value, which is much larger than the typical statistical uncertainties of a few percent. The uncertainty of the target density is smaller than 1% and the uncertainty in counting the incident beam particles using a plastic scintillator is typically 1%. Therefore, this fluctuation is considered to be mainly because of the uncertainty in estimating the detection and track reconstruction efficiency with the simulation. To incorporate uncertainty from the simulation, we simply added the 16% fractional uncertainty to the statistical uncertainty in quadrature in the following analysis. The error bars in Fig. 4.29 are plotted according to both the statistical and fractional uncertainties.

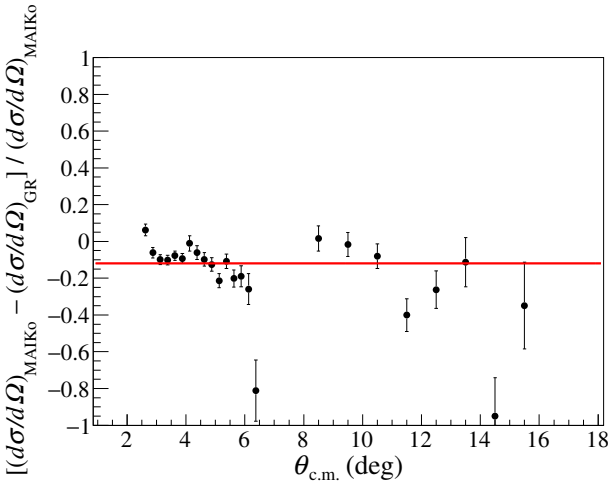

Figure 4.31: Fractional differences of the α+^{12}C elastic scattering cross sections between the present and previous results [143].

5 DWBA ANALYSIS

The measured α+^{10}C cross sections were compared with distorted wave Born-approximation (DWBA) calculations to extract the neutron transition matrix element M_n. First, the cross section of the elastic scattering was analyzed to obtain the effective α-N interaction. The transition potential to the 2_1^+ state was constructed by folding the obtained effective interaction with the macroscopic transition density. The M_n value was then determined to reproduce the cross section of the inelastic scattering. The DWBA calculations were performed using a computer code ECIS-95 [149].

5.1 Single-folding model and effective α-N interaction

The optical-model potential $U(\boldsymbol{r})$ for the α+^{10}C elastic scattering at 68 MeV/u was obtained by integrating a phenomenological α-N effective interaction u over the ^{10}C nucleus (single-folding model):

$$U(\boldsymbol{r}) = \int \Phi_c^*(\boldsymbol{r_1}, \boldsymbol{r_2}, ..., \boldsymbol{r_A}) \sum_{i=1}^{A} u(|\boldsymbol{r} - \boldsymbol{r_i}|) \Phi_c(\boldsymbol{r_1}, \boldsymbol{r_2}, ..., \boldsymbol{r_A}) d\boldsymbol{r_1} d\boldsymbol{r_2} \cdots d\boldsymbol{r_A} \tag{5.1}$$

Here, $\Phi_c(\boldsymbol{r_1}, \boldsymbol{r_2}, ..., \boldsymbol{r_A})$ is the wave function of the ground state in ^{10}C with $A = 10$ and $\boldsymbol{r}$ represents the position of the alpha particle from the center of the ^{10}C nucleus (see Fig. 5.1). $\boldsymbol{r_i}$ is the position of the i-th nucleon in ^{10}C with respect to the center of the ^{10}C nucleus. Using delta functions, Eq. (5.1) yields

$$\begin{aligned} U(\boldsymbol{r}) &= \int \Phi_c^*(\boldsymbol{r_1}, \boldsymbol{r_2}, ..., \boldsymbol{r_A}) \sum_{i=1}^{A} u(|\boldsymbol{r} - \boldsymbol{r'}|) \delta(\boldsymbol{r'} - \boldsymbol{r_i}) \Phi_c(\boldsymbol{r_1}, \boldsymbol{r_2}, ..., \boldsymbol{r_A}) d\boldsymbol{r_1} d\boldsymbol{r_2} \cdots d\boldsymbol{r_A} d\boldsymbol{r'} \\ &= \int \rho(\boldsymbol{r'}) u(|\boldsymbol{r} - \boldsymbol{r'}|) d\boldsymbol{r'}, \end{aligned} \tag{5.2}$$

with $\rho(\boldsymbol{r'})$ is the point-nucleon density distribution of the ^{10}C ground state:

$$\begin{aligned} \rho(\boldsymbol{r'}) &\equiv \int \Phi_c^*(\boldsymbol{r_1}, \boldsymbol{r_2}, ..., \boldsymbol{r_A}) \sum_{i=1}^{A} \delta(\boldsymbol{r'} - \boldsymbol{r_i}) \Phi_c(\boldsymbol{r_1}, \boldsymbol{r_2}, ..., \boldsymbol{r_A}) d\boldsymbol{r_1} d\boldsymbol{r_2} \cdots d\boldsymbol{r_A} \\ &= \langle \Phi_c | \sum_{i=1}^{A} \delta(\boldsymbol{r'} - \boldsymbol{r_i}) | \Phi_c \rangle. \end{aligned} \tag{5.3}$$

Since the spin parity of the ground state in ^{10}C is 0^+, only the transferred angular momentum of $\Delta L = 0$ is allowed, and thus the wave function and the density distribution of the ground state are treated as spherically symmetric hereafter.

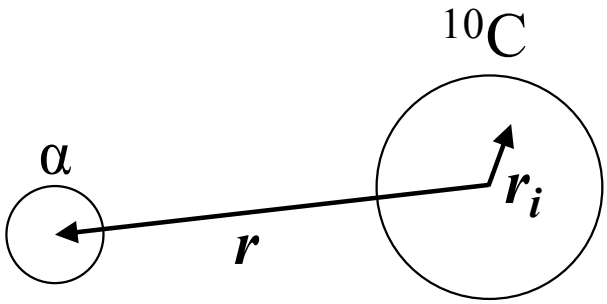

Figure 5.1: Definition of the spacial coordinates in Eq. (5.2).

We parametrize the phenomenological α-N interaction as in Ref. [150]:

$$\begin{aligned} u(|\boldsymbol{r}-\boldsymbol{r'}|) = &-V[1+\beta\rho^{2/3}(r')]\mathrm{e}^{-|\boldsymbol{r}-\boldsymbol{r'}|^2/\alpha_V^2} \\ &-iW[1+\beta\rho^{2/3}(r')]\mathrm{e}^{-|\boldsymbol{r}-\boldsymbol{r'}|^2/\alpha_W^2}. \end{aligned} \tag{5.4}$$

The parameters V and W are the strengths of the real and imaginary interactions, respectively. β is the density dependence parameter of the effective interaction. α_V and α_W are the range parameters of the real and imaginary interactions. These parameters are dependent on the incident energy and nucleus. Therefore, they have to be determined phenomenologically. Here, we note that the definition of α_V and α_W are changed from Ref. [150] so that they have the dimension of the length.

In the present analysis, it is assumed that the range parameters of the real and imaginary interactions are the same ($\alpha_V = \alpha_W = \alpha$), and the effective interaction is density independent ($\beta = 0$). According to a previous study [143], the density dependent ($\beta \neq 0$) and independent interactions give almost the same cross sections for the 2_1^+ states in the DWBA calculations once the parameters of the effective interaction are determined to reproduce the cross sections of the elastic scattering. Thus, we chose the density independent interaction for simplicity.

5.2 Determination of the range parameter

In an usual analysis as in Refs. [143, 151], the density distribution of the ground state is already determined from the electron scattering experiments, and only the effective interaction is optimized to reproduce the alpha elastic scattering. However, the density distribution of the ground state in ^{10}C has not been obtained from the electron scattering, both the effective interaction and the density distribution must be determined at the same time. Unfortunately, the effective interaction and the density distribution are not fully decoupled in the calcula-

Table 5.1: Effective interaction parameters for the α+^{12}C scattering at 60 MeV/u.

Parameter	Value
α	2.13 fm
V	17.9 MeV
W	6.96 MeV

tion of the cross section. Especially, the range parameter α in the effective interaction and the radius of the ^{10}C nucleus are strongly coupled. Therefore, these parameters can not be determined uniquely.

In this analysis, the range parameter α was determined not from the present α+^{10}C elastic scattering data, but from the previous α+^{12}C elastic scattering data at 60 MeV/u measured in the Texas A&M K500 superconducting cyclotron facility [152].

The previous data was analyzed using the density independent effective interaction described in Sec. 5.1. The point-nucleon density distribution of the ground state in ^{12}C was calculated from the charge distribution obtained by the electron scattering experiment as described in Appendix C.

The point-nucleon density distribution is a sum of the point-proton and point-neutron distributions. In the case of ^{12}C, the point-neutron distribution was assumed to be the same as the point-proton distribution because the charge symmetry is approximately established in light nuclei. The effective interaction parameters V, W, and α in Eq. (5.4) were determined so as to minimize the chi-square (χ^2) between the experimental and theoretical differential cross section:

$$\chi^2 = \sum_i \left(\frac{y_i^{\mathrm{exp}} - y_i^{\mathrm{cal}}}{\Delta y_i} \right)^2, \tag{5.5}$$

where y_i^{exp}, y_i^{exp}, and Δy_i are the i-th experimental value of the cross section, cross section calculated by the optical-model potential, and uncertainty of the cross section, respectively. The optimization of the parameters were performed using the Nelder-Mead algorithm [153] implemented in the SciPy library [154]. The obtained parameters are listed in Table 5.1. The differential cross section calculated using the optimized parameters are compared with the experimental data in Fig. 5.2. The optical-model calculation reasonably reproduces the experimental cross section. We used the same range parameter α in analyzing the α+^{10}C scattering data.

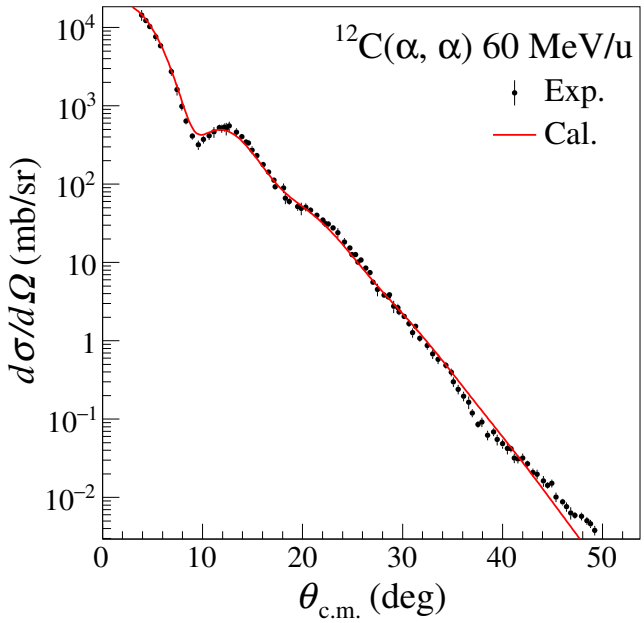

Figure 5.2: Differential cross section of the α+^{12}C elastic scattering at 60 MeV/u. The black solid circle and the red solid line represent the experimental data from Ref. [152] and optical single-folding model calculation, respectively.

5.3 Analysis of α+^{10}C elastic scattering

The point-nucleon distribution of the ground state in ^{10}C was parametrized with the three-parameter Gaussian (3pG) function:

$$\rho(r) = \frac{\rho_0(1 + wr^2/c^2)}{1 + \mathrm{e}^{(r^2-c^2)/z^2}}, \tag{5.6}$$

where c, z, and w are the parameters of the 3pG function. The normalization factor ρ_0 is determined so that it satisfies the relation:

$$4\pi \int \rho(r) r^2 dr = A, \tag{5.7}$$

where $A = 10$ is the mass number of ^{10}C. Note that while the point-nucleon density distribution of ^{12}C was deduced from the experimental results, the point-nucleon density distribution of ^{10}C was unknown.

The parameters V and W for the α-N effective interaction and the 3pG parameters c, z, and w were optimized so as to minimize the χ^2 of the cross section of the α+^{10}C elastic scattering, keeping the range parameter α at 2.13 fm which was taken from the α+^{12}C elastic scattering analysis. The optimized parameters are listed in Table 5.2, and the calculated cross section using these parameters is plotted by the solid line in Fig. 4.29. The reduced

Table 5.2: Optimized parameters for the α-N effective interaction and the point-nucleon distribution of the ground state in ^{10}C in the present analysis.

Interaction			3pG			
α (fm)	V (MeV)	W (MeV)	c (fm)	z (fm)	w	rms (fm)
2.13 (fixed)	$25.8^{+3.1}_{-2.1}$	$17.0^{+2.7}_{-2.0}$	0.21	1.98	-1.8×10^{-4}	2.6 ± 0.3

chi-square of the fitting χ^2/ν, where ν is the number of degrees of freedom, is 4.98/5, which means that the optical-model calculation reasonably reproduce the experimental data.

The standard uncertainties of V and W in Table 5.2 were estimated by allowing to increase the χ^2 value from the minimized value in the range

$$\chi^2 \leq \chi^2_{\rm min} + \Delta\chi^2. \tag{5.8}$$

When one parameter was varied, the other parameters were determined to minimize the χ^2 value. Then, $\Delta\chi^2$ obeys the χ^2 probability distribution for 1 degree of freedom. Thus, when $\Delta\chi^2$ is equal to 1, the variation of the parameter corresponds to the uncertainty at a confidence level of 68.3%. Figure 5.3 shows the χ^2 value as functions of the strengths of the effective α-N interaction: (a) V and (b) W. The χ^2 lines at $\chi^2_{\rm min} + 1$ are indicated by the red solid lines. The uncertainties of V and W in Table 5.2 were obtained from the ranges where $\chi^2 \leq \chi^2_{\rm min} + 1$.

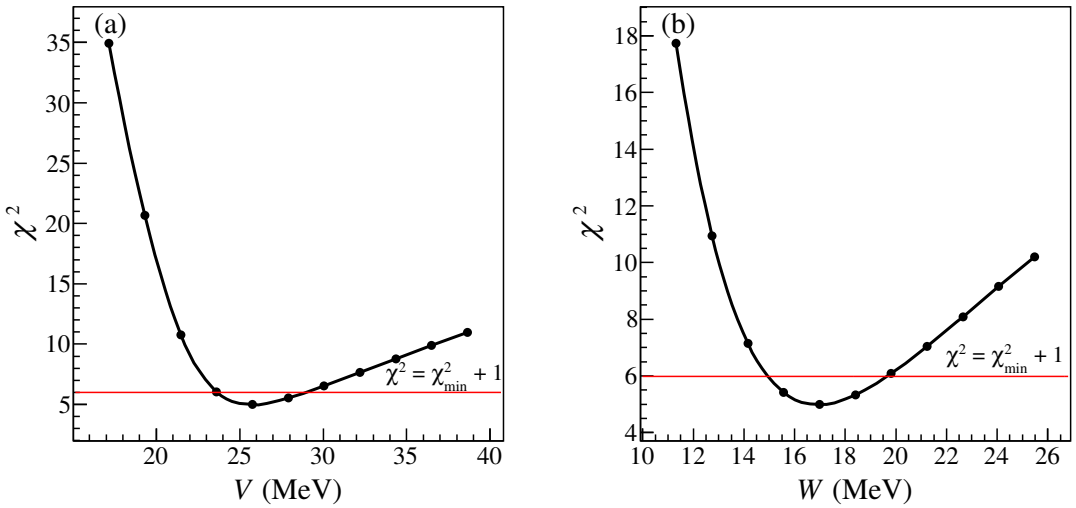

Figure 5.3: χ^2 values as functions of interaction strengths: (a) V and (b) W.

The obtained point-nucleon distribution of the ground state in ^{10}C is plotted in Fig. 5.4. The vertical axes of the left and right panels represent $\rho(r)$ and $r^2\rho(r)$, respectively. The point-nucleon distribution expressed by the best-fit 3pG function is plotted by the blue

solid line associated with its error band. The error band was estimated as an envelope with $\Delta\chi^2 \leq 3.5$ when the three parameters c, z, and w in the 3pG function were randomly varied. $\Delta\chi^2$ for multi parameters obeys the χ^2 distribution of ν degrees of freedom, where ν is the number of free parameters [155]. At a confidence level of 68.3%, $\Delta\chi^2$ for the three parameters c, z, and w in the 3pG function is 3.5. When the three parameters were varied, V and W were optimized to minimize χ^2. The uncertainty of $\rho(r)$ is large at small r because the present measurement is limited at forward angles in the c.m. frame.

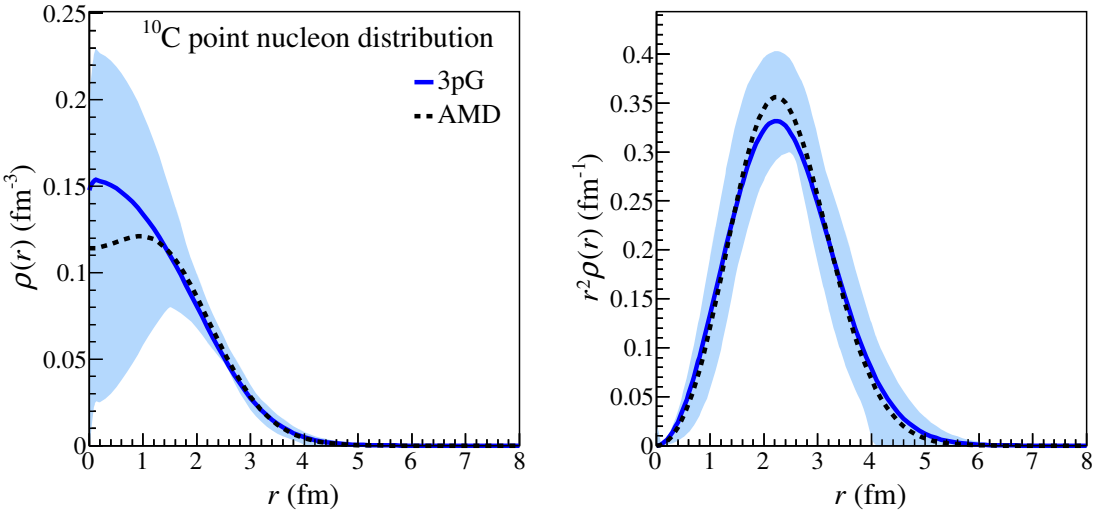

Figure 5.4: Point-nucleon distribution of the ground state in ^{10}C. Left panel: $\rho(r)$ as a function of r. Right panel: $r^2\rho(r)$ as a function of r. The density distribution obtained from the present work is shown by the blue solid line associated with the error band. The black dashed lines represent the density distribution calculated by AMD [156].

The obtained point-nucleon density distribution was compared with the theoretical prediction by the antisymmetrized molecular dynamics (AMD) model [156] which is plotted by the black dashed lines in Fig .5.4. The present result is consistent with the AMD calculation within the error band. The root-mean-square (RMS) radius of the point-nucleon distribution, defined as

$$\sqrt{\langle r^2 \rangle} = \frac{\int r^4 \rho(r) dr}{\int r^2 \rho(r) dr}, \tag{5.9}$$

is compared between the present result, previous experiments obtained by the proton elastic scattering [94] and the interaction cross section [157], and the AMD calculation [156] in Table 5.3. The present rms value is consistent with those from the proton elastic scattering experiment [94] and the AMD calculation, but slightly larger than that from the interaction cross section measurement [157].

Table 5.3: Comparison of the RMS radii of the ground state in ^{10}C obtained from the present and previous works.

Present	2.6 ± 0.3 fm
Proton elastic scattering [94]	2.42 ± 0.10 fm
Interaction cross section [157]	2.27 ± 0.03 fm
AMD calculation [156]	2.52 fm

5.4 Analysis of α+^{10}C inelastic scattering to the 2^+_1 state

In order to calculate the differential cross section of alpha inelastic scatterings using DWBA, we need to determine the transition potential $\delta U(r)$, which is defined as

$$\delta U(\boldsymbol{r}) = \int \Phi^*_{c'}(\boldsymbol{r_1}, \boldsymbol{r_2}, ..., \boldsymbol{r_A}) \sum_{i=1}^{A} u(|\boldsymbol{r} - \boldsymbol{r_i}|) \Phi_c(\boldsymbol{r_1}, \boldsymbol{r_2}, ..., \boldsymbol{r_A}) d\boldsymbol{r_1} d\boldsymbol{r_2} \cdots d\boldsymbol{r_A}. \tag{5.10}$$

where $\Phi^*_{c'}(\boldsymbol{r_1}, \boldsymbol{r_2}, ..., \boldsymbol{r_A})$ is the wave function of the excited state. The effective interaction parameters are the same as those determined in Sec. 5.3. Using a delta function, one obtains

$$\begin{aligned} \delta U(\boldsymbol{r}) &= \int \Phi^*_{c'}(\boldsymbol{r_1}, \boldsymbol{r_2}, ..., \boldsymbol{r_A}) \sum_{i=1}^{A} u(|\boldsymbol{r} - \boldsymbol{r'}|) \delta(\boldsymbol{r'} - \boldsymbol{r_i}) \Phi_c(\boldsymbol{r_1}, \boldsymbol{r_2}, ..., \boldsymbol{r_A}) d\boldsymbol{r_1} d\boldsymbol{dr_2} \cdots d\boldsymbol{r_A} d\boldsymbol{r'} \\ &= \int \delta\rho(\boldsymbol{r}) u(|\boldsymbol{r} - \boldsymbol{r'}|) d\boldsymbol{r'}. \end{aligned} \tag{5.11}$$

$\delta\rho(r)$ is the transition density between the ground and excited states which is defined as

$$\delta\rho(\boldsymbol{r}) \equiv \int \Phi^*_{c'}(\xi) \sum_{i=1}^{A} \delta(\boldsymbol{r} - \boldsymbol{r_i}) \Phi_c(\xi) d\xi = \langle \Phi_{c'} | \sum_{i=1}^{A} \delta(\boldsymbol{r} - \boldsymbol{r_i}) | \Phi_c \rangle. \tag{5.12}$$

The transition density expresses the overlap of the wave functions between the initial and final states. It can be expanded with the sum of different multipoles as [158]

$$\delta\rho(\boldsymbol{r}) = \sum_{\lambda} \delta\rho^{(\lambda)}(r) \sum_{\mu} Y^*_{\lambda\mu}(\hat{\boldsymbol{r}}) \langle J_c M_c \lambda\mu | J_{c'} M_{c'} \rangle, \tag{5.13}$$

where $J_{c,c'}$ and $M_{c,c'}$ represent the angular momenta and magnetic quantum numbers. The Clebsch-Gordan coefficients have the non-zero values only when λ and μ take $|J_{c'} - J_c| \leq \lambda \leq |J_{c'} + J_c|$ and $\mu = M_{c'} - M_c$. For the transition from the 0^+_1 state to the 2^+_1 state, only the $\lambda = 2$ terms have non-zero values.

In the present analysis, the macroscopic model [159] was used. The macroscopic model treats the nuclear excitation modes as small-amplitude collective oscillations of a liquid drop

about its equilibrium shape. Using this model, the quadrupole transition ($\Delta L = 2$) density from the ground state to the 2^+_1 state is given as

$$\delta\rho^{(2)}_{n(p)}(r) = -\delta_{n(p)}\frac{d}{dr}\rho_{n(p)}(r), \tag{5.14}$$

where $\delta_{n(p)}$ is the deformation length for neutron (proton), and $\rho_{n(p)}(r)$ is the point density distribution of neutron (proton) of the ground state in ^{10}C. Assuming that the neutron and proton distributions have the same shape, one can obtain the point proton and neutron distribution:

$$\rho_p(r) = \frac{Z}{A}\rho(r) \tag{5.15}$$

$$\rho_n(r) = \frac{N}{A}\rho(r). \tag{5.16}$$

The density distribution $\rho(r)$ is expressed by Eq. (5.6) with the parameters in Table 5.2.

The quadrupole transition matrix element of neutron (proton) was calculated from the transition density with

$$M_{n(p)} = \int r^4 \delta\rho^{(2)}_{n(p)}(r)dr. \tag{5.17}$$

The reduced electromagnetic transition rate $B(E2; 0^+_1 \to 2^+_1)$ is related to the proton transition matrix element M_p by

$$B(E2; 0^+_1 \to 2^+_1) = e^2|M_p|^2. \tag{5.18}$$

Here we note that since a proton is not a point-like particle strictly, its charge form factor should be taken into account when M_p is compared with $B(E2; 0^+_1 \to 2^+_1)$ in principle. However, the difference of M_p calculated directly from the point-proton distribution and that calculated from the charge distribution obtained by applying Eq. (C.3) to the 3pG point-proton distribution is only 1.9%. Since this difference is much smaller than the uncertainties of M_n described below, we calculated M_p directly from the point-proton distribution for simplicity. The proton deformation length δ_p was determined so as to reproduce the known $B(E2; 0^+_1 \to 2^+_1)$ value in ^{10}C reported in Ref. [117]:

$$B(E2; 0^+_1 \to 2^+_1) = 44.5 \pm 1.5\ e^2\mathrm{fm}^4. \tag{5.19}$$

It should be noted that the neutron deformation length δ_n is the last remaining free parameter to calculate the differential cross section of the alpha inelastic scattering using the DWBA and the transition potential in Eq. (5.11).

δ_n was determined to be 2.4 fm by fitting the calculated cross sections to the experimental data as shown by the dashed line in Fig. 4.29. The reduced χ^2 of the fitting was $\chi^2/\nu = 10.9/7$. Using Eq. (5.14), the transition densities from the ground state to the 2^+_1 state were obtained as shown in Fig. 5.5. By integrating the neutron transition density with Eq. (5.17), we obtained the neutron transition matrix element from the ground state to the 2^+_1

state as $M_n = 6.9$ fm^2.

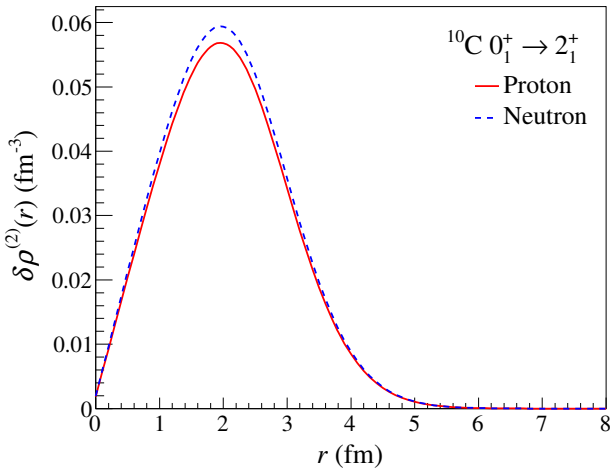

Figure 5.5: Proton and neutron quadrupole transition densities from the ground state to the 2^+_1 state in ^{10}C. The proton transition density is plotted by the red solid line, while the neutron transition density is plotted by the blue dashed line.

The uncertainty of M_n associated with the fitting procedure was estimated by changing M_n values in the range that satisfies Eq. (5.8). In the present fitting, since the free parameter is only M_n or δ_n, $\Delta\chi^2$ is equal to 1. Figure 5.6 shows the χ^2 value calculated by changing M_n. The red horizontal line is drawn at $\chi^2 = \chi^2_{\rm min} + 1$. The resulting uncertainty of M_n was determined to be ± 0.4 fm^2 from the range where $\chi^2 \leq \chi^2_{\rm min} + 1$.

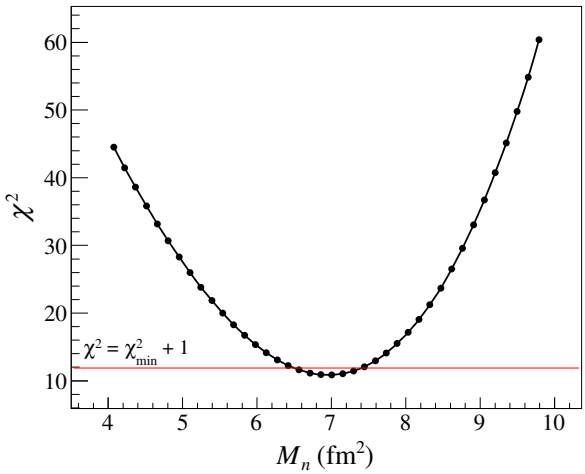

Figure 5.6: χ^2 value of the cross section for the 2^+_1 state in ^{10}C as a function of M_n.

The uncertainties of the effective interaction and the 3pG parameters also result in an additional uncertainty in M_n. This uncertainty was estimated to be ± 0.6 fm^2 by taking

different parameter sets of V, W, c, z, and w randomly generated in the range that satisfies $\chi^2 \leq \chi^2_{\rm min} + 1$ for the elastic scattering data and deduced the M_n values using these parameters. Adding this uncertainty to that obtained in the previous paragraph in quadrature, we obtained the total uncertainty coming from the fitting procedure as $\sqrt{(0.4)^2 + (0.6)^2} = 0.7$ fm^2.

In Ref. [143], the differential cross sections of the alpha inelastic scattering exciting the 2^+ states in stable self-conjugate even-even nuclei from ^{12}C to ^{40}Ca were systematically measured at $E_\alpha = 386$ MeV. The authors calculated the differential cross sections using a single-folding model similar to the present method. They obtained δ_p from the know $B(E2; 0^+_1 \to 2^+_1)$ values, assuming $M_n = M_p$ because the proton and neutron numbers are the same. The ratio R of the experimental cross sections to the calculated cross sections are shown in Fig. 5.7, which is taken from Fig. 15 in Ref. [143]. The fluctuation of R around the unity is 17% in the standard deviation. This fluctuation corresponds to the uncertainty of the single-folding model in the DWBA calculation. Therefore, we adopt $\pm$17% ($\pm$1.2 fm^2) as a systematic uncertainty associated to the error in the DWBA analysis with the single-folding model. Other systematic uncertainties, *i.e.*, uncertainties of the target density (0.1%) and the number of beam particles (3%) are negligibly small compared to that of the DWBA analysis.

Finally, we obtained the M_n value and its uncertainties in the $0^+_1 \to 2^+_1$ transition in ^{10}C as

$$M_n = 6.9 \pm 0.7\,(\text{fit}) \pm 1.2\,(\text{sys})\,\text{fm}^2. \tag{5.20}$$

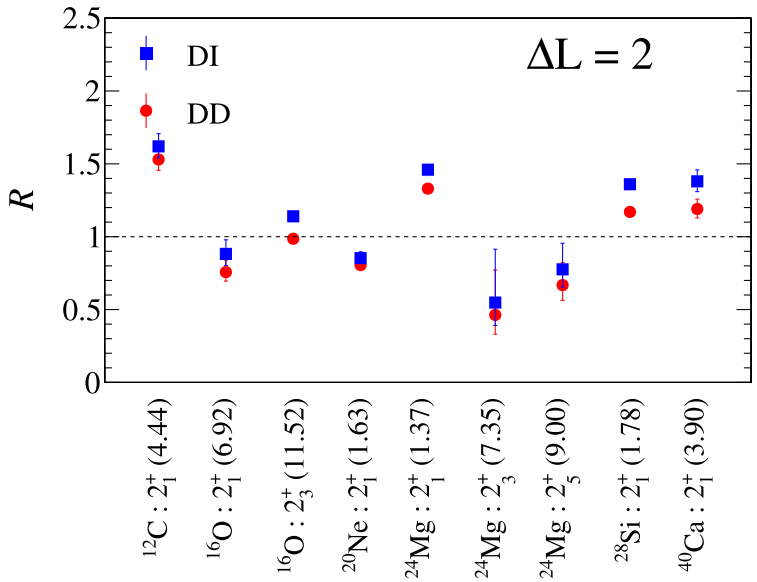

Figure 5.7: Ratio $R = \sigma_{\rm exp}/\sigma_{\rm cal}$ of the measured cross sections to the calculated cross sections using the single-folding model. The figure is taken from Fig. 15 in Ref. [143].

6 DISCUSSION

6.1 Comparison with the previous results

If one assumes the charge symmetry in the ^{10}C-^{10}Be system, the neutron transition matrix element M_n in ^{10}C should be equal to the proton transition matrix element M_p in ^{10}Be. The M_p value in ^{10}Be was measured as $M_p = 6.78 \pm 0.11$ fm^2 using the Doppler shift attenuation method [160]. This value is actually close to the present M_n value in ^{10}C, and thus the charge symmetry in the $A = 10$ system is almost conserved.

On the other hand, the previous proton inelastic scattering measurement reported a different M_n value in ^{10}C of $M_n = 5.51 \pm 1.09$ fm^2 [94], which is significantly smaller than the M_p value in ^{10}Be. The authors claimed that the mirror symmetry was not fulfilled in the ^{10}C-^{10}Be system, which is attributed to the Coulomb effect. The discrepancy between the present and previous results is possibly because the authors in Ref. [94] used the old $B(E2; 0^+_1 \rightarrow 2^+_1)$ value of 61.5 ± 10 e^2fm^4 from Ref. [114]. This value is larger than the new value of 44.0 ± 1.5 e^2fm^4 [117] which was reported after the proton inelastic scattering measurement. This larger $B(E2; 0^+_1 \rightarrow 2^+_1)$ value might lead to a smaller value of M_n in the previous analysis. If we use the old $B(E2; 0^+_1 \rightarrow 2^+_1)$ value to analyze the present cross section of the alpha inelastic scattering, we obtained the smaller M_n value in ^{10}C as $M_n = 5.7 \pm 0.6\,(\text{fit}) \pm 1.0\,(\text{sys})$ fm^2 which is close to the previous result.

6.2 Comparison with theoretical calculations

As mentioned in Sec. 1.6, the ratio of the neutron and proton transition matrix elements from the ground states to the 2^+_1 states M_n/M_p (single ratio) is a useful probe to investigate nuclear shell structures. The single ratio in ^{10}C deduced from the present measurement is

$$M_n/M_p = 1.05 \pm 0.11\,(\text{fit}) \pm 0.17\,(\text{sys}), \tag{6.1}$$

which is close to unity.

The present results of the transition matrix elements and the single ratio are compared with the results of the proton inelastic scattering [94] and various theoretical calculations in Table 6.1. In the $2p+2\alpha$ four-body cluster-model calculation [161], the fully antisymmetrized 10-nucleon wave functions were built in a microscopic $2p + 2\alpha$ configuration space using the Minnesota potential [162]. The no-core shell model calculation [163] was conducted using the CD-Bonn N-N potential [164] in the configuration space up to $8\hbar\Omega$ with the harmonic oscillator frequency of $\hbar\Omega = 14$ MeV. The shell-model calculation [165] was carried out within

Table 6.1: Comparison of the transition matrix elements of proton and neutron from the ground state to the 2_1^+ state in ^{10}C. Single ratios of the transition matrix elements M_n/M_p are also listed.

	M_p (fm^2)	M_n (fm^2)	M_n/M_p
Present	6.63 ± 0.11 [117]	$6.9 \pm 0.7 \pm 1.2$	$1.05 \pm 0.11 \pm 0.17$
(p, p') [94]	7.84 ± 0.64 [114]	5.51 ± 1.09	0.70 ± 0.08
Cluster [161]	5.5	4.4	0.8
No-core shell model [163]	5.3	5.7	1.1
Shell model [165]	3.3	4.3	1.3
Monte Carlo shell model [167]	6.8	6.8	1.0
AMD [169]	5.3	6.9	1.3

the p shell using the Cohen and Kurath (8-16)2BME interaction [166]. The shell-model transition matrix elements were calculated using single-particle wave functions in the harmonic oscillator potential with $b = 1.64$ fm and effective charges of $e_p = 1.3e$ and $e_n = 0.5e$. In the Monte Carlo shell-model calculation [167], the unitary-correlation-operator-method potential based on the chiral next-to-next-to-next-to-leading-order two nucleon interaction [168] with the bare charges ($e_p = e$ and $e_n = 0$) was used to calculate the transition matrix elements. The M_n value in ^{10}C by the Monte Carlo shell-model calculation was taken from the M_p value calculated in the mirror nucleus ^{10}Be assuming the charge symmetry. In the AMD calculation [169], the wave function was given by a single Slater determinant of Gaussian functions with the width parameter of $\nu = 0.15$ fm^{-2}.

The theoretical calculations tend to underestimate the transition matrix elements M_p and M_n except the Monte Carlo shell-model calculation and the M_n value calculated by the AMD model. Especially, the M_p and M_n values predicted by the shell-model calculation are considerably smaller than the experimental values. However, all of the theoretical calculations agree with the M_n/M_p values close to unity.

6.3 $Z = 6$ shell closure

The M_n/M_p ratio in ^{10}C is almost unity, whereas a large M_n/M_p ratio of 3.2 ± 0.7 was reported in ^{16}C [101]. This suggests that the quadrupole transition in ^{10}C is less neutron dominant than ^{16}C and the effect of the $Z = 6$ shell closure proposed in the neutron-rich carbon isotopes [77] is less evident in proton-rich ^{10}C.

If one assumes that the deformation lengths of the proton and neutron distributions are the same, the M_n/M_p ratio is expected to be N/Z [see Eq. (1.9)]. Taking this assumption, the double ratio $(M_n/M_p)/(N/Z)$ has been widely used to discuss the nuclear shell structures [85]. When the neutron (proton) shell is closed, the double ratio becomes smaller (larger) than unity because the transition of the neutron (proton) is remarkably suppressed. The experimental double ratios in various single or double closed nuclei are shown in Fig. 6.1.

The plotted values are the weighted averages of the experimental values derived by various hadronic probes compiled in Ref. [84]. The double ratios in proton-closed nuclei plotted by the circles are systematically larger than unity, whereas those in neutron-closed nuclei plotted by the triangles are smaller than unity.

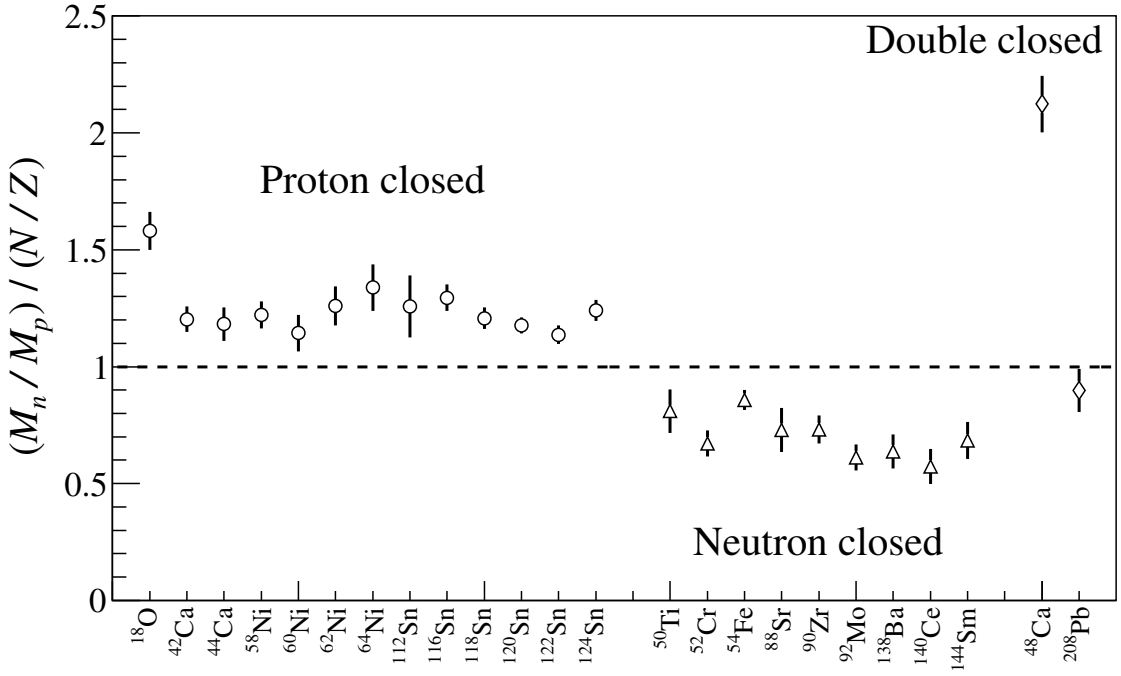

Figure 6.1: Double ratios in proton-closed (circles), neutron-closed (triangles), and double-closed (diamonds) nuclei. The plotted values are the weighted averages of the experimental values compiled in Ref. [84].

The double ratios in the even-even $T_z = -1$ ($Z = N + 2$) nuclei are plotted in Fig. 6.2. The M_p values were calculated using Eq. (5.18) and the $B(E2; 0_1^+ \to 2_1^+)$ values were taken from Refs. [170, 171]. The M_n values in ^{18}Ne–^{46}Cr were obtained by assuming the charge symmetry:

$$M_n(N, Z) = M_p(Z, N). \tag{6.2}$$

As seen in the figure, the double ratios are close to unity when both the proton and neutron shells are open (open squares). On the other hand, the double ratios deviate from unity when the proton or neutron shell is closed. In case of ^{18}Ne and ^{42}Ti (open triangles), neutrons tend to contribute less to the excitation than protons since the neutron shells are closed at the $1p_{1/2}$ and $1d_{3/2}$ orbitals, respectively. In case of ^{38}Ca (open circle), the proton contribution is reduced because the proton shell is closed at the $1d_{3/2}$ orbital.

The double ratio in ^{10}C obtained from the present work is plotted by the solid circle. The fitting and systematic uncertainties are indicated by the solid and dashed vertical lines, respectively. It should be noted that the double ratio in ^{10}C was deduced in the present work

without relying on the charge symmetry. Although we concluded that the $Z = 6$ shell closure or magicity is less evident in ^{10}C, it was found that the double ratio in ^{10}C is significantly larger than unity as those in the proton-closed nuclei.

$$(M_n/M_p)/(N/Z) = 1.57 \pm 0.17\,(\text{fit}) \pm 0.27\,(\text{sys}). \tag{6.3}$$

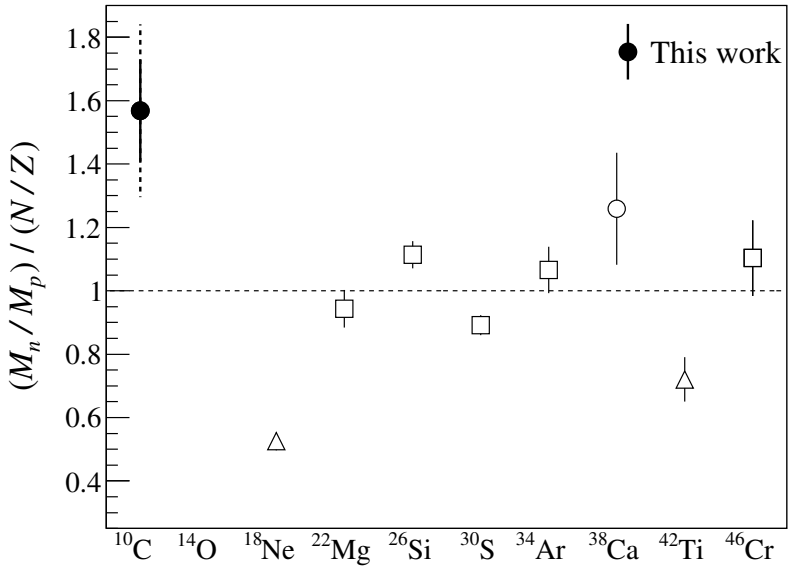

Figure 6.2: Double ratios $(M_n/M_p)/(N/Z)$ for the quadrupole transitions from the ground states to the 2_1^+ states in the even-even $T_z = -1$ nuclei. The double ratio in ^{10}C determined in the present measurement is plotted by the solid circle, and the fitting and systematic uncertainties are presented by the vertical solid and dashed lines, respectively. The open squares are the double ratios in open shell nuclei. The open circle and triangles represent proton and neutron closed nuclei, respectively.

The AMD calculation [172] explains the reason of this contradiction. The deformations in the ground states in ^{16}C and ^{20}C predicted by the AMD calculation are illustrated in Fig. 6.3. The AMD calculation suggests both the proton and neutron distributions exhibit the oblate deformation in ^{20}C as illustrated in the right side. Such a same deformation in proton and neutron distributions is a usual trend in stable nuclei. On the other hand, in case of ^{16}C, the deformation of the proton and neutron distributions are decoupled, that is, the oblate proton and prolate neutron deformations whose symmetric axes are perpendicular to each other. Therefore, the assumption to use the double ratio, that the deformation lengths of the proton and neutron distributions are the same, is no longer valid in this nucleus. The AMD calculation suggests that the proton and neutron deformations in ^{10}C are also decoupled like ^{16}C [173]. Therefore, the large double ratio observed in ^{10}C does not necessarily suggests the $Z = 6$ shell closure in the proton-rich carbon isotope.

The present conclusion that the $Z = 6$ shell closure is less evident in ^{10}C is consistent

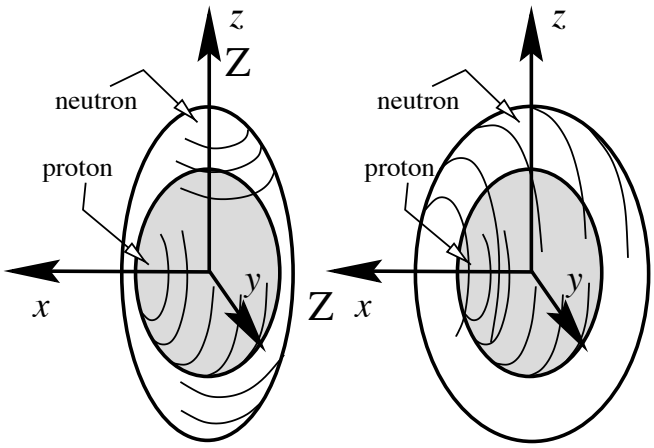

Figure 6.3: Deformations of the proton and neutron distributions in carbon isotopes in the AMD calculation. (a): Oblate proton and prolate neutron deformations in ^{16}C. (b): Oblate proton and oblate neutron deformations in ^{20}C. The principal axes for the ground-state $K^\pi = 0^+$ band are denoted as Z. The figure is taken from Fig. 4 in Ref. [172].

with the known $B(E2; 0_1^+ \rightarrow 2_1^+)$ values in carbon isotopes. Since the quadrupole transition is described as rearrangement of the particle-hole configuration in the valence shell, the $B(E2; 0_1^+ \rightarrow 2_1^+)$ value tends to become small for proton-closed nuclei. The measured $B(E2; 0_1^+ \rightarrow 2_1^+)$ values in ^{16}C [93, 100, 101, 105], ^{18}C [101, 106], ^{20}C [104] are only 1.1–2.3 W.u.. These values are comparable to the proton-closed oxygen isotopes, *i.e.*, 3.1 W.u. in ^{18}O [174], and thus the $Z = 6$ shell closure is evident in above neutron-rich carbon isotopes. On the other hand, the $B(E2; 0_1^+ \rightarrow 2_1^+)$ value in ^{10}C is 6.9 ± 0.2 W.u. [117] and not small compared to those in the neutron-rich carbon isotopes. This fact also supports the present conclusion that the $Z = 6$ shell closure is less evident in the proton-rich side.

6.4 Future perspectives

6.4.1 Upgrade of the MAIKo detector

The present work demonstrated that the MAIKo active target is successful in performing the missing-mass spectroscopy to investigate the nuclear structures of unstable nuclei. It shall be utilized in various incoming RI beam experiments. However, it is expected that the beam intensity and the statistics will become smaller when we are to explore with the unstable nuclei beam far from the stability region. The active target method can compensate the reduction of the beam intensity by extending the detector size along the beam axis which increases the target thickness.

We are planning to enlarge the sensitive volume of the MAIKo TPC from $100 \times 100 \times 140$

mm^2 to 300 × 300 × 300 mm^2. This upgrade will increases the target thickness by a factor of three. Moreover, the energy acceptance of the recoil alpha particles which stop inside the TPC sensitive volume will become three times larger than that of the present TPC. This can significantly reduce the beam time because the measurements for low-energy recoil particles at forward c.m. angles and for high-energy recoil particles at relatively backward c.m. angles were carried out separately in the present work. The statistics will become approximately a factor of nine.

In addition to the enlargement of the TPC, the configuration of the readout strip will be changed from the two-axial X–Y structure to the three-axial X–U–V structure as shown in Fig. 6.4. In the present two-axial strips, only the vertical angle of the beam particles can be determined since the X strips are parallel to the beam axis. We installed the additional MWDC detectors to monitor the horizontal angle, but this makes the analysis procedure complicated if we are to determine the angle of the incident beam which is scattered in the TPC. In the upgraded MAIKo TPC, we are considering to arrange the readout strips at 60 degrees. Although the X strips are still parallel to the beam axis, the three dimensional angle of the beam particles can be determined from the U and V strips.

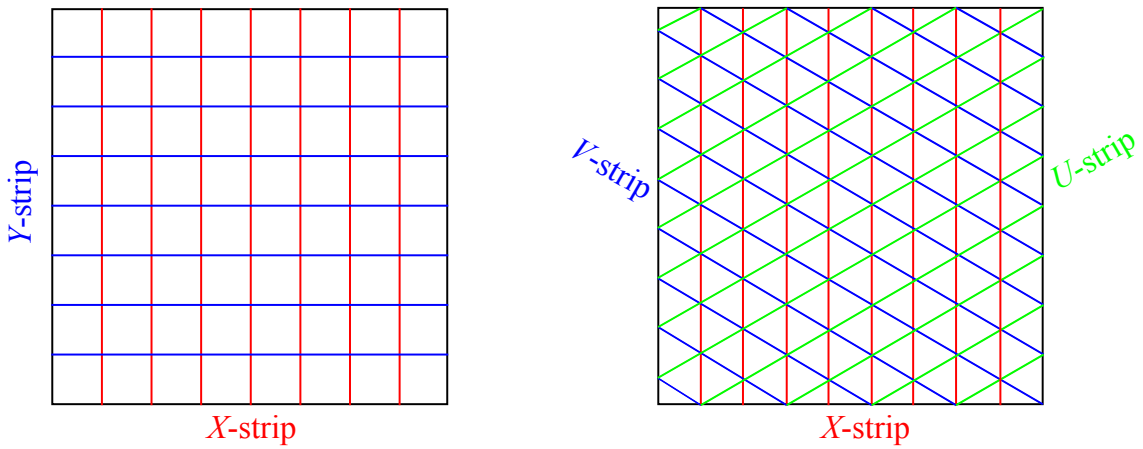

Figure 6.4: Structures of the readout strips. Left: Two-axial strips utilized in the present MAIKo TPC. Right: Three-axial strips planed in the upgraded TPC.

6.4.2 Search for alpha cluster states

As described in Sec. 1.4.2.2, the MAIKo active target is a suited device to search for alpha cluster states in unstable nuclei because it enables the measurement at forward c.m. angles where the cross sections for exciting spatially well-developed cluster states become large. As a next physics experiment with MAIKo, we aim to examine the alpha cluster states in ^{10}Be and ^{10}C.

A recent theoretical calculation with the generalized two-center cluster model (GTCM) describes the cluster structures in the ^{10}Be-^{10}C mirror system and suggests that the differ-

ences of the cluster configurations are reflected in monopole transition strengths and energy shifts.

Figure 6.5 schematically shows the alpha cluster structures in ^{10}C predicted by GTCM [175]. The 0_1^+ state is considered to be a $2\alpha + 2p$ molecular state in which two valence protons occupy the π-molecular orbital formed by two alpha particles. The 0_2^+ state is another 2α+$2p$ molecular structure in which the valence protons occupy the σ-molecular orbital. On the other hand, the 0_3^+ and 0_4^+ states are predicted to have α+^{6}Be structures in which the relative motion between the two alpha clusters are dominated by the s wave and d wave, respectively.

The isoscalar monopole transition strengths $B(E0)$ from the ground state to excited states are enhanced when the relative motion of the two alpha clusters in the ground state is excited. According to the GTCM calculation, the 0_4^+ state is excited by stimulating the relative motion of the two alpha clusters in the ground state. This transition is denoted as cluster excitation in the figure. The 0_2^+ state is excited by rearranging the valence protons which is denoted as molecular orbital (MO) excitation. The 0_3^+ state is excited by the cluster excitation of the 0_2^+ state. The 0_4^+ state is predicted to have the largest $B(E0)$ value of 57 fm^4 among the three excited states while the 0_2^+ and 0_3^+ states have about half $B(E0)$ values of 28 fm^4 and 23 fm^4, respectively. Therefore, the $B(E0)$ values provide information to distinguish these different alpha cluster configurations.

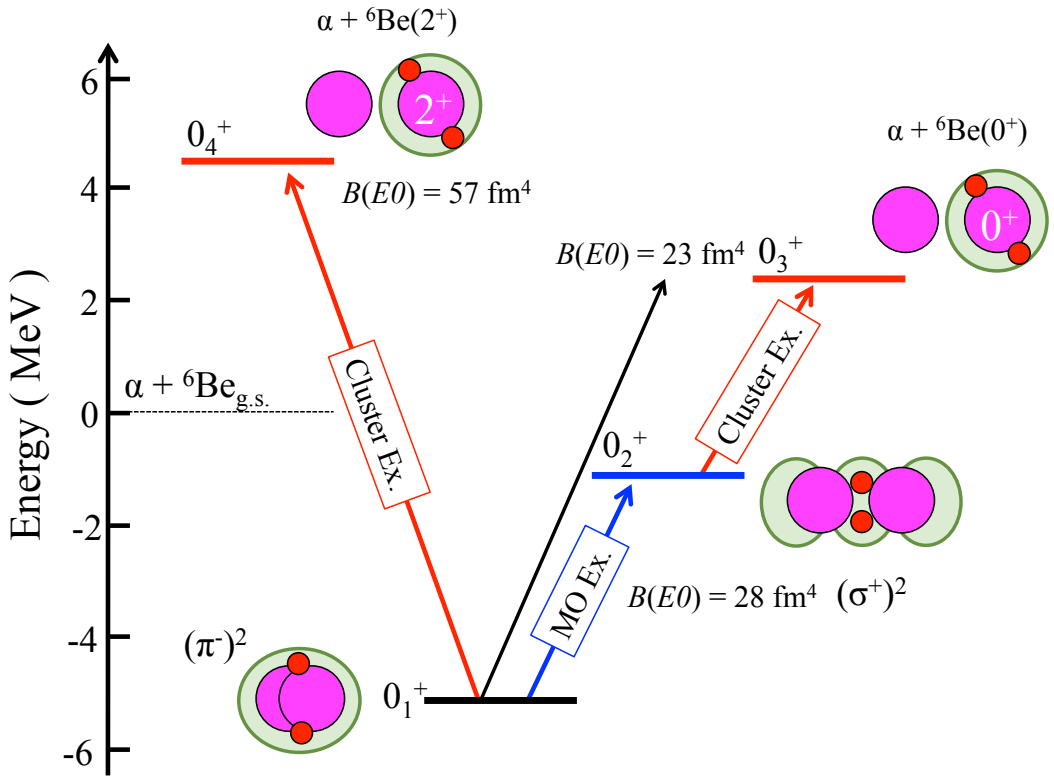

Figure 6.5: Alpha cluster structures in ^{10}C predicted by the GTCM calculation [175].

The energy shifts between the isobaric analog states are expected to be a new observable to clarify the alpha cluster structures [176–178]. Due to the Coulomb interaction, the analog states in the proton-rich nuclei usually shift to higher energies than those in the neutron-rich mirror nuclei. It is naively expected that these energy shifts become small as the radii of the analog states increase. Figure 6.6 shows the level structure of the 0^+ states in the ^{10}Be-^{10}C system predicted by the GTCM calculation [176]. The energy shift of the 0^+_1 states is predicted to be 2.3 MeV, which is the largest energy shift among the four 0^+ states. This large energy shift is because of the spatially compact structure due to the two valence nucleons in the π-molecular orbital. The energy shift of the 0^+_2 states is predicted to be 1.3 MeV which is smaller than that between the 0^+_1 states due to the loosely bound σ-molecular orbital. Because the 0^+_3 and 0^+_4 states have spatially well-developed α+^{6}He/^{6}Be cluster structures, the energy shifts of these states are even smaller: 0.6 MeV and 0.8 MeV, respectively. The smaller energy shift of the 0^+_3 states than the 0^+_4 states is because the relative angular momenta between the two clusters in the 0^+_3 states are zero. They are not confined in the centrifugal potential which makes them spatially more expanded than the 0^+_4 states. These differences in the energy shift are the the analogy of the well-known Thomas-Ehrman shift originally discussed in the single particle states in the ^{13}C-^{13}N system [179, 180].

As discussed above, a systematic measurement of the energies and the isoscalar monopole transition strengths in the ^{10}Be-^{10}C system are desired to investigate the cluster structures. The 0^+_2 state in ^{10}Be was experimentally found at $E_x = 6.18$ MeV [113]. However, the 0^+_3 and 0^+_4 states have never been found in ^{10}Be. On the other hand, in ^{10}C, no 0^+ excited state has been found. We obtained the excitation-energy spectra in ^{10}C above the particle decay threshold from the present measurement as shown in Fig. 4.24. In order to deduce the monopole transition strengths from the present measurement, the angular distribution of the differential cross section at each excitation-energy should be determined. However, the present statistics is not sufficient to reliably determine the differential cross section at each excitation energy and at each c.m. angle. We will carry out further measurements both on ^{10}Be and ^{10}C after upgrading the MAIKo active target to achieve about nine times higher statistics which ensures us to obtain the angular distribution of the differential cross section at each excitation-energy.

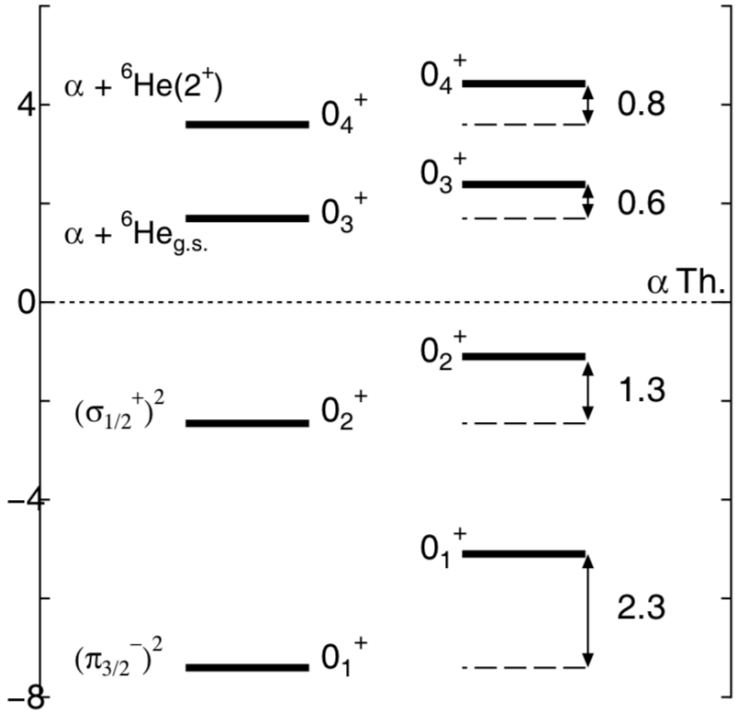

Figure 6.6: Level structure of the 0^+ states in the ^{10}Be (left)-^{10}C (right) mirror system. The figure was taken from Fig. 1 in Ref. [176].

7 SUMMARY

The missing-mass spectroscopy is a promising method to investigate the structures in unstable nuclei. However, the measurement at forward scattering angles in the c.m. system is technically difficult because the energies of the recoil particles are extremely small. In order to realize the detection of such low-energy recoil particle, we developed a new active target system named MAIKo [41]. MAIKo is based on a TPC in which the detector gas is used as a target gas. Since the scatterings occur inside the sensitive volume of the TPC, the detection threshold for the recoil particles are lowered. The size of the MAIKo TPC is $100 \times 100 \times 140$ mm^3. We introduced the μ-PIC [42] for the amplification and detection of the drift electrons and achieved the finest readout pitch among the existing active target systems.

As the first physics experiment using MAIKo, we performed the alpha elastic and inelastic scatterings off ^{10}C at 68 MeV/u at RCNP, Osaka University [76]. The aim of the experiment is to deduce neutron transition matrix element M_n from the ground state to the 2^+_1 state at $E_x = 3.35$ MeV in ^{10}C and discuss the $Z = 6$ magicity in the proton-rich carbon isotope.

An almost pure ^{10}C secondary beam with an intensity of 70 kcps was produced from a ^{12}C primary beam at 96 MeV/u. The missing-mass spectroscopy with MAIKo was performed to determine the excitation energy in ^{10}C. MAIKo was operated with the He(96%)+CO_2(4%) gas mixture at 500 and 1000 hPa. We successfully detected low-energy recoil alpha particles down to $E_\alpha = 0.5$ MeV with MAIKo as designed, which corresponds to the momentum transfer down to $q = 0.4$ fm^{-1}.

The trajectories of the recoil alpha particles were reconstructed with the Hough transformation. Only the α+^{10}C events were selected from other background events by the track reconstruction algorithm and the particle identification. The parameters in the track reconstruction procedures were optimized from the eye-scanned data samples. The excitation-energy resolution was about 1 MeV in sigma, which was good enough to distinguish the first excited 2^+_1 state at $E_x = 3.35$ MeV from the ground state in ^{10}C. A Monte Carlo simulation was performed to estimate the detection and track reconstruction efficiencies. The differential cross sections of the α+^{10}C elastic scattering and the inelastic scattering exciting the 2^+_1 state were determined at $4.5° < \theta_{\mathrm{c.m.}} < 15°$.

The differential cross section of the α+^{12}C elastic scattering was also measured using a primary ^{12}C beam at 94 MeV/u. The measured cross section was compared with the previous data measured under the normal kinematic condition using a ^{4}He beam at 96 MeV/u [143]. We confirmed that both results are consistent quantitatively, demonstrating the reliability of the present measurement with MAIKo.

From the analysis of the cross section of the α+^{10}C elastic scattering, the phenomenological α-N effective interaction and the point-nucleon distribution of the ground state in

^{10}C were determined. The rms radius of 2.6 ± 0.3 fm in ^{10}C is consistent with the theoretical prediction by the AMD calculation [156] and the experimental result of the previous proton elastic scattering [94], but slightly larger than that deduced from the interaction cross section [157].

By comparing the measured cross section of the α+^{10}C inelastic scattering exciting the 2_1^+ state with the DWBA calculation, the neutron transition matrix element of $M_n = 6.9 \pm 0.7\,(\mathrm{fit}) \pm 1.2\,(\mathrm{sys})$ was obtained. The present experiment is the first attempt to determine the neutron transition matrix element in unstable nuclei from the alpha inelastic scattering. The alpha inelastic scattering enables us to deduce the neutron transition matrix element without model ambiguity better than the inelastic proton scattering which has been widely applied to the RI beam experiments.

Because the obtained M_n value in ^{10}C is close to the M_p value in the mirror nucleus ^{10}Be, we concluded that the isospin symmetry in the $A = 10$ system is almost conserved. The ratio of the neutron transition matrix element to the proton transition matrix element was determined as $M_n/M_p = 1.05 \pm 0.11\,(\mathrm{fit}) \pm 0.17\,(\mathrm{sys})$. The ratio close to unity suggests that the recently proposed $Z = 6$ shell closure is less evident in proton-rich ^{10}C nucleus than the neutron-rich side. The fact that M_n/M_p larger than $N/Z = 2/3$ can be attributed to the decoupling of the proton and neutron distributions predicted by the AMD calculation [172].

After the long-standing development since 2011, the first physics experiment using MAIKo has been successfully completed. The MAIKo active target provides a breakthrough to realize the measurement of the alpha inelastic scattering at low-momentum transfer region under the inverse kinematic condition. MAIKo is now under an upgrade program to explore more exotic side and it shall be utilized in many incoming RI beam experiments in the near future.

Acknowledgement

The present thesis would not have been completed without the dedicated and kind supports from many people. I would like to take this opportunity to express my sincere thanks to them.

First and foremost, I would like to express my great appreciation to my supervisor, Prof. Takahiro Kawabata. He provided me the opportunity to undertake the interesting and challenging project to develop a new active target system from almost scratch. Since I was an undergraduate student, he has been continuously encouraged and supported for the planning and carrying out the experiments, the data analysis, and writing the thesis even after he moved from Kyoto University to Osaka University. Moreover, he taught me the most important thing, to enjoy research and life. It was my privilege to be his student.

I am really grateful to Prof. Hooi Jin Ong at RCNP. He gave me invaluable advice on the experiment at RCNP and discussions on the obtained physics results. He also kindly helped me for writing the articles.

I gratefully acknowledge the present and past members of our research group: Dr. Satoshi Adachi, Mr. Naoki Yokota, Mr. Tomosuke Kadoya, Mr. Hidetomo Watanabe, Ms. Miho Tsumura, Mr. Tatsuo Baba, Mr. Motoki Murata, Mr. Yuki Ishii, Mr. Takahiro Morimoto, Ms. Akane Sakaue, Mr. Kento Inaba, Mr. Yu Takahashi, Mr. Tomoya Takeda, Mr. Yuki Fujikawa, Mr. Takanobu Doi, Mr. Shintaro Okamoto, and Mr. Kohsuke Sakanashi. We spent quite a long time on many experiments through which I felt a genuine camaraderie. They made great contributions to the development of MAIKo and the present measurement. I also enjoyed daily conversation with them. The long time with them has been matured my personality.

The present E463 experiment was successfully carried out thanks to the hard and professional works by the collaborators: Dr. Yassid Ayyad, Prof. Michele Sferrazza, Prof. Isao Tanihata, and Dr. Dinh Trong Tran.

I would like to express my gratitude to Prof. Nori Aoi, Prof. Yoshiko Kanada-En'yo, Prof. Kazuyuki Ogata, and Prof. Harutaka Sakaguchi for the fruitful discussions about the theoretical interpretation of the results. My special thanks go to Prof. Makoto Ito who motivated me to start the present experiment showing me the interesting clustering aspects of ^{10}C. I am grateful to Prof. Tomokazu Suzuki, Dr. Takashi Hashimoto and Dr. Junki Tanaka for helping the development of MAIKo. I also acknowledge Dr. Hidetada Baba at RIKEN for helping the development of the DAQ system.

The MAIKo active target was successfully developed owing to the supports from the Cosmic Ray group at Kyoto University. I would like to express my great appreciation to Prof. Toru Tanimori, Prof. Hidetoshi Kubo, Prof. Atsushi Takada, Dr. Shigeto Kabuki, Dr. Tatsuya Sawano, Dr. Yoshitaka Mizumura, Dr. Tetsuya Mizumoto, and Dr. Yoshihiro

Matsuoka.

The low-pressure MWDCs which were used in the present experiment were newly developed with the help from Prof. Yohei Matsuda, Prof. Satoru Terashima, Prof. Juzo Zenihiro. I am also grateful to Kaizu Works company, Liftec company, Swagelok company, MKS company, Seiwa Sangyo company, Horiba company, and Horiguchi company for the kind help and advice in making the experimental equipment used in the present measurement.

I am truly grateful to the staffs in RCNP for their supports. Especially, Prof. Atsushi Tamii, Prof. Nobuyuki Kobayashi, Mr. Shinji Ano, Prof. Tomokazu Suzuki, Mr. Michio Uraki, Dr. Yusuke Yasuda, and Dr. Hidetomo Yoshida for technical supports on experiments. The experiment was stably performed thanks to the cyclotron crews. I deeply appreciate the staffs at the RCNP office for providing the comfortable guest house during the experiments.

I would like to express my great gratitude to the staffs at Experimental Nuclear and Hadronic Physics Laboratory (NH) at Kyoto University, Prof. Tomofumi Nagae, Prof. Megumi Naruki, Prof. Juzo Zenihiro, Prof. Tetsuya Murakami, Prof. Hiroyuki Fujioka, Prof. Masayuki Niiyama, and Prof. Toshiyuki Gogami for the encouragements and suggestions throughout the time in the university. I would like to also acknowledge all of the members in the NH group and office staffs at Department of Physics. I enjoyed discussions, research activities, recreations, BBQ, and drinkings with them.

After six year in Kyoto University, I started to work at RCNP. I am grateful to all of the staffs and students in NP-1A group for discussions and supports.

I appreciate the financial supports of Grant-in-Aid for JSPS Research Fellow JP14J00949.

I am indebted to all of my friends in my university life for the emotional supports. I was really happy with them.

Finally but not least, I would like to express my sincere appreciation to my parents, sister, and grand parents. Without their kind supports and understandings, it would have been impossible to reach this goal.

Appendix A
Hough transformation

The Hough transform algorithm was originally developed by Hough for the analysis of the bubble chamber pictures [181] and later modified by Duda and Hart [182]. It enables to extract features in a picture such as lines or circles without knowing how many features exist in the picture. This algorithm is now widely applied in image recognition because of its high immunity to random noises compared to other algorithms like the least-square method.

The anode and cathode images obtained by MAIKo contain 256×1024 black-and-white pixels. When coordinates of the i-th black pixel in an image are expressed as $(x_i,\ y_i)$ in the track space, this pixel is transformed to a curve in the $(\theta,\ r)$ parameter space (Hough space) given by Eq. (A.1) in the Hough transformation.

$$r = x_i \cos\theta + y_i \sin\theta. \tag{A.1}$$

In the track space as shown in Fig. A.1(a), the red, blue, and green points at $(x_i,\ y_i)$, $(x_{i+1},\ y_{i+1})$, and $(x_{i+2},\ y_{i+2})$ are transformed into the red, blue, and green curves in the Hough space as shown in Fig. A.1(b), respectively. The j-th pixel at (θ_j, r_j) in the Hough space corresponds to a straight line in the track space as:

$$y = -\frac{x}{\tan\theta_j} + \frac{r_j}{\sin\theta_j}. \tag{A.2}$$

As shown in Fig. A.1(a), r corresponds to the distance from the origin to the straight line, and θ corresponds to the angle between the x axis and the perpendicular line from the origin.

If several pixels in the track space lie on a straight line, their transformed curves intersect at one point in the Hough space, which corresponds to the original straight line in the track space.

In the present analysis, the transformed curves were discretized into bins and these bins were booked into a two-dimensional histogram in the Hough space. The number of the bins of the histogram in the Hough space was 180×256. The trajectories with sizable length make clear peaks in the Hough histogram while the small spots caused by noises do not. By finding the bin with the maximum entry in the Hough histogram, which is easy to implement in a computer program, the longest trajectory in the image was extracted.

After the first trajectory was extracted, the black pixels near the first line were eliminated from the image. The remaining pixels were again transformed into the Hough space. The second trajectory was determined by the highest bin in the second Hough histogram. The Hough transformation and the elimination were repeated until the number of entry in the

highest bin in the Hough histogram became lower than a certain threshold. With this method, multiple trajectories were successfully extracted from the images.

Here it should be noted that the smaller bin size in the Hough histogram does not necessarily lead to an accurate determination of the trajectories. If we adopt the smaller bin size, the number of the entries in the highest bin in the Hough histogram becomes smaller, thus this makes the analysis susceptible to noises and difficult to determine the highest bin. In order to achieve the better accuracy in determining the trajectories, we fitted another straight line to the black pixels near the straight line extracted by the Hough transformation.

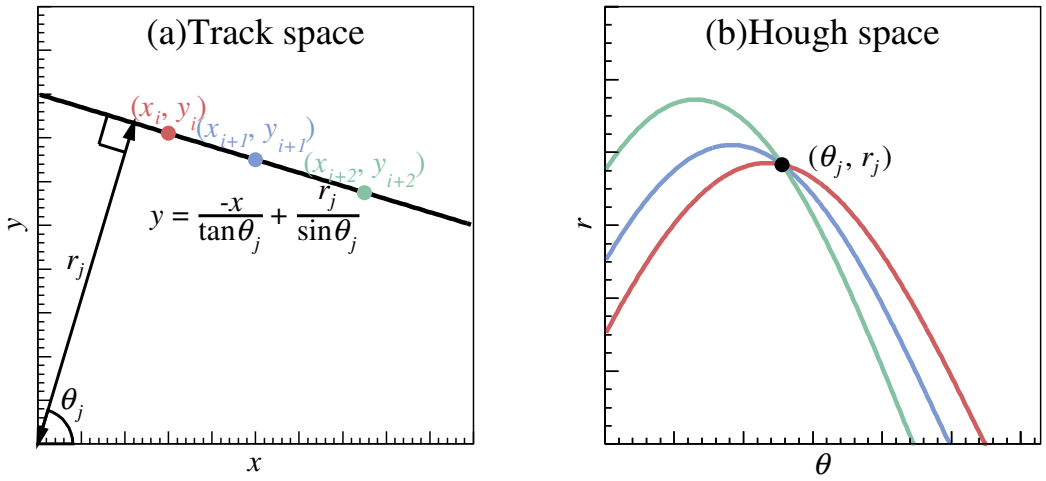

Figure A.1: Example of the Hough transformation. The the red, blue, and green points at $(x_i,\ y_i)$, $(x_{i+1},\ y_{i+1})$, and $(x_{i+2},\ y_{i+2})$ in the left panel (a) are transformed into the red, blue, and green curves in the right panel (b) according to Eq. (A.1), respectively.

Appendix B
Relativistic kinematics

In this appendix, the formulae to reconstruct the excitation energy and center of mass angle in the inverse kinematic condition are presented.

The excitation energy of the incident particle E_x is calculated using the relativistic kinematics as

$$E_x = \sqrt{s + t + u - m_1^2 - m_2^2 - m_3^2} - m_4, \tag{B.1}$$

where m_1 and m_4 are the rest mass of the incident particle and m_2 and m_3 are the rest mass of the target particle. s, t, and u are the Mandelstam variables defined as

$$\begin{aligned} s &= m_1^2 + m_2^2 + 2m_2E_1, & \text{(B.2)} \\ t &= m_1^2 + m_3^2 + 2(p_1p_3\cos\theta_3 - E_1E_3), & \text{(B.3)} \\ u &= m_2^2 + m_3^2 - 2m_2E_3. & \text{(B.4)} \end{aligned}$$

Here, θ_3 is the angle of the recoil particle in the laboratory frame. E_1, E_3 are the energies while p_1 and p_3 are the momenta given as

$$\begin{aligned} E_1 &= m_1 + K_1, & \text{(B.5)} \\ E_3 &= m_3 + K_3, & \text{(B.6)} \\ p_1 &= \sqrt{E_1^2 - m_1^2}, & \text{(B.7)} \\ p_3 &= \sqrt{E_3^2 - m_3^2}, & \text{(B.8)} \end{aligned}$$

where K_1 and K_3 are the kinetic energies of the incident and recoil particles, respectively. The center of the mass scattering angle $\theta_{\text{c.m.}}$ is calculated from several parameters below.

$$W = \sqrt{m_1^2 + m_2^2 + 2m_1E_1}, \tag{B.9}$$

is the total energy in the c.m. frame.

$$\begin{aligned} p_{1,\text{c.m.}} = p_{2,\text{c.m.}} &= \frac{1}{2W}\sqrt{[W^2 - (m_1 + m_2)^2][W^2 - (m_1 - m_2)^2]}, & \text{(B.10)} \\ p_{3,\text{c.m.}} = p_{4,\text{c.m.}} &= \frac{1}{2W}\sqrt{[W^2 - (m_3 + m_4)^2][W^2 - (m_3 - m_4)^2]}, & \text{(B.11)} \end{aligned}$$

are the momenta in the c.m. frame.

$$E_{i,\mathrm{c.m.}} = \sqrt{m_i^2 + p_{i,\mathrm{c.m.}}^2}, \tag{B.12}$$

$$\gamma_{i,\mathrm{c.m.}} = \frac{E_{i,\mathrm{c.m.}}}{m_i}, \tag{B.13}$$

$$\beta_{i,\mathrm{c.m.}} = \frac{p_{i,\mathrm{c.m.}}}{E_{i,\mathrm{c.m.}}}, \tag{B.14}$$

are the energy, gamma factor, and velocity in the c.m. frame, respectively. Finally, $\theta_{\mathrm{c.m.}}$ is calculated as

$$\theta_{\mathrm{c.m.}} = \arccos(\lambda + \tau), \tag{B.15}$$

where

$$\lambda = -\frac{\beta_{2,\mathrm{c.m.}}}{\beta_{3,\mathrm{c.m.}}} \frac{(\gamma_{i,\mathrm{c.m.}} \tan\theta_3)^2}{1 + (\gamma_{i,\mathrm{c.m.}} \tan\theta_3)^2}, \tag{B.16}$$

$$\tau = \frac{\sqrt{[1 - (\beta_{2,\mathrm{c.m.}}/\beta_{3,\mathrm{c.m.}})^2]\gamma_{2,\mathrm{c.m.}} \tan\theta_3 + 1}}{1 + (\gamma_{i,\mathrm{c.m.}} \tan\theta_3)^2}. \tag{B.17}$$

Appendix C
Point proton density distribution of the ground state in ^{12}C

In this appendix, the procedure to obtain the point proton density distribution of the ground state in ^{12}C from the charge distribution is described.

The charge distribution ρ_0^c given in Ref. [183] was parametrized with the sum of Gausians (SOG) as follows:

$$\rho_0^c(r) = \sum_i A_i \left\{ \exp\left[-\left(\frac{r - R_i}{\gamma} \right)^2 \right] + \exp\left[-\left(\frac{r + R_i}{\gamma} \right)^2 \right] \right\}, \tag{C.1}$$

with

$$A_i = ZeQ_i \left[2\pi^{2/3}\gamma^3 \left(1 + \frac{2R_i^2}{\gamma^2} \right) \right]^{-1}. \tag{C.2}$$

The parameters R_i, Q_i, and γ in Eqs. (C.1) and (C.2) were determined so as to reproduce the cross section of the elastic electron scattering. We took the values from Ref. [183] as listed in Table C.1.

The point-proton distribution $\rho_0^p(r)$ was calculated by unfolding the charge distribution of Eq. (C.1) with the proton charge form factor [184] since the charge distribution $\rho_0^c(r)$ is given by folding $\rho_0^p(r)$ with the charge distribution in a proton $\rho_p^c(r)$ as follows:

$$\rho_0^c(r) = \int \rho_0^p(r')\rho_p^c(r - r')dr'. \tag{C.3}$$

Here, we assumed that $\rho_0^p(r)$ and $\rho_p^c(r)$ are spherically symmetric. The Fourier transformation of this equation is expressed by

$$F^c(q) = F^p(q)G_p(q), \tag{C.4}$$

where q is the momentum transfer and $F^c(q)$, $F^p(q)$, and $G_p(q)$ represent the Fourier transformations of $\rho_0^c(r)$, $\rho_0^p(r)$, and $\rho_p^c(r)$, respectively. $F^c(q)$ was calculated from the charge density in Eq. (C.1) by

$$F^c(q) = \frac{4\pi}{q} \int \rho_0^c(r) \sin(qr) dr, \tag{C.5}$$

and $G_p(q)$, known as Sachs electric form factor of proton [185], was empirically parametrized

Table C.1: Parameters of SOG for the charge distribution of the ^{12}C ground state from Ref. [183].

	Parameter	Value
i	R_i (fm)	Q_i
1	0.0	0.016690
2	0.4	0.050325
3	1.0	0.128621
4	1.3	0.180515
5	1.7	0.219097
6	2.3	0.278416
7	2.7	0.058779
8	3.5	0.057817
9	4.3	0.007739
10	5.4	0.002001
11	6.7	0.000007
	γ (fm)	0.98

in Ref. [186] as:

$$G_p(q) = \frac{0.312}{1+q^2/6.0} + \frac{1.312}{1+q^2/15.02} - \frac{0.709}{1+q^2/44.08} + \frac{0.085}{1+q^2/154.2}. \tag{C.6}$$

Therefore, $F_p(q)$ was calculated from Eqs. (C.4), (C.5) and (C.6). Finally, the point-proton distribution $\rho_0^p(r)$ was obtained by the inverse Fourier transformation of $F_p(q)$ as

$$\rho_0^p(r) = \int \frac{F^c(q)}{G_p(q)} \sin(rq) dq. \tag{C.7}$$

The obtained charge and point-proton density distributions are compared in Fig. C.1.

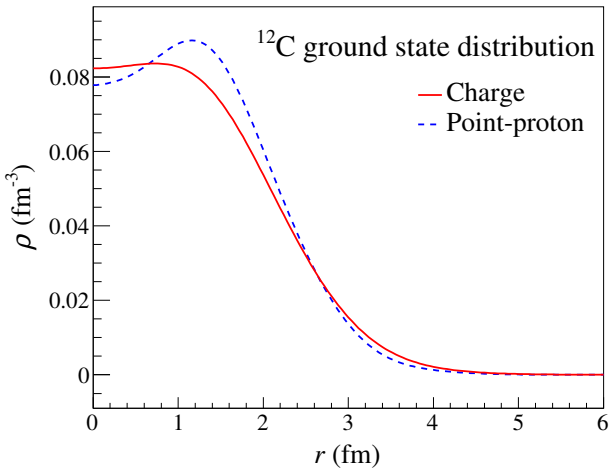

Figure C.1: Density distributions of the ^{12}C ground state. The charge distribution given by the SOG function is plotted by the red solid line, while the unfolded point-proton distribution is plotted by the blue dashed line.

Appendix D
Data tables of cross sections

Table D.1: Data table for α+^{10}C elastic scattering cross section.

$\theta_{\text{c.m.}}$ (deg)	$d\sigma/d\Omega$ (mb/sr)
4.25	$(1.35 \pm 0.22) \times 10^4$
4.75	$(9.01 \pm 1.44) \times 10^3$
5.94	$(4.06 \pm 0.66) \times 10^3$
6.31	$(2.90 \pm 0.47) \times 10^3$
6.69	$(2.07 \pm 0.33) \times 10^3$
7.06	$(1.36 \pm 0.22) \times 10^3$
9.50	$(3.04 \pm 0.49) \times 10^2$
11.0	$(3.50 \pm 0.56) \times 10^2$
13.0	$(2.48 \pm 0.40) \times 10^2$
15.0	$(1.10 \pm 0.18) \times 10^2$

Table D.2: Data table for α+^{10}C inelastic scattering cross section to the 2_1^+ state at $E_x = 3.35$ MeV.

$\theta_{\text{c.m.}}$ (deg)	$d\sigma/d\Omega$ (mb/sr)
5.94	$(1.50 \pm 0.29) \times 10^2$
6.31	$(1.30 \pm 0.25) \times 10^2$
6.69	$(1.03 \pm 0.20) \times 10^2$
7.06	$(1.30 \pm 0.25) \times 10^2$
9.50	$(6.65 \pm 1.14) \times 10^1$
11.0	$(3.27 \pm 0.56) \times 10^1$
13.0	$(1.76 \pm 0.31) \times 10^1$
15.0	$(2.33 \pm 0.40) \times 10^1$

References

[1] T. Kubo, M. Ishihara, N. Inabe, H. Kumagai, I. Tanihata, K. Yoshida, T. Nakamura, H. Okuno, S. Shimoura, and K. Asahi, Nucl. Instrum. Methods Phys. Res. B **70**, 309 (1992).

[2] Y. Yano, Nucl. Instrum. Methods Phys. Res. B **261**, 1009 (2007).

[3] M. Thoennessen, Nucl. Phys. A **834**, 688 (2010).

[4] P. Spiller and G. Franchetti, Nucl. Instrum. Methods Phys. Res. A **561**, 305 (2006).

[5] S. Gales, Nucl. Phys. A **834**, 717 (2010).

[6] H. Moeini, S. Ilieva, F. Aksouh, K. Boretzky, a. Chatillon, a. Corsi, P. Egelhof, H. Emling, G. Ickert, J. Jourdan, N. Kalantar Nayestanaki, D. Kiselev, O. Kiselev, C. Kozhuharov, T. Le Bleis, X. Le, Y. Litvinov, K. Mahata, J. Meier, F. Nolden, S. Paschalis, U. Popp, H. Simon, M. Steck, T. Stöhlker, H. Weick, D. Werthmüller, and a. Zalite, Nucl. Instrum. Methods Phys. Res. A **634**, 77 (2011).

[7] T. Kröll, M. Von Schmid, J. C. Zamora, S. Bagchi, S. Bönig, M. Csatlós, I. Dillmann, C. Dimopoulou, P. Egelhof, V. Eremin, T. Furuno, H. Geissel, R. Gernhäuser, M. N. Harakeh, A. L. Hartig, S. Ilieva, N. Kalantar-Nayestanaki, O. Kiselev, H. Kollmus, C. Kozhuharov, A. Krasznahorkay, M. Kuilman, S. Litvinov, Y. A. Litvinov, M. Mahjour-Shafiei, M. Mutterer, D. Nagae, M. A. Najafi, C. Nociforo, F. Nolden, U. Popp, C. Rigollet, S. Roy, C. Scheidenberger, M. Steck, B. Streicher, L. Stuhl, M. Thürauf, T. Uesaka, H. Weick, J. S. Winfield, D. Winters, P. J. Woods, T. Yamaguchi, K. Yue, and J. Zenihiro, Jour. Phys.: Conf. Ser. **724**, 012026 (2016).

[8] B. Franzke, Nucl. Instrum. Methods Phys. Res. B **24**, 18 (1987).

[9] H. Reich, W. Bourgeois, B. Franzke, a. Kritzer, and V. Varentsov, Nucl. Phys. A **626**, 417 (1997).

[10] B. Streicher, P. Egelhof, S. Ilieva, N. Kalantar-Nayestanaki, H. Kollmus, T. Kröll, M. Mutterer, M. von Schmid, and M. Träger, Nucl. Instrum. Methods Phys. Res. A **654**, 604 (2011).

[11] M. Steck, P. Beller, K. Beckert, B. Franzke, and F. Nolden, Nucl. Instrum. Methods Phys. Res. A **532**, 357 (2004).

[12] M. von Schmid, S. Bagchi, S. Bönig, M. Csatlós, I. Dillmann, C. Dimopoulou, P. Egelhof, V. Eremin, T. Furuno, H. Geissel, R. Gernhäuser, M. N. Harakeh, A.-L. Hartig, S. Ilieva, N. Kalantar-Nayestanaki, O. Kiselev, H. Kollmus, C. Kozhuharov, A. Krasznahorkay, T. Kröll, M. Kuilman, S. Litvinov, Y. A. Litvinov, M. Mahjour-Shafiei,

M. Mutterer, D. Nagae, M. A. Najafi, C. Nociforo, F. Nolden, U. Popp, C. Rigollet, S. Roy, C. Scheidenberger, M. Steck, B. Streicher, L. Stuhl, M. Thürauf, T. Uesaka, H. Weick, J. S. Winfield, D. Winters, P. J. Woods, T. Yamaguchi, K. Yue, J. C. Zamora, and J. Zenihiro, Physica Scripta **T166**, 014005 (2015).

[13] J. C. Zamora, T. Aumann, S. Bagchi, S. Bönig, M. Csatlós, I. Dillmann, C. Dimopoulou, P. Egelhof, V. Eremin, T. Furuno, H. Geissel, R. Gernhäuser, M. Harakeh, A.-L. Hartig, S. Ilieva, N. Kalantar-Nayestanaki, O. Kiselev, H. Kollmus, C. Kozhuharov, A. Krasznahorkay, T. Kröll, M. Kuilman, S. Litvinov, Y. Litvinov, M. Mahjour-Shafiei, M. Mutterer, D. Nagae, M. Najafi, C. Nociforo, F. Nolden, U. Popp, C. Rigollet, S. Roy, C. Scheidenberger, M. von Schmid, M. Steck, B. Streicher, L. Stuhl, M. Thürauf, T. Uesaka, H. Weick, J. Winfield, D. Winters, P. Woods, T. Yamaguchi, K. Yue, and J. Zenihiro, Phys. Lett. B **763**, 16 (2016).

[14] J. C. Zamora, T. Aumann, S. Bagchi, S. Bönig, M. Csatlós, I. Dillmann, C. Dimopoulou, P. Egelhof, V. Eremin, T. Furuno, H. Geissel, R. Gernhäuser, M. N. Harakeh, A. L. Hartig, S. Ilieva, N. Kalantar-Nayestanaki, O. Kiselev, H. Kollmus, C. Kozhuharov, A. Krasznahorkay, T. Kröll, M. Kuilman, S. Litvinov, Y. A. Litvinov, M. Mahjour-Shafiei, M. Mutterer, D. Nagae, M. A. Najafi, C. Nociforo, F. Nolden, U. Popp, C. Rigollet, S. Roy, C. Scheidenberger, M. Von Schmid, M. Steck, B. Streicher, L. Stuhl, M. Thürauf, T. Uesaka, H. Weick, J. S. Winfield, D. Winters, P. J. Woods, T. Yamaguchi, K. Yue, and J. Zenihiro, Phys. Rev. C **96**, 034617 (2017).

[15] J. Glorius, C. Langer, Z. Slavkovská, L. Bott, C. Brandau, B. Brückner, K. Blaum, X. Chen, S. Dababneh, T. Davinson, P. Erbacher, S. Fiebiger, T. Gaßner, K. Göbel, M. Groothuis, A. Gumberidze, G. Gyürky, M. Heil, R. Hess, R. Hensch, P. Hillmann, P.-M. Hillenbrand, O. Hinrichs, B. Jurado, T. Kausch, A. Khodaparast, T. Kisselbach, N. Klapper, C. Kozhuharov, D. Kurtulgil, G. Lane, C. Lederer-Woods, M. Lestinsky, S. Litvinov, Y. A. Litvinov, B. Löher, F. Nolden, N. Petridis, U. Popp, T. Rauscher, M. Reed, R. Reifarth, M. S. Sanjari, D. Savran, H. Simon, U. Spillmann, M. Steck, T. Stöhlker, J. Stumm, A. Surzhykov, T. Szücs, T. T. Nguyen, A. Taremi Zadeh, B. Thomas, S. Y. Torilov, H. Törnqvist, M. Träger, C. Trageser, S. Trotsenko, L. Varga, M. Volknandt, H. Weick, M. Weigand, C. Wolf, P. J. Woods, and Y. M. Xing, Phys. Rev. Lett. **122**, 092701 (2019).

[16] G. A. Korolev, A. A. Vorobyov, and Y. K. Zalite, Nucl. Instrum. Methods **97**, 323 (1971).

[17] S. Ilieva, F. Aksouh, G. D. Alkhazov, L. Chulkov, A. V. Dobrovolsky, P. Egelhof, H. Geissel, M. Gorska, A. Inglessi, R. Kanungo, A. V. Khanzadeev, O. A. Kiselev, G. A. Korolev, X. C. Le, Y. A. Litvinov, C. Nociforo, D. M. Seliverstov, L. O. Sergeev, H. Simon, V. A. Volkov, A. A. Vorobyov, H. Weick, V. I. Yatsoura, and A. A. Zhdanov, Nucl. Phys. A **875**, 8 (2012).

[18] S. Neumaier, G. Alkhazov, M. Andronenko, A. Dobrovolsky, P. Egelhof, G. Gavrilov, H. Geissel, H. Irnich, A. Khanzadeev, G. Korolev, A. Lobodenko, G. Münzenberg,

M. Mutterer, W. Schwab, D. Seliverstov, T. Suzuki, N. Timofeev, A. Vorobyov, and V. Yatsoura, Nucl. Phys. A **712**, 247 (2002).

[19] T. Hashimoto, H. Ishiyama, T. Ishikawa, T. Kawamura, K. Nakai, Y. Watanabe, H. Miyatake, M. Tanaka, Y. Fuchi, N. Yoshikawa, S. Jeong, I. Katayama, T. Nomura, T. Furukawa, S. Mitsuoka, K. Nishio, M. Matsuda, H. Ikezoe, T. Fukuda, S. Das, P. Saha, Y. Mizoi, T. Komatsubara, M. Yamaguchi, and Y. Tagishi, Nucl. Instrum. Methods Phys. Res. A **556**, 339 (2006).

[20] C. Demonchy, M. Caamaño, H. Wang, W. Mittig, P. Roussel-Chomaz, H. Savajols, M. Chartier, D. Cortina-Gil, A. Fomichev, G. Frémont, P. Gangnant, A. Gillibert, L. Giot, M. Golovkov, B. Jurado, J. Libin, A. Obertelli, E. Pollaco, A. Rodin, C. Spitaels, S. Stepantsov, G. Ter-Akopian, and R. Wolski, Nucl. Instrum. Methods Phys. Res. A **583**, 341 (2007).

[21] D. Suzuki, M. Ford, D. Bazin, W. Mittig, W. G. Lynch, T. Ahn, S. Aune, E. Galyaev, A. Fritsch, J. Gilbert, F. Montes, A. Shore, J. Kolata, J. Browne, A. Howard, A. Roberts, and X. Tang, Nucl. Instrum. Methods Phys. Res. A **691**, 39 (2012).

[22] S. Ota, H. Tokieda, C. S. Lee, and Y. N. Watanabe, Jour. Rad. Nucl. Chem. **305**, 907 (2015).

[23] J. Bradt, D. Bazin, F. Abu-Nimeh, T. Ahn, Y. Ayyad, S. B. Novo, L. Carpenter, M. Cortesi, M. Kuchera, W. Lynch, W. Mittig, S. Rost, N. Watwood, and J. Yurkon, Nucl. Instrum. Methods Phys. Res. A **875**, 65 (2017).

[24] T. Roger, J. Pancin, G. Grinyer, B. Mauss, A. Laffoley, P. Rosier, H. Alvarez-Pol, M. Babo, B. Blank, M. Caamaño, S. Ceruti, J. Daemen, S. Damoy, B. Duclos, B. Fernández-Domínguez, F. Flavigny, J. Giovinazzo, T. Goigoux, J. Henares, P. Konczykowski, T. Marchi, G. Lebertre, N. Lecesne, L. Legeard, C. Maugeais, G. Minier, B. Osmond, J. Pedroza, J. Pibernat, O. Poleshchuk, E. Pollacco, R. Raabe, B. Raine, F. Renzi, F. Saillant, P. Sénécal, P. Sizun, D. Suzuki, J. Swartz, C. Wouters, G. Wittwer, and J. Yang, Nucl. Instrum. Methods Phys. Res. A **895**, 126 (2018).

[25] B. Mauss, P. Morfouace, T. Roger, J. Pancin, G. Grinyer, J. Giovinazzo, V. Alcindor, H. Álvarez-Pol, A. Arokiaraj, M. Babo, B. Bastin, C. Borcea, M. Caamaño, S. Ceruti, B. Fernández-Domínguez, E. Foulon-Moret, P. Gangnant, S. Giraud, A. Laffoley, G. Mantovani, T. Marchi, B. Monteagudo, J. Pibernat, O. Poleshchuk, R. Raabe, J. Refsgaard, A. Revel, F. Saillant, M. Stanoiu, G. Wittwer, and J. Yang, Nucl. Instrum. Methods Phys. Res. A **940**, 498 (2019).

[26] E. Koshchiy, G. V. Rogachev, E. Pollacco, S. Ahn, E. Uberseder, J. Hooker, J. Bishop, E. Aboud, M. Barbui, V. Z. Goldberg, C. Hunt, H. Jayatissa, C. Magana, R. O'Dwyer, B. T. Roeder, A. Saastamoinen, and S. Upadhyayula, arXiv, 1906.07845 (2019).

[27] I. Tanihata, M. Alcorta, D. Bandyopadhyay, R. Bieri, L. Buchmann, B. Davids, N. Galinski, D. Howell, W. Mills, S. Mythili, R. Openshaw, E. Padilla-Rodal,

G. Ruprecht, G. Sheffer, A. C. Shotter, M. Trinczek, P. Walden, H. Savajpls, T. Roger, M. Caamaño, W. Mittig, P. Roussel-Chomaz, R. Kanungo, A. Gallant, M. Notani, G. Savard, and I. J. Thompson, Phys. Rev. Lett. **100**, 192502 (2008).

[28] M. Vandebrouck, J. Gibelin, E. Khan, N. L. Achouri, H. Baba, D. Beaumel, Y. Blumenfeld, M. Caamaño, L. Càceres, G. Colò, F. Delaunay, B. Fernandez-Dominguez, U. Garg, G. F. Grinyer, M. N. Harakeh, N. Kalantar-Nayestanaki, N. Keeley, W. Mittig, J. Pancin, R. Raabe, T. Roger, P. Roussel-Chomaz, H. Savajols, O. Sorlin, C. Stodel, D. Suzuki, and J. C. Thomas, Phys. Rev. Lett. **113**, 032504 (2014).

[29] M. Vandebrouck, J. Gibelin, E. Khan, N. L. Achouri, H. Baba, D. Beaumel, Y. Blumenfeld, M. Caamaño, L. Càceres, G. Colò, F. Delaunay, B. Fernandez-Dominguez, U. Garg, G. F. Grinyer, M. N. Harakeh, N. Kalantar-Nayestanaki, N. Keeley, W. Mittig, J. Pancin, R. Raabe, T. Roger, P. Roussel-Chomaz, H. Savajols, O. Sorlin, C. Stodel, D. Suzuki, and J. C. Thomas, Phys. Rev. C **92**, 024316 (2015).

[30] S. Bagchi, J. Gibelin, M. Harakeh, N. Kalantar-Nayestanaki, N. Achouri, H. Akimune, B. Bastin, K. Boretzky, H. Bouzomita, M. Caamaão, L. Càceres, S. Damoy, F. Delaunay, B. Fernàndez-Domínguez, M. Fujiwara, U. Garg, G. Grinyer, O. Kamalou, E. Khan, A. Krasznahorkay, G. Lhoutellier, J. Libin, S. Lukyanov, K. Mazurek, M. Najafi, J. Pancin, Y. Penionzhkevich, L. Perrot, R. Raabe, C. Rigollet, T. Roger, S. Sambi, H. Savajols, M. Senoville, C. Stodel, L. Suen, J. Thomas, M. Vandebrouck, and J. V. de Walle, Phys. Lett. B **751**, 371 (2015).

[31] C. Rodríguez-Tajes, F. Farget, L. Acosta, H. Alvarez-Pol, M. Babo, F. Boulay, M. Caamaño, S. Damoy, B. Fernàndez-Domínguez, D. Galaviz, G. Grinyer, J. Grinyer, M. Harakeh, P. Konczykowski, I. Martel, J. Pancin, G. Randisi, F. Renzi, T. Roger, A. Sánchez-Benítez, P. Teubig, and M. Vandebrouck, Nucl. Phys. A **958**, 246 (2017).

[32] D. Suzuki, A. Shore, W. Mittig, J. J. Kolata, D. Bazin, M. Ford, T. Ahn, F. D. Becchetti, S. Beceiro Novo, D. Ben Ali, B. Bucher, J. Browne, X. Fang, M. Febbraro, A. Fritsch, E. Galyaev, A. M. Howard, N. Keeley, W. G. Lynch, M. Ojaruega, A. L. Roberts, and X. D. Tang, Phys. Rev. C **87**, 054301 (2013).

[33] A. Fritsch, S. Beceiro-Novo, D. Suzuki, W. Mittig, J. J. Kolata, T. Ahn, D. Bazin, F. D. Becchetti, B. Bucher, Z. Chajecki, X. Fang, M. Febbraro, A. M. Howard, Y. Kanada-En'yo, W. G. Lynch, A. J. Mitchell, M. Ojaruega, A. M. Rogers, A. Shore, T. Suhara, X. D. Tang, R. Torres-Isea, and H. Wang, Phys. Rev. C **93**, 014321 (2016).

[34] J. Bradt, Y. Ayyad, D. Bazin, W. Mittig, T. Ahn, S. B. Novo, B. Brown, L. Carpenter, M. Cortesi, M. Kuchera, W. Lynch, S. Rost, N. Watwood, J. Yurkon, J. Barney, U. Datta, J. Estee, A. Gillibert, J. Manfredi, P. Morfouace, D. Pérez-Loureiro, E. Pollacco, J. Sammut, and S. Sweany, Phys. Lett. B **778**, 155 (2018).

[35] Y. Ayyad, B. Olaizola, W. Mittig, G. Potel, V. Zelevinsky, M. Horoi, S. Beceiro-Novo, M. Alcorta, C. Andreoiu, T. Ahn, M. Anholm, L. Atar, A. Babu, D. Bazin,

N. Bernier, S. S. Bhattacharjee, M. Bowry, R. Caballero-Folch, M. Cortesi, C. Dalitz, E. Dunling, A. B. Garnsworthy, M. Holl, B. Kootte, K. G. Leach, J. S. Randhawa, Y. Saito, C. Santamaria, P. Šiurytė, C. E. Svensson, R. Umashankar, N. Watwood, and D. Yates, Phys. Rev. Lett. **123**, 082501 (2019).

[36] J. Hooker, G. V. Rogachev, E. Koshchiy, S. Ahn, M. Barbui, V. Z. Goldberg, C. Hunt, H. Jayatissa, E. C. Pollacco, B. T. Roeder, A. Saastamoinen, and S. Upadhyayula, Phys. Rev. C **100**, 054618 (2019).

[37] J. Pancin, J. L. Pedroza, J. Pibernat, E. Pollacco, A. Rebii, T. Roger, and P. Sizun, Nucl. Instrum. Methods Phys. Res. A **840**, 15 (2016).

[38] S. Beceiro-Novo, T. Ahn, D. Bazin, and W. Mittig, Prog. Part. Nucl. Phys. **84**, 124 (2015).

[39] Y. Ayyad, D. Bazin, S. Beceiro-Novo, M. Cortesi, and W. Mittig, Eur. Phys. J. A **54**, 181 (2018).

[40] E. Koshchiy, G. Rogachev, E. Pollacco, S. Ahn, E. Uberseder, J. Hooker, J. Bishop, E. Aboud, M. Barbui, V. Goldberg, C. Hunt, H. Jayatissa, C. Magana, R. Dwyer, B. Roeder, A. Saastamoinen, and S. Upadhyayula, Nucl. Instrum. Methods Phys. Res. A **957**, 163398 (2020).

[41] T. Furuno, T. Kawabata, H. J. Ong, S. Adachi, Y. Ayyad, T. Baba, Y. Fujikawa, T. Hashimoto, K. Inaba, Y. Ishii, S. Kabuki, H. Kubo, Y. Matsuda, Y. Matsuoka, T. Mizumoto, T. Morimoto, M. Murata, T. Sawano, T. Suzuki, A. Takada, J. Tanaka, I. Tanihata, T. Tanimori, D. T. Tran, M. Tsumura, and H. D. Watanabe, Nucl. Instrum. Methods Phys. Res. A **908**, 215 (2018).

[42] A. Ochi, T. Nagayoshi, S. Koishi, T. Tanimori, T. Nagae, and M. Nakamura, Nucl. Instrum. Methods Phys. Res. A **471**, 264 (2001).

[43] H. D. Watanabe, Master thesis, Kyoto University (2013).

[44] T. Furuno, Master thesis, Kyoto University (2014).

[45] T. Furuno, T. Kawabata, S. Adachi, Y. Ayyad, T. Baba, T. Hashimoto, Y. Ishii, S. Kabuki, H. Kubo, Y. Matsuda, Y. Matsuoka, T. Mizumoto, M. Murata, H. J. Ong, T. Sawano, A. Takada, J. Tanaka, I. Tanihata, T. Tanimori, M. Tsumura, and H. D. Watanabe, Jour. Phys.: Conf. Ser. **569**, 012042 (2014).

[46] M. Murata, Master thesis, Kyoto University (2015).

[47] T. Furuno, T. Kawabata, M. Murata, S. Adachi, Y. Ayyad, H. Baba, T. Baba, M. Cavallaro, T. Hashimoto, Y. Ishii, R. Kobayakawa, Y. Matsuda, Y. Matsuoka, T. Morimoto, T. Nanamura, S. Beceilo-Novo, H. J. Ong, A. Sakaue, J. Tanaka, I. Tanihata, D. T. Trong, M. Tsumura, and H. D. Watanabe, Jour. Phys.: Conf. Ser. **863**, 012076 (2017).

[48] T. Morimoto, Master thesis, Kyoto University (2017).

[49] K. Inaba, Master thesis, Kyoto University (2018).

[50] M. G. Mayer, Phys. Rev. **75**, 1969 (1949).

[51] O. Haxel, J. H. D. Jensen, and H. E. Suess, Phys. Rev. **75**, 1766 (1949).

[52] A. Navin, D. W. Anthony, T. Aumann, T. Baumann, D. Bazin, Y. Blumenfeld, B. A. Brown, T. Glasmacher, P. G. Hansen, R. W. Ibbotson, P. A. Lofy, V. Maddalena, K. Miller, T. Nakamura, B. V. Pritychenko, B. M. Sherrill, E. Spears, M. Steiner, J. A. Tostevin, J. Yurkon, and A. Wagner, Phys. Rev. Lett. **85**, 266 (2000).

[53] H. Iwasaki, T. Motobayashi, H. Akiyoshi, Y. Ando, N. Fukuda, H. Fujiwara, Z. Fülöp, K. I. Hahn, Y. Higurashi, M. Hirai, I. Hisanaga, N. Iwasa, T. Kijima, T. Minemura, T. Nakamura, M. Notani, S. Ozawa, H. Sakurai, S. Shimoura, S. Takeuchi, T. Teranishi, Y. Yanagisawa, and M. Ishihara, Phys. Lett. B **481**, 7 (2000).

[54] H. Iwasaki, T. Motobayashi, H. Akiyoshi, Y. Ando, N. Fukuda, H. Fujiwara, Z. Fülöp, K. Hahn, Y. Higurashi, M. Hirai, I. Hisanaga, N. Iwasa, T. Kijima, A. Mengoni, T. Minemura, T. Nakamura, M. Notani, S. Ozawa, H. Sagawa, H. Sakurai, S. Shimoura, S. Takeuchi, T. Teranishi, Y. Yanagisawa, and M. Ishihara, Phys. Lett. B **491**, 8 (2000).

[55] S. Shimoura, A. Saito, T. Minemura, Y. Matsuyama, H. Baba, H. Akiyoshi, N. Aoi, T. Gomi, Y. Higurashi, K. Ieki, N. Imai, N. Iwasa, H. Iwasaki, S. Kanno, S. Kubono, M. Kunibu, S. Michimasa, T. Motobayashi, T. Nakamura, H. Sakurai, M. Serata, E. Takeshita, S. Takeuchi, T. Teranishi, K. Ue, K. Yamada, Y. Yanagisawa, M. Ishihara, and N. Itagaki, Phys. Lett. B **560**, 31 (2003).

[56] C. Thibault, R. Klapisch, C. Rigaud, A. M. Poskanzer, R. Prieels, L. Lessard, and W. Reisdorf, Phys. Rev. C **12**, 644 (1975).

[57] T. Motobayashi, Y. Ikeda, K. Ieki, M. Inoue, N. Iwasa, T. Kikuchi, M. Kurokawa, S. Moriya, S. Ogawa, H. Murakami, S. Shimoura, Y. Yanagisawa, T. Nakamura, Y. Watanabe, M. Ishihara, T. Teranishi, H. Okuno, and R. Casten, Phys. Lett. B **346**, 9 (1995).

[58] B. Bastin, S. Grévy, D. Sohler, O. Sorlin, Z. Dombrádi, N. L. Achouri, J. C. Angélique, F. Azaiez, D. Baiborodin, R. Borcea, C. Bourgeois, A. Buta, A. Bürger, R. Chapman, J. C. Dalouzy, Z. Dlouhy, A. Drouard, Z. Elekes, S. Franchoo, S. Iacob, B. Laurent, M. Lazar, X. Liang, E. Liénard, J. Mrazek, L. Nalpas, F. Negoita, N. A. Orr, Y. Penionzhkevich, Z. Podolyák, F. Pougheon, P. Roussel-Chomaz, M. G. Saint-Laurent, M. Stanoiu, I. Stefan, F. Nowacki, and A. Poves, Phys. Rev. Lett. **99**, 022503 (2007).

[59] S. Takeuchi, M. Matsushita, N. Aoi, P. Doornenbal, K. Li, T. Motobayashi, H. Scheit, D. Steppenbeck, H. Wang, H. Baba, D. Bazin, L. Càceres, H. Crawford, P. Fallon, R. Gernhäuser, J. Gibelin, S. Go, S. Grévy, C. Hinke, C. R. Hoffman, R. Hughes, E. Ideguchi, D. Jenkins, N. Kobayashi, Y. Kondo, R. Krücken, T. Le Bleis, J. Lee,

G. Lee, A. Matta, S. Michimasa, T. Nakamura, S. Ota, M. Petri, T. Sako, H. Sakurai, S. Shimoura, K. Steiger, K. Takahashi, M. Takechi, Y. Togano, R. Winkler, and K. Yoneda, Phys. Rev. Lett. **109**, 182501 (2012).

[60] A. Ozawa, T. Kobayashi, T. Suzuki, K. Yoshida, and I. Tanihata, Phys. Rev. Lett. **84**, 5493 (2000).

[61] J. Prisciandaro, P. Mantica, B. Brown, D. Anthony, M. Cooper, A. Garcia, D. Groh, A. Komives, W. Kumarasiri, P. Lofy, A. Oros-Peusquens, S. Tabor, and M. Wiedeking, Phys. Lett. B **510**, 17 (2001).

[62] R. Janssens, B. Fornal, P. Mantica, B. Brown, R. Broda, P. Bhattacharyya, M. Carpenter, M. Cinausero, P. Daly, A. Davies, T. Glasmacher, Z. Grabowski, D. Groh, M. Honma, F. Kondev, W. Królas, T. Lauritsen, S. Liddick, S. Lunardi, N. Marginean, T. Mizusaki, D. Morrissey, A. Morton, W. Mueller, T. Otsuka, T. Pawlat, D. Seweryniak, H. Schatz, A. Stolz, S. Tabor, C. Ur, G. Viesti, I. Wiedenhöver, and J. Wrzesiński, Phys. Lett. B **546**, 55 (2002).

[63] A. Gade, R. V. F. Janssens, D. Bazin, R. Broda, B. A. Brown, C. M. Campbell, M. P. Carpenter, J. M. Cook, A. N. Deacon, D.-C. Dinca, B. Fornal, S. J. Freeman, T. Glasmacher, P. G. Hansen, B. P. Kay, P. F. Mantica, W. F. Mueller, J. R. Terry, J. A. Tostevin, and S. Zhu, Phys. Rev. C **74**, 021302 (2006).

[64] F. Wienholtz, D. Beck, K. Blaum, C. Borgmann, M. Breitenfeldt, R. B. Cakirli, S. George, F. Herfurth, J. D. Holt, M. Kowalska, S. Kreim, D. Lunney, V. Manea, J. Menéndez, D. Neidherr, M. Rosenbusch, L. Schweikhard, A. Schwenk, J. Simonis, J. Stanja, R. N. Wolf, and K. Zuber, Nature **498**, 346 (2013).

[65] M. Rosenbusch, P. Ascher, D. Atanasov, C. Barbieri, D. Beck, K. Blaum, C. Borgmann, M. Breitenfeldt, R. B. Cakirli, A. Cipollone, S. George, F. Herfurth, M. Kowalska, S. Kreim, D. Lunney, V. Manea, P. Navrátil, D. Neidherr, L. Schweikhard, V. Somà, J. Stanja, F. Wienholtz, R. N. Wolf, and K. Zuber, Phys. Rev. Lett. **114**, 202501 (2015).

[66] D. Steppenbeck, S. Takeuchi, N. Aoi, P. Doornenbal, M. Matsushita, H. Wang, Y. Utsuno, H. Baba, S. Go, J. Lee, K. Matsui, S. Michimasa, T. Motobayashi, D. Nishimura, T. Otsuka, H. Sakurai, Y. Shiga, N. Shimizu, P.-A. Söderström, T. Sumikama, R. Taniuchi, J. J. Valiente-Dobón, and K. Yoneda, Phys. Rev. Lett. **114**, 252501 (2015).

[67] D. Steppenbeck, S. Takeuchi, N. Aoi, P. Doornenbal, M. Matsushita, H. Wang, H. Baba, N. Fukuda, S. Go, M. Honma, J. Lee, K. Matsui, S. Michimasa, T. Motobayashi, D. Nishimura, T. Otsuka, H. Sakurai, Y. Shiga, P. A. Söderström, T. Sumikama, H. Suzuki, R. Taniuchi, Y. Utsuno, J. J. Valiente-Dobón, and K. Yoneda, Nature **502**, 207 (2013).

[68] S. Michimasa, M. Kobayashi, Y. Kiyokawa, S. Ota, D. S. Ahn, H. Baba, G. P. A. Berg, M. Dozono, N. Fukuda, T. Furuno, E. Ideguchi, N. Inabe, T. Kawabata, S. Kawase,

K. Kisamori, K. Kobayashi, T. Kubo, Y. Kubota, C. S. Lee, M. Matsushita, H. Miya, A. Mizukami, H. Nagakura, D. Nishimura, H. Oikawa, H. Sakai, Y. Shimizu, A. Stolz, H. Suzuki, M. Takaki, H. Takeda, S. Takeuchi, H. Tokieda, T. Uesaka, K. Yako, Y. Yamaguchi, Y. Yanagisawa, R. Yokoyama, K. Yoshida, and S. Shimoura, Phys. Rev. Lett. **121**, 022506 (2018).

[69] S. Chen, J. Lee, P. Doornenbal, A. Obertelli, C. Barbieri, Y. Chazono, P. Navrátil, K. Ogata, T. Otsuka, F. Raimondi, V. Somà, Y. Utsuno, K. Yoshida, H. Baba, F. Browne, D. Calvet, F. Château, N. Chiga, A. Corsi, M. L. Cortés, A. Delbart, J.-M. Gheller, A. Giganon, A. Gillibert, C. Hilaire, T. Isobe, J. Kahlbow, T. Kobayashi, Y. Kubota, V. Lapoux, H. N. Liu, T. Motobayashi, I. Murray, H. Otsu, V. Panin, N. Paul, W. Rodriguez, H. Sakurai, M. Sasano, D. Steppenbeck, L. Stuhl, Y. L. Sun, Y. Togano, T. Uesaka, K. Wimmer, K. Yoneda, N. Achouri, O. Aktas, T. Aumann, L. X. Chung, F. Flavigny, S. Franchoo, I. Gašparić, R.-B. Gerst, J. Gibelin, K. I. Hahn, D. Kim, T. Koiwai, Y. Kondo, P. Koseoglou, C. Lehr, B. D. Linh, T. Lokotko, M. MacCormick, K. Moschner, T. Nakamura, S. Y. Park, D. Rossi, E. Sahin, D. Sohler, P.-A. Söderström, S. Takeuchi, H. Törnqvist, V. Vaquero, V. Wagner, S. Wang, V. Werner, X. Xu, H. Yamada, D. Yan, Z. Yang, M. Yasuda, and L. Zanetti, Phys. Rev. Lett. **123**, 142501 (2019).

[70] K. Ikeda, N. Takigawa, and H. Horiuchi, Prog. Theor. Phys. Suppl **E68**, 464 (1968).

[71] F. Hoyle, Astrophys. J. Suppl. Ser. **1**, 121 (1954).

[72] Y. Kanada-En'yo, H. Horiuchi, and A. Doté, Phys. Rev. C **60**, 064304 (1999).

[73] Y. Kanada-En'yo, M. Kimura, and A. Ono, Prog. Theor. Exp. Phys. **2012**, 01A202 (2012).

[74] T. Kawabata, H. Akimune, H. Fujita, Y. Fujita, M. Fujiwara, K. Hara, K. Hatanaka, M. Itoh, Y. Kanada-En'yo, S. Kishi, K. Nakanishi, H. Sakaguchi, Y. Shimbara, A. Tamii, S. Terashima, M. Uchida, T. Wakasa, Y. Yasuda, H. Yoshida, and M. Yosoi, Phys. Lett. B **646**, 6 (2007).

[75] T. Yamada, Y. Funaki, H. Horiuchi, K. Ikeda, and A. Tohsaki, Prog. Theor. Phys. **120**, 1139 (2008).

[76] T. Furuno, T. Kawabata, S. Adachi, Y. Ayyad, Y. Kanada-En'yo, Y. Fujikawa, K. Inaba, M. Murata, H. J. Ong, M. Sferrazza, Y. Takahashi, T. Takeda, I. Tanihata, D. T. Tran, and M. Tsumura, Phys. Rev. C **100**, 054322 (2019).

[77] D. T. Tran, H. J. Ong, G. Hagen, T. D. Morris, N. Aoi, T. Suzuki, Y. Kanada-En'yo, L. S. Geng, S. Terashima, I. Tanihata, T. T. Nguyen, Y. Ayyad, P. Y. Chan, M. Fukuda, H. Geissel, M. N. Harakeh, T. Hashimoto, T. H. Hoang, E. Ideguchi, A. Inoue, G. R. Jansen, R. Kanungo, T. Kawabata, L. H. Khiem, W. P. Lin, K. Matsuta, M. Mihara, S. Momota, D. Nagae, N. D. Nguyen, D. Nishimura, T. Otsuka, A. Ozawa, P. P. Ren, H. Sakaguchi, C. Scheidenberger, J. Tanaka, M. Takechi, R. Wada, and T. Yamamoto, Nature Communications **9**, 1594 (2018).

[78] H. R. Collard, L. R. B. Elton, and R. Hofstadter, *Nuclear radii 2* (Springer 1967).

[79] I. Angeli and M. Csatlós, Nucl. Phys. A **288**, 480 (1977).

[80] I. Angeli and K. P. Marinova, J. Phys. G **42**, 055108 (2015).

[81] A. Bohr and B. R. Mottelson, *NUCLEAR STRUCTURE VOL I* (W. A. BENJAMIN, INC. 1971).

[82] E. P. Wigner and E. Feenberg, Rep. Prog. Phys. **8**, 274 (1941).

[83] M. G. Mayer, The shell model, Novel Lectures pp. 20-37, (1963).

[84] A. Bernstein, V. Brown, and V. Madsen, Phys. Lett. B **103**, 255 (1981).

[85] A. M. Bernstein, V. R. Brown, and V. A. Madsen, Comments Nucl. Part. Phys. **11**, 203 (1983).

[86] M. A. Kennedy, P. D. Cottle, and K. W. Kemper, Phys. Rev. C **46**, 1811 (1992).

[87] L. A. Riley, J. K. Jewell, P. D. Cottle, T. Glasmacher, K. W. Kemper, N. Alamanos, Y. Blumenfeld, J. A. Carr, M. J. Chromik, R. W. Ibbotson, F. Maréchal, W. E. Ormand, F. Petrovich, H. Scheit, and T. Suomijärvi, Phys. Rev. Lett. **82**, 4196 (1999).

[88] J. K. Jewell, L. A. Riley, P. D. Cottle, K. W. Kemper, T. Glasmacher, R. W. Ibbotson, H. Scheit, M. Chromik, Y. Blumenfeld, S. E. Hirzebruch, F. Maréchal, and T. Suomijärvi, Phys. Lett. B **454**, 181 (1999).

[89] H. Iwasaki, T. Motobayashi, H. Akiyoshi, Y. Ando, N. Fukuda, H. Fujiwara, Z. Fülöp, K. I., Y. Higurashi, M. Hirai, I. Hisanaga, N. Iwasa, T. Kijima, T. Minemura, T. Nakamura, M. Notani, S. Ozawa, H. Sakurai, S. Shimoura, S. Takeuchi, T. Teranishi, Y. Yanagisawa, and M. Ishihara, Phys. Lett. B **481**, 7 (2000).

[90] E. Khan, T. Suomijärvi, Y. Blumenfeld, N. Van Giai, N. Alamanos, F. Auger, E. Bauge, D. Beaumel, J. P. Delaroche, P. Delbourgo-Salvador, A. Drouart, S. Fortier, N. Frascaria, A. Gillibert, M. Girod, C. Jouanne, K. W. Kemper, A. Lagoyannis, V. Lapoux, A. Lépine-Szily, I. Lhenry, J. Libert, F. Maréchal, J. M. Maison, A. Musumarra, S. Ottini-Hustache, P. Piattelli, S. Pita, E. C. Pollacco, P. Roussel-Chomaz, D. Santonocito, J. E. Sauvestre, J. A. Scarpaci, and T. Zerguerras, Nucl. Phys. A **694**, 103 (2001).

[91] P. D. Cottle, Z. Hu, B. V. Pritychenko, J. A. Church, M. Fauerbach, T. Glasmacher, R. W. Ibbotson, K. W. Kemper, L. A. Riley, H. Scheit, and M. Steiner, Phys. Rev. Lett. **88**, 172502 (2002).

[92] Z. Elekes, Z. Dombrádi, A. Krasznahorkay, H. Baba, M. Csatlós, L. Csige, N. Fukuda, Z. Fülöp, Z. Gácsi, J. Gulyás, N. Iwasa, H. Kinugawa, S. Kubono, M. Kurokawa, X. Liu, S. Michimasa, T. Minemura, T. Motobayashi, A. Ozawa, A. Saito, S. Shimoura, S. Takeuchi, I. Tanihata, P. Thirolf, Y. Yanagisawa, and K. Yoshida, Phys. Lett. B **586**, 34 (2004).

[93] N. Imai, H. J. Ong, N. Aoi, H. Sakurai, K. Demichi, H. Kawasaki, H. Baba, Z. Dombrádi, Z. Elekes, N. Fukuda, Z. Fülöp, A. Gelberg, T. Gomi, H. Hasegawa, K. Ishikawa, H. Iwasaki, E. Kaneko, S. Kanno, T. Kishida, Y. Kondo, T. Kubo, K. Kurita, S. Michimasa, T. Minemura, M. Miura, T. Motobayashi, T. Nakamura, M. Notani, T. K. Onishi, A. Saito, S. Shimoura, T. Sugimoto, M. K. Suzuki, E. Takeshita, S. Takeuchi, M. Tamaki, K. Yamada, K. Yoneda, H. Watanabe, and M. Ishihara, Phys. Rev. Lett. **92**, 062501 (2004).

[94] C. Jouanne, V. Lapoux, F. Auger, N. Alamanos, A. Drouart, A. Gillibert, G. Lobo, A. Musumarra, L. Nalpas, E. Pollacco, J.-L. Sida, M. Trotta, Y. Blumenfeld, E. Khan, T. Suomijärvi, T. Zerguerras, P. Roussel-Chomaz, H. Savajols, A. Lagoyannis, and A. Pakou, Phys. Rev. C **72**, 014308 (2005).

[95] L. A. Riley, M. A. Abdelqader, D. Bazin, M. J. Bojazi, B. A. Brown, C. M. Campbell, J. A. Church, P. D. Cottle, D. C. Dinca, J. Enders, A. Gade, T. Glasmacher, M. Honma, S. Horibe, Z. Hu, K. W. Kemper, W. F. Mueller, H. Olliver, T. Otsuka, B. C. Perry, B. T. Roeder, B. M. Sherrill, T. P. Spencer, and J. R. Terry, Phys. Rev. C **72**, 024311 (2005).

[96] K. Yamada, T. Motobayashi, N. Aoi, H. Baba, K. Demichi, Z. Elekes, J. Gibelin, T. Gomi, H. Hasegawa, N. Imai, H. Iwasaki, S. Kanno, T. Kubo, K. Kurita, Y. Matsuyama, S. Michimasa, T. Minemura, M. Notani, T. Onishi K., H.J. Ong, S. Ota, A. Ozawa, A. Saito, H. Sakurai, S. Shimoura, E. Takeshita, S. Takeuchi, M. Tamaki, Y. Togano, Y. Yanagisawa, K. Yoneda, and I. Tanihata, Eur. Phys. J. A **25**, 409 (2005).

[97] H. J. Ong, N. Imai, N. Aoi, H. Sakurai, Z. Dombrádi, A. Saito, Z. Elekes, H. Baba, K. Demichi, Z. S. Fülöp, J. Gibelin, T. Gomi, H. Hasegawa, M. Ishihara, H. Iwasaki, S. Kanno, S. Kawai, T. Kubo, K. Kurita, Y. U. Matsuyama, S. Michimasa, T. Minemura, T. Motobayashi, M. Notani, S. Ota, H. K. Sakai, S. Shimoura, E. Takeshita, S. Takeuchi, M. Tamaki, Y. Togano, K. Yamada, Y. Yanagisawa, and K. Yoneda, Phys. Rev. C **73**, 024610 (2006).

[98] E. Becheva, Y. Blumenfeld, E. Khan, D. Beaumel, J. M. Daugas, F. Delaunay, C.-E. Demonchy, A. Drouart, M. Fallot, A. Gillibert, L. Giot, M. Grasso, N. Keeley, K. W. Kemper, D. T. Khoa, V. Lapoux, V. Lima, A. Musumarra, L. Nalpas, E. C. Pollacco, O. Roig, P. Roussel-Chomaz, J. E. Sauvestre, J. A. Scarpaci, F. Skaza, and H. S. Than, Phys. Rev. Lett. **96**, 012501 (2006).

[99] C. M. Campbell, N. Aoi, D. Bazin, M. D. Bowen, B. A. Brown, J. M. Cook, D. C. Dinca, A. Gade, T. Glasmacher, M. Horoi, S. Kanno, T. Motobayashi, L. A. Riley, H. Sagawa, H. Sakurai, K. Starosta, H. Suzuki, S. Takeuchi, J. R. Terry, K. Yoneda, and H. Zwahlen, Phys. Lett. B **652**, 169 (2007).

[100] M. Wiedeking, P. Fallon, A. O. Macchiavelli, J. Gibelin, M. S. Basunia, R. M. Clark, M. Cromaz, M.-A. Deleplanque, S. Gros, H. B. Jeppesen, P. T. Lake, I.-Y. Lee, L. G. Moretto, J. Pavan, L. Phair, E. Rodriguez-Vietiez, L. A. Bernstein, D. L. Bleuel, J. T.

Burke, S. R. Lesher, B. F. Lyles, and N. D. Scielzo, Phys. Rev. Lett. **100**, 152501 (2008).

[101] H. J. Ong, N. Imai, D. Suzuki, H. Iwasaki, H. Sakurai, T. K. Onishi, M. K. Suzuki, S. Ota, S. Takeuchi, T. Nakao, Y. Togano, Y. Kondo, N. Aoi, H. Baba, S. Bishop, Y. Ichikawa, M. Ishihara, T. Kubo, K. Kurita, T. Motobayashi, T. Nakamura, T. Okumura, and Y. Yanagisawa, Phys. Rev. C **78**, 014308 (2008).

[102] N. Iwasa, T. Motobayashi, S. Bishop, Z. Elekes, J. Gibelin, M. Hosoi, K. Ieki, K. Ishikawa, H. Iwasaki, S. Kawai, S. Kubono, K. Kurita, M. Kurokawa, N. Matsui, T. Minemura, H. Morikawa, T. Nakamura, M. Niikura, M. Notani, S. Ota, A. Saito, H. Sakurai, S. Shimoura, K. Sugawara, T. Sugimoto, H. Suzuki, T. Suzuki, I. Tanihata, E. Takeshita, T. Teranishi, Y. Togano, K. Yamada, K. Yamaguchi, and Y. Yanagisawa, Phys. Rev. C **78**, 024306 (2008).

[103] Z. Elekes, Z. Dombrádi, T. Aiba, N. Aoi, H. Baba, D. Bemmerer, B. A. Brown, T. Furumoto, Z. Fülöp, N. Iwasa, Á. Kiss, T. Kobayashi, Y. Kondo, T. Motobayashi, T. Nakabayashi, T. Nannichi, Y. Sakuragi, H. Sakurai, D. Sohler, M. Takashina, S. Takeuchi, K. Tanaka, Y. Togano, K. Yamada, M. Yamaguchi, and K. Yoneda, Phys. Rev. C **79**, 011302 (2009).

[104] M. Petri, P. Fallon, A. O. Macchiavelli, S. Paschalis, K. Starosta, T. Baugher, D. Bazin, L. Cartegni, R. M. Clark, H. L. Crawford, M. Cromaz, A. Dewald, A. Gade, G. F. Grinyer, S. Gros, M. Hackstein, H. B. Jeppesen, I. Y. Lee, S. McDaniel, D. Miller, M. M. Rajabali, A. Ratkiewicz, W. Rother, P. Voss, K. A. Walsh, D. Weisshaar, M. Wiedeking, and B. A. Brown, Phys. Rev. Lett. **107**, 102501 (2011).

[105] M. Petri, S. Paschalis, R. M. Clark, P. Fallon, A. O. Macchiavelli, K. Starosta, T. Baugher, D. Bazin, L. Cartegni, H. L. Crawford, M. Cromaz, U. Datta Pramanik, G. de Angelis, A. Dewald, A. Gade, G. F. Grinyer, S. Gros, M. Hackstein, H. B. Jeppesen, I. Y. Lee, S. McDaniel, D. Miller, M. M. Rajabali, A. Ratkiewicz, W. Rother, P. Voss, K. A. Walsh, D. Weisshaar, M. Wiedeking, B. A. Brown, C. Forssén, P. Navrátil, and R. Roth, Phys. Rev. C **86**, 044329 (2012).

[106] P. Voss, T. Baugher, D. Bazin, R. M. Clark, H. L. Crawford, A. Dewald, P. Fallon, A. Gade, G. F. Grinyer, H. Iwasaki, A. O. Macchiavelli, S. McDaniel, D. Miller, M. Petri, A. Ratkiewicz, W. Rother, K. Starosta, K. A. Walsh, D. Weisshaar, C. Forssén, R. Roth, and P. Navrátil, Phys. Rev. C **86**, 011303 (2012).

[107] Y. Togano, Y. Yamada, N. Iwasa, K. Yamada, T. Motobayashi, N. Aoi, H. Baba, S. Bishop, X. Cai, P. Doornenbal, D. Fang, T. Furukawa, K. Ieki, T. Kawabata, S. Kanno, N. Kobayashi, Y. Kondo, T. Kuboki, N. Kume, K. Kurita, M. Kurokawa, Y. G. Ma, Y. Matsuo, H. Murakami, M. Matsushita, T. Nakamura, K. Okada, S. Ota, Y. Satou, S. Shimoura, R. Shioda, K. N. Tanaka, S. Takeuchi, W. Tian, H. Wang, J. Wang, and K. Yoneda, Phys. Rev. Lett. **108**, 222501 (2012).

[108] S. Michimasa, Y. Yanagisawa, K. Inafuku, N. Aoi, Z. Elekes, Z. Fülöp, Y. Ichikawa, N. Iwasa, K. Kurita, M. Kurokawa, T. Machida, T. Motobayashi, T. Nakamura, T. Nakabayashi, M. Notani, H. J. Ong, T. K. Onishi, H. Otsu, H. Sakurai, M. Shinohara, T. Sumikama, S. Takeuchi, K. Tanaka, Y. Togano, K. Yamada, M. Yamaguchi, and K. Yoneda, Phys. Rev. C **89**, 054307 (2014).

[109] L. A. Riley, M. L. Agiorgousis, T. R. Baugher, D. Bazin, M. Bowry, P. D. Cottle, F. G. DeVone, A. Gade, M. T. Glowacki, K. W. Kemper, E. Lunderberg, D. M. McPherson, S. Noji, F. Recchia, B. V. Sadler, M. Scott, D. Weisshaar, and R. G. T. Zegers, Phys. Rev. C **90**, 011305 (2014).

[110] A. Corsi, S. Boissinot, A. Obertelli, P. Doornenbal, M. Dupuis, F. Lechaftois, M. Matsushita, S. Péru, S. Takeuchi, H. Wang, N. Aoi, H. Baba, P. Bednarczyk, M. Ciemala, A. Gillibert, T. Isobe, A. Jungclaus, V. Lapoux, J. Lee, M. Martini, K. Matsui, T. Motobayashi, D. Nishimura, S. Ota, E. Pollacco, H. Sakurai, C. Santamaria, Y. Shiga, D. Sohler, D. Steppenbeck, and R. Taniuchi, Phys. Lett. B **743**, 451 (2015).

[111] M. L. Cortés, P. Doornenbal, M. Dupuis, S. M. Lenzi, F. Nowacki, A. Obertelli, S. Péru, N. Pietralla, V. Werner, K. Wimmer, G. Authelet, H. Baba, D. Calvet, F. Château, A. Corsi, A. Delbart, J.-M. Gheller, A. Gillibert, T. Isobe, V. Lapoux, C. Louchart, M. Matsushita, S. Momiyama, T. Motobayashi, M. Niikura, H. Otsu, C. Péron, A. Peyaud, E. C. Pollacco, J.-Y. Roussé, H. Sakurai, C. Santamaria, M. Sasano, Y. Shiga, S. Takeuchi, R. Taniuchi, T. Uesaka, H. Wang, K. Yoneda, F. Browne, L. X. Chung, Z. Dombradi, S. Franchoo, F. Giacoppo, A. Gottardo, K. Hadynska-Klek, Z. Korkulu, S. Koyama, Y. Kubota, J. Lee, M. Lettmann, R. Lozeva, K. Matsui, T. Miyazaki, S. Nishimura, L. Olivier, S. Ota, Z. Patel, E. Sahin, C. M. Shand, P.-A. Söderström, I. Stefan, D. Steppenbeck, T. Sumikama, D. Suzuki, Z. Vajta, J. Wu, and Z. Xu, Phys. Rev. C **97**, 044315 (2018).

[112] L. A. Riley, D. Bazin, J. Belarge, P. C. Bender, B. A. Brown, P. D. Cottle, B. Elman, A. Gade, S. D. Gregory, E. B. Haldeman, K. W. Kemper, B. R. Klybor, M. A. Liggett, S. Lipschutz, B. Longfellow, E. Lunderberg, T. Mijatovic, J. Pereira, L. M. Skiles, R. Titus, A. Volya, D. Weisshaar, J. C. Zamora, and R. G. T. Zegers, Phys. Rev. C **100**, 044312 (2019).

[113] D. Tilley, J. Kelley, J. Godwin, D. Millener, J. Purcell, C. Sheu, and H. Weller, Nucl. Phys. A **745**, 155 (2004).

[114] T. R. Fisher, S. S. Hanna, D. C. Healey, and P. Paul, Phys. Rev. **176**, 1130 (1968).

[115] Y. Blumenfeld, F. Auger, J. E. Sauvestre, F. Maréchal, S. Ottini, N. Alamanos, A. Barbier, D. Beaumel, B. Bonnereau, D. Charlet, J. F. Clavelin, P. Courtat, P. Delbourgo-Salvador, R. Douet, M. Engrand, T. Ethvignot, A. Gillibert, E. Khan, V. Lapoux, A. Lagoyannis, L. Lavergne, S. Lebon, P. Lelong, A. Lesage, V. Le Ven, I. Lhenry, J. M. Martin, A. Musumarra, S. Pita, L. Petizon, E. Pollacco, J. Pouthas, A. Richard, D. Rougier, D. Santonocito, J. A. Scarpaci, J. L. Sida, C. Soulet, J. S. Stutzmann,

T. Suomijärvi, M. Szmigiel, P. Volkov, and G. Voltolini, Nucl. Instrum. Methods Phys. Res. A **421**, 471 (1999).

[116] J.-P. Jeukenne, A. Lejeune, and C. Mahaux, Phys. Rev. C **16**, 80 (1977).

[117] E. A. McCutchan, C. J. Lister, S. C. Pieper, R. B. Wiringa, D. Seweryniak, J. P. Greene, P. F. Bertone, M. P. Carpenter, C. J. Chiara, G. Gürdal, C. R. Hoffman, R. V. F. Janssens, T. L. Khoo, T. Lauritsen, and S. Zhu, Phys. Rev. C **86**, 014312 (2012).

[118] R. Veenhof, Garfield - simulation of gaseous detectors, http://garfield.web.cern.ch/garfield/.

[119] S. Mukhopadhyay and N. Majumdar, Engineering Analysis with Boundary Elements **33**, 105 (2009).

[120] A. Ochi, T. Nagayoshi, S. Koishi, T. Tanimori, T. Nagae, and M. Nakamura, Nucl. Instrum. Methods Phys. Res. A **471**, 264 (2001).

[121] Y. Mizumura, T. Tanimori, H. Kubo, A. Takada, J. D. Parker, T. Mizumoto, S. Sonoda, D. Tomono, T. Sawano, K. Nakamura, Y. Matsuoka, S. Komura, S. Nakamura, M. Oda, K. Miuchi, S. Kabuki, Y. Kishimoto, S. Kurosawa, and S. Iwaki, Journal of Instrumentation **9**, C05045 (2014).

[122] D. Tomono, T. Mizumoto, A. Takada, S. Komura, Y. Matsuoka, Y. Mizumura, M. Oda, and T. Tanimori, Scientific Reports **7**, 41972 (2017).

[123] T. Tanimori, Y. Mizumura, A. Takada, S. Miyamoto, T. Takemura, T. Kishimoto, S. Komura, H. Kubo, S. Kurosawa, Y. Matsuoka, K. Miuchi, T. Mizumoto, Y. Nakamasu, K. Nakamura, J. D. Parker, T. Sawano, S. Sonoda, D. Tomono, and K. Yoshikawa, Scientific Reports **7**, 41511 (2017).

[124] S. Komura, A. Takada, Y. Mizumura, S. Miyamoto, T. Takemura, T. Kishimoto, H. Kubo, S. Kurosawa, Y. Matsuoka, K. Miuchi, T. Mizumoto, Y. Nakamatsu, K. Nakamura, M. Oda, J. D. Parker, T. Sawano, S. Sonoda, T. Tanimori, D. Tomono, and K. Yoshikawa, The Astrophysical Journal **839**, 41 (2017).

[125] K. Miuchi, H. Nishimura, K. Hattori, N. Higashi, C. Ida, S. Iwaki, S. Kabuki, H. Kubo, S. Kurosawa, K. Nakamura, J. Parker, T. Sawano, M. Takahashi, T. Tanimori, K. Taniue, K. Ueno, H. Sekiya, A. Takeda, K. Tsuchiya, and A. Takada, Phys. Lett. B **686**, 11 (2010).

[126] K. Nakamura, K. Miuchi, T. Tanimori, H. Kubo, A. Takada, J. Parker, T. Mizumoto, Y. Mizumura, H. Nishimura, H. Sekiya, A. Takeda, T. Sawano, Y. Matsuoka, S. Komura, Y. Yamaguchi, and T. Hashimoto, Progress of Theoretical and Experimental Physics **2015**, 043F01 (2015).

[127] J. Parker, K. Hattori, H. Fujioka, M. Harada, S. Iwaki, S. Kabuki, Y. Kishimoto, H. Kubo, S. Kurosawa, K. Miuchi, T. Nagae, H. Nishimura, T. Oku, T. Sawano, T. Shinohara, J. Suzuki, A. Takada, T. Tanimori, and K. Ueno, Nucl. Instrum. Methods Phys. Res. A **697**, 23 (2013).

[128] J. Parker, M. Harada, K. Hattori, S. Iwaki, S. Kabuki, Y. Kishimoto, H. Kubo, S. Kurosawa, Y. Matsuoka, K. Miuchi, T. Mizumoto, H. Nishimura, T. Oku, T. Sawano, T. Shinohara, J. Suzuki, A. Takada, T. Tanimori, and K. Ueno, Nucl. Instrum. Methods Phys. Res. A **726**, 155 (2013).

[129] C. Altunbas, M. Capéans, K. Dehmelt, J. Ehlers, J. Friedrich, I. Konorov, a. Gandi, S. Kappler, B. Ketzer, R. De Oliveira, S. Paul, a. Placci, L. Ropelewski, F. Sauli, F. Simon, and M. Van Stenis, Nucl. Instrum. Methods Phys. Res. A **490**, 177 (2002).

[130] F. Sauli, Nucl. Instrum. Methods Phys. Res. A **386**, 531 (1997).

[131] T. Mizumoto, Y. Matsuoka, Y. Mizumura, T. Tanimori, H. Kubo, A. Takada, S. Iwaki, T. Sawano, K. Nakamura, S. Komura, S. Nakamura, T. Kishimoto, M. Oda, S. Miyamoto, T. Takemura, J. Parker, D. Tomono, S. Sonoda, K. Miuchi, and S. Kurosawa, Nucl. Instrum. Methods Phys. Res. A **800**, 40 (2015).

[132] H. Baba, T. Ichihara, T. Ohnishi, S. Takeuchi, K. Yoshida, Y. Watanabe, S. Ota, and S. Shimoura, Nucl. Instrum. Methods Phys. Res. A **616**, 65 (2010).

[133] T. Shimoda, H. Miyatake, and S. Morinobu, Nucl. Instrum. Methods Phys. Res. B **70**, 320 (1992).

[134] S. Mitsuoka, T. Shimoda, H. Miyatake, Y. Mizoi, H. Kobayashi, M. Sasaki, T. Shirakura, N. Takahashi, T. Murakami, and S. Morinobu, Nucl. Instrum. Methods Phys. Res. A **372**, 489 (1996).

[135] H. J. Ong, AIP Conf. Proc. **1588**, 146 (2014).

[136] H. Nishibata, R. Leguillon, A. Odahara, T. Shimoda, C. M. Petrache, Y. Ito, J. Takatsu, K. Tajiri, N. Hamatani, R. Yokoyama, E. Ideguchi, H. Watanabe, Y. Wakabayashi, K. Yoshinaga, T. Suzuki, S. Nishimura, D. Beaumel, G. Lehaut, D. Guinet, P. Desesquelles, D. Curien, K. Higashiyama, and N. Yoshinaga, Phys. Rev. C **91**, 054305 (2015).

[137] Y. L. Sun, J. Lee, Y. L. Ye, A. Obertelli, Z. H. Li, N. Aoi, H. J. Ong, Y. Ayyad, C. A. Bertulani, J. Chen, A. Corsi, F. Cappuzzello, M. Cavallaro, T. Furono, Y. C. Ge, T. Hashimoto, E. Ideguchi, T. Kawabata, J. L. Lou, Q. T. Li, G. Lorusso, F. Lu, H. N. Liu, S. Nishimura, H. Suzuki, J. Tanaka, M. Tanaka, D. T. Tran, M. B. Tsang, J. Wu, Z. Y. Xu, and T. Yamamoto, Phys. Rev. C **93**, 044607 (2016).

[138] J. Chen, J. L. Lou, Y. L. Ye, J. Rangel, A. M. Moro, D. Y. Pang, Z. H. Li, Y. C. Ge, Q. T. Li, J. Li, W. Jiang, Y. L. Sun, H. L. Zang, Y. Zhang, N. Aoi, E. Ideguchi, H. J. Ong, J. Lee, J. Wu, H. N. Liu, C. Wen, Y. Ayyad, K. Hatanaka, T. D. Tran,

T. Yamamoto, M. Tanaka, T. Suzuki, and T. T. Nguyen, Phys. Rev. C **94**, 064620 (2016).

[139] J. Chen, J. L. Lou, Y. L. Ye, Z. H. Li, Y. C. Ge, Q. T. Li, J. Li, W. Jiang, Y. L. Sun, H. L. Zang, N. Aoi, E. Ideguchi, H. J. Ong, Y. Ayyad, K. Hatanaka, D. T. Tran, T. Yamamoto, M. Tanaka, T. Suzuki, N. T. Tho, J. Rangel, A. M. Moro, D. Y. Pang, J. Lee, J. Wu, H. N. Liu, and C. Wen, Phys. Rev. C **93**, 034623 (2016).

[140] D. T. Tran, H. J. Ong, T. T. Nguyen, I. Tanihata, N. Aoi, Y. Ayyad, P. Y. Chan, M. Fukuda, T. Hashimoto, T. H. Hoang, E. Ideguchi, A. Inoue, T. Kawabata, L. H. Khiem, W. P. Lin, K. Matsuta, M. Mihara, S. Momota, D. Nagae, N. D. Nguyen, D. Nishimura, A. Ozawa, P. P. Ren, H. Sakaguchi, J. Tanaka, M. Takechi, S. Terashima, R. Wada, and T. Yamamoto, Phys. Rev. C **94**, 064604 (2016).

[141] H. Kumagai, A. Ozawa, N. Fukuda, K. Summerer, and I. Tanihata, Nucl. Instrum. Methods Phys. Res. A **470**, 562 (2001).

[142] Y. Matsuda, J. Zenihiro, W. Chao, H. Sakaguchi, J. Tanaka, M. Tsumura, and N. Nakatsuka, RIKEN Accel. Prog. Rep. **48**, 211 (2015).

[143] S. Adachi, T. Kawabata, K. Minomo, T. Kadoya, N. Yokota, H. Akimune, T. Baba, H. Fujimura, M. Fujiwara, Y. Funaki, T. Furuno, T. Hashimoto, K. Hatanaka, K. Inaba, Y. Ishii, M. Itoh, C. Iwamoto, K. Kawase, Y. Maeda, H. Matsubara, Y. Matsuda, H. Matsuno, T. Morimoto, H. Morita, M. Murata, T. Nanamura, I. Ou, S. Sakaguchi, Y. Sasamoto, R. Sawada, Y. Shimizu, K. Suda, A. Tamii, Y. Tameshige, M. Tsumura, M. Uchida, T. Uesaka, H. P. Yoshida, and S. Yoshida, Phys. Rev. C **97**, 014601 (2018).

[144] J. Ziegler, M. Ziegler, and J. Biersack, Nucl. Instrum. Methods Phys. Res. B **268**, 1818 (2010).

[145] S. Biagi, Nucl. Instrum. Methods Phys. Res. A **421**, 234 (1999).

[146] https://garfieldpp.web.cern.ch/garfieldpp/.

[147] A. Takada, T. Tanimori, H. Kubo, J. D. Parker, T. Mizumoto, Y. Mizumura, S. Iwaki, T. Sawano, K. Nakamura, K. Taniue, N. Higashi, Y. Matsuoka, S. Komura, Y. Sato, S. Namamura, M. Oda, S. Sonoda, D. Tomono, K. Miuchi, S. Kabuki, Y. Kishimoto, and S. Kurosawa, Journal of Instrumentation **8**, C10023 (2013).

[148] M. Fujiwara, H. Akimune, I. Daito, H. Fujimura, Y. Fujita, K. Hatanaka, H. Ikegami, I. Katayama, K. Nagayama, N. Matsuoka, S. Morinobu, T. Noro, M. Yoshimura, H. Sakaguchi, Y. Sakemi, A. Tamii, and M. Yosoi, Nucl. Instrum. Methods Phys. Res. A **422**, 484 (1999).

[149] J. Raynal, Computer program: ECIS-95, NEA-0850/19.

[150] G. R. Satchler and D. T. Khoa, Phys. Rev. C **55**, 285 (1997).

[151] M. Uchida, H. Sakaguchi, M. Itoh, M. Yosoi, T. Kawabata, H. Takeda, Y. Yasuda, T. Murakami, T. Ishikawa, T. Taki, N. Tsukahara, S. Terashima, U. Garg, M. Hedden, B. Kharraja, M. Koss, B. K. Nayak, S. Zhu, M. Fujiwara, H. Fujimura, K. Hara, E. Obayashi, H. P. Yoshida, H. Akimune, M. N. Harakeh, and M. Volkerts, Phys. Lett. B **557**, 12 (2003).

[152] J. Bency, Y. Tokimoto, Y. W. Lui, H. L. Clark, X. Chen, and D. H. Youngblood, Phys. Rev. C **68**, 014305 (2003).

[153] J. A. Nelder and R. Mead, The Computer Journal **7**, 308 (1965).

[154] E. Jones, T. Oliphant, P. Peterson *et al.*, SciPy: Open source scientific tools for Python (2001–).

[155] P. R. Bevington and D. K. Robinson, *Data Reduction and Error Analysis for the Physical Sciences* (McGraw-Hill 2003).

[156] Y. Kanada-En'yo, Phys. Rev. C **91**, 014315 (2015).

[157] A. Ozawa, I. Tanihata, T. Kobayashi, Y. Sugahara, O. Yamakawa, K. Omata, K. Sugimoto, D. Olson, W. Christie, and H. Wieman, Nucl. Phys. A **608**, 63 (1996).

[158] M. Kamimura, Nucl. Phys. A **351**, 456 (1981).

[159] G. Satchler, Nucl. Phys. A **472**, 215 (1987).

[160] E. A. McCutchan, C. J. Lister, R. B. Wiringa, S. C. Pieper, D. Seweryniak, J. P. Greene, M. P. Carpenter, C. J. Chiara, R. V. F. Janssens, T. L. Khoo, T. Lauritsen, I. Stefanescu, and S. Zhu, Phys. Rev. Lett. **103**, 192501 (2009).

[161] Y. Ogawa, K. Arai, Y. Suzuki, and K. Varga, Nucl. Phys. A **673**, 122 (2000).

[162] D. Thompson, M. Lemere, and Y. Tang, Nucl. Phys. A **286**, 53 (1977).

[163] E. Caurier, P. Navrátil, W. E. Ormand, and J. P. Vary, Phys. Rev. C **66**, 024314 (2002).

[164] R. Machleidt, F. Sammarruca, and Y. Song, Phys. Rev. C **53**, R1483 (1996).

[165] H. Sagawa, X. R. Zhou, X. Z. Zhang, and T. Suzuki, Phys. Rev. C **70**, 054316 (2004).

[166] S. Cohen and D. Kurath, Nucl. Phys. **73**, 1 (1965).

[167] L. Liu, T. Otsuka, N. Shimizu, Y. Utsuno, and R. Roth, Phys. Rev. C **86**, 014302 (2012).

[168] R. Machleidt and D. R. Entem, Phys. Rep. **503**, 1 (2011).

[169] Y. Kanada-En'yo, Phys. Rev. C **84**, 024317 (2011).

[170] I. Angeli and K. P. Marinova, At. Data and Nucl. Data Tab. **99**, 69 (2013).

[171] J. Henderson, G. Hackman, P. Ruotsalainen, S. R. Stroberg, K. D. Launey, J. D. Holt, F. A. Ali, N. Bernier, M. A. Bentley, M. Bowry, R. Caballero-Folch, L. J. Evitts, R. Frederick, A. B. Garnsworthy, P. E. Garrett, B. Jigmeddorj, A. I. Kilic, J. Lassen, J. Measures, D. Muecher, B. Olaizola, E. O'Sullivan, O. Paetkau, J. Park, J. Smallcombe, C. E. Svensson, R. Wadsworth, and C. Y. Wu, Phys. Lett. B **782**, 468 (2018).

[172] Y. Kanada-En'yo, Phys. Rev. C **71**, 014310 (2005).

[173] Y. Kanada-En'yo and H. Horiuchi, Phys. Rev. C **55**, 2860 (1997).

[174] B. Pritychenko, M. Birch, B. Singh, and M. Horoi, At. Data and Nucl. Data Tab. **107**, 1 (2016).

[175] M. Ito, Private communication.

[176] M. Ito, EPJ Web Conf. **117**, 06014 (2016).

[177] M. Nakao, H. Umehara, S. Ebata, and M. Ito, Phys. Rev. C **98**, 054318 (2018).

[178] T. Baba and M. Kimura, Phys. Rev. C **99**, 021303 (2019).

[179] J. B. Ehrman, Phys. Rev. **81**, 412 (1951).

[180] R. G. Thomas, Phys. Rev. **88**, 1109 (1952).

[181] P. Hough, 2nd Int. Conf. High-Energy Acc. Inst. pp. 554–558 (1959).

[182] R. O. Duda and P. E. Hart, Commun. ACM **15**, 11 (1972).

[183] H. D. Vries, C. D. Jager, and C. D. Vries, At. Data and Nucl. Data Tab. **36**, 495 (1987).

[184] J. J. Kelly, Phys. Rev. C **70**, 068202 (2004).

[185] R. G. Sachs, Phys. Rev. **126**, 2256 (1962).

[186] S. Adachi, Ph.D. thesis, Kyoto University (2018).